Hardware Innovations and Biomedical Applications of Magnetic Particle Imaging

by

Elaine Yu

A dissertation submitted in partial satisfaction of the

requirements for the degree of

Joint Doctor of Philosophy with University of California, San Francisco

in

Bioengineering

in the

Graduate Division

of the

University of California, Berkeley

Committee in charge:

Professor Steven Conolly, Chair
Professor John Kurhanewicz
Professor John Clarke

Summer 2017

Hardware Innovations and Biomedical Applications of Magnetic Particle Imaging

Abstract

Hardware Innovations and Biomedical Applications of Magnetic Particle Imaging

by

Elaine Yu

Joint Doctor of Philosophy with University of California, San Francisco in Bioengineering

University of California, Berkeley

Professor Steven Conolly, Chair

Magnetic particle imaging (MPI) shows extraordinary promise for biomedical applications: it is highly sensitive, linearly quantitative anywhere in the body, has zero signal from biological tissue, and is safe for patients. One of the major challenges in MPI is spatial resolution, which is fundamentally governed by selection field gradient strength and nanoparticle properties. In Chapter 3 of this dissertation, I describe the design and construction of a high gradient field-free line (FFL) scanner for improved spatial resolution. This is the world's first iron return MPI scanner, and the highest resolution FFL imager in the world. Armed with MPI-tailored nanoparticles created by our collaborators at the University of Washington and Lodespin Labs, we were able to achieve 700 μm resolution *in vivo*. We also successfully demonstrated dynamic projection MPI as well as 3D projection reconstruction MPI with this scanner. In addition to hardware innovations, I have also demonstrated the use of MPI in two very important applications, namely cancer imaging and gastrointestinal (GI) bleed detection. In Chapter 2 of this dissertation, I demonstrated the first use of MPI for *in vivo* cancer imaging with systemic tracer administration. Due to the enhanced permeability and retention (EPR) effect, the tumor was highlighted with tumor-to-background ratio of up to 50. The nanoparticle dynamics in the tumor was also well appreciated, with initial wash-in on the tumor rim, peak uptake at 6 hours, and eventual clearance beyond 48 hours. In Chapter 4 of this dissertation, I demonstrated the first use of MPI along with long-circulating, PEG-stabilized SPIOs for rapid *in vivo* detection and quantification of GI bleed. MPI-tailored, long-circulating SPIOs were systemically administered into a disease model of GI bleed. The tracer biodistribution was then tracked over time using our custom-built high resolution FFL MPI scanner which was described in Chapter 3. Dynamic MPI projection images captured tracer accumulation in the lower GI tract with excellent contrast. The robust contrast, sensitivity, safety, ability to image anywhere in the body, along with our MPI-tailored long-circulating SPIOs, demonstrates the outstanding promise of MPI as a clinical diagnostic tool.

To Malav, Victoria and Mom

Contents

List of Figures

List of Tables

Acknowledgments

I would first like to thank my advisor, Prof. Steven Conolly. I am extremely fortunate to have an amazing mentor like Steve. Steve is absolutely brilliant in his own right, yet insanely goofy at the same time. Working with him over the years taught me to take my science seriously, but not to take myself too seriously. He has always been able to patiently guide me toward the physical intuition of each problem at hand, and taught me how to be critical. He has also trained me to become a much (MUCH!) better writer and presenter than I was 5 years ago. Steve is also the most caring advisor one could hope for. He always tried everything in his power to make sure everyone was happy, and was there for us not just professionally, but personally as well.

I would also like to thank Dr. Patrick Goodwill. Without his guidance, I would not have been able to accomplish and learn as much as I have during my PhD. He was everyone's walking encyclopedia for everything MPI and beyond. He has patiently coached me through numerous technical problems, and pushed me to be at my technical best. I am extremely grateful for his mentorship over the years that molded me into the engineer that I am today.

I was also fortunate enough to be surrounded by amazing labmates throughout my PhD. Special thanks to Xinyi Zhou for being my little sister in lab and such a good friend. Oh and thank you for all the tasty baked goods that you fed us over the years! Yum. Thanks to Dr. Paul Keselman for always being there for me, from helping me assembling a 2000 lb magnet, taking a machine shop class with me, helping me with my teaching duties, traveling and hiking, to weekly rock climbing sessions. I am extremely lucky to have you as a friend! I would also like to thank Dr. Bo Zheng for being an amazing mentor. He is so knowledgeable, and at the same time such a humble person and wonderful teacher. I am so lucky to have had you there to answer my countless questions. I was also lucky enough to be mentored by Prof. Emine Saritas, Dr. Kuan Lu, Dr. Justin Konkle, and Dr. Laura Rose Croft when I first joined the lab. Thank you for being so warm and supporting, and for making me feel so welcome in the lab. I would like to also thank our visiting scholars over the years who became wonderful friends: Nicole Hinterberger, Friso Heslinga, Yueting Shi, and Ran Berzon. I also had the privilege to mentor undergraduate students in the lab: Mindy Bishop, Beliz Gunel, and David Mai. I learned a lot about myself and how I can improve as a mentor. I hope you have learned as much from me as I have from you! I would also like to thank Zhi Wei Tay, who is honestly the most hardworking, humble, and smart person I have ever met. You are truly inspiring! I would also like to thank Dr. Prashant Chandrasekharan for being so patient with me, coaching me through all the biomedical applications studies. Your chemistry and biology expertise has made all the difference in our lab this past year. Our lab was also fortunate enough to have an absolutely amazing lab manager, Robert Frawley, who sheltered us from all the logistical challenges of research so that we could conduct research without worry. Lastly, I would like to thank Ryan Orendorff and Daniel Hensley. The three of us joined the lab at the same time, took imaging and optimization classes together, worked on projects together in the lab, traveled together and grew together as researchers.

You being there for me (and quite frankly carrying me through) every step of the way made my experience all the better.

I would also like to thank the funding sources that made all my research possible. I am extremely lucky to have received funding through the NSF Graduate Research Fellowships Program. Work at UC Berkeley was supported by NIH 5R01EB019458-03, NIH 5R24MH106053-03, UC Discovery Grant 29623, and W. M. Keck Foundation Grant 009323. Additionally, work at Lodespin Labs and University of Washington was supported by NIH 1R41EB013520-01 and NIH 2R42EB013520-02A1.

I am also blessed with a wonderful mother, Meiling. Without you, there is no way I would be the person that I am today. You worked so hard your whole life, and always did everything in your power to give us the best opportunities despite all the challenges and hardship of raising us as a single mother. Thank you for giving me my twin sister, the absolute best friend I can ever wish for. You have both been there for me my whole life, loved, supported, and guided me through everything, and for that I am eternally grateful!

I would also like to thank my stepfather Cheewai who is truly nurturing, and helped us through our whole journey here in the US for the past 10 years. As a medical physicist, he has also inspired me to work on biomedical problems. I would also like to thank my stepsister Nikki and her husband Wei, who took me under their wing and became my first ever research mentors. Special thanks to my stepsisters Lillian and Linda and my sister's boyfriend Mark for all your love and support. I am so blessed to be able to call you my family!

Lastly, I would like to thank my husband Malav. We met in college at Rutgers University where we studied biomedical engineering together. We were then lucky enough to both join the bioengineering program here at Berkeley. Thank you so much for being there for me the entire way, supporting me through times of trouble in research and also celebrating every single tiny success with me. Thank you for believing in me when I didn't believe in myself, and for giving me the confidence I needed to succeed. Having you by my side was truly the best thing that I could've asked for!

Chapter 1

Introduction to Magnetic Particle Imaging

1.1 MPI: a safe tracer imaging modality for clinical translation

Magnetic Particle Imaging (MPI) is a novel tracer imaging modality that directly images superparamagnetic iron oxide (SPIO) nanoparticles. MPI detects zero signal from biological tissue, resulting in high contrast images akin to optical imaging and nuclear medicine techniques such as Positron Emission Tomography (PET) and Single-photon emission computed tomography (SPECT). Optical imaging suffers from signal depth attenuation and lacks quantitation, rendering it impractical for clinical applications. Nuclear imaging is widely used in the clinic due to its excellent contrast, but it suffers from short-lived tracers, radiation dose, low resolution, and high cost [1]. MPI signal, on the other hand, is not attenuated by tissue. Therefore, SPIOs anywhere in the body can be quantitatively imaged with high contrast and sensitivity. MPI is also safe, as it requires no ionizing radiation and is safe for patients with Chronic Kidney Disease (CKD).

A comparison of MPI with MRI and fluorescence imaging in Figure 1.1 demonstrates the value of MPI as a tracer modality. MPI detects no signal from native biological tissue, resulting in high image contrast. MPI also does not suffer from signal depth attenuation, and can quantitatively image anywhere in the body, as seen in Figure 1.1(b). This is in stark contrast from optical imaging which suffers from significant signal attenuation, as seen in Figure 1.1(a). SPIOs were initially used as a contrast agent in MRI, whereby T2* effects of the particles result in a signal dropout. This negative contrast is often problematic, as it relies on positive native signal for visualization. In addition, air-tissue interfaces result in signal drop-outs. As shown in Figure 1.1(c)&(d), the SPIO signal is nearly indistinguishable from the air signal.

MPI was first experimentally demonstrated in 2005 by Philips Research in Germany by Gleich and Weizenecker [3]. Since then, many groups around the world have been working

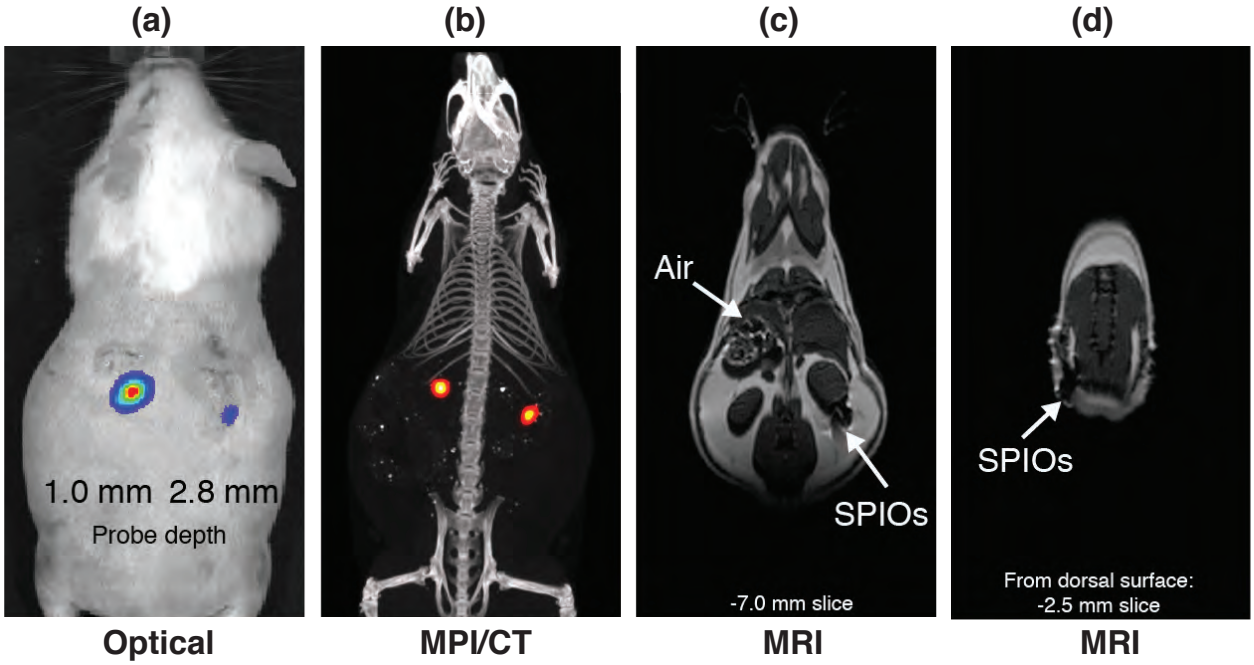

Figure 1.1: **Comparison of *in vivo* MPI/CT, Fluorescence Imaging, and MRI.** Image courtesy Dr. Bo Zheng [2]. Two point sources filled with a mixture of SPIOs (Nanomag-MIP) and fluorescent tracer (Angiosense 680 EX) were implanted below the dorsal skin surface of a mouse at two different depths. (a) Fluorescence imaging overlaid with gray scale photograph. The fluorescence signal decreases with implant depth due to scattering. Scan time: 5 seconds. (b) A maximum intensity projection of a 3D MPI volume coregistered with CT for anatomical reference. MPI: 50 mm $\times$ 37.5 mm $\times$ 100 mm field of view (FOV), 6.8 min scan. CT: 15 min scan, 184 μm isotropic resolution. MPI exhibits high image contrast with zero signal attenuation with depth. (c) In MRI, SPIO tracer in tissue results in a signal drop out similar to those generated at air-tissue interfaces. MRI: 40 mm $\times$ 80 mm FOV, 313 μm in-plane resolution, 17 min scan. (d) Coronal MRI slice 2.5 mm from dorsal surface of the animal. The SPIO is barely distinguishable from air pockets.

on various aspects of MPI such as imaging theory [4, 5, 6, 7, 8, 9], particle physics [10, 11], nanoparticle development [12, 13, 14, 15], imaging hardware [16, 17, 18, 19, 20, 21, 22], and safety limits [23]. There have been various demonstrations of biomedical applications with MPI: cell tracking [2, 24, 25], cancer imaging [26, 27], pulmonary imaging [28, 29], vascular and perfusion imaging [30, 31, 32], traumatic brain injury imaging [33], and magnetic hyperthermia [34, 35].

Prof. Steven Conolly and Dr. Patrick Goodwill started the development of Magnetic Particle Imaging in 2006 here at UC Berkeley. The Berkeley group has since then designed and constructed 8 generations (Figure 1.2) of scanners to improve sensitivity and spatial resolution. The design and construction of "Helga", a high resolution iron-core field-free line

scanner, will be described in Chapter 3 of this thesis. The Berkeley group currently has the world's highest resolution MPI scanners. In addition to hardware, the Berkeley group also developed the fast and robust x-space MPI image reconstruction algorithm [4, 5, 6, 7, 36, 37].

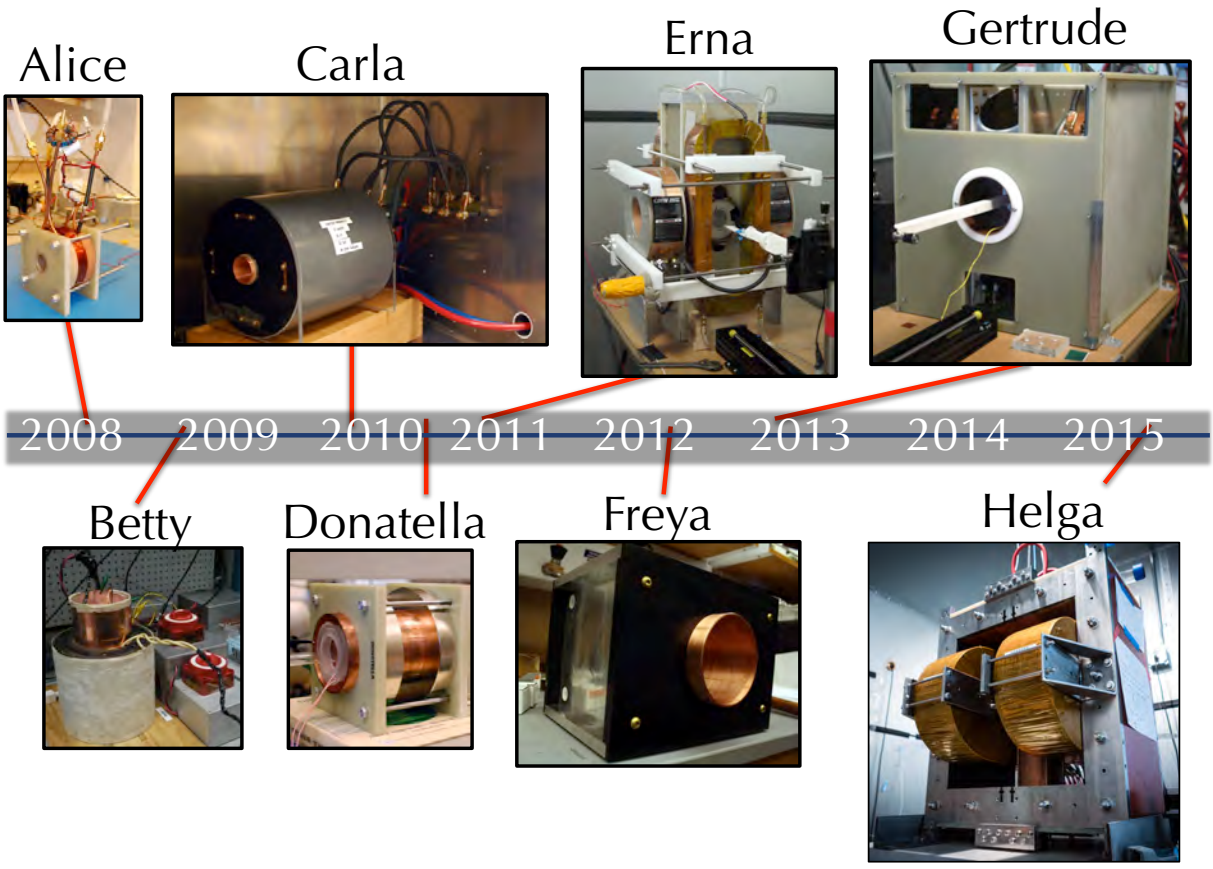

Figure 1.2: **Timeline of Berkeley Scanners.** Eight scanners were developed by the Conolly group at UC Berkeley since 2006.

MPI uses zero ionizing radiation for imaging, and the SPIO tracers are safe for clinical use. In fact, Ferumoxytol, a drug that is composed of SPIO coated with a carbohydrate shell, is approved for intravenous use by the FDA in the treatment of iron deficiency anemia [38]. Numerous other SPIO imaging agents are also approved for clinical use [39]. In addition, SPIOs have minimal effects on cell viability, proliferation, and differentiation [40]. Gadolinium and iodine based contrast agents commonly used for vascular imaging in MRI and CT are unsafe for patients with Chronic Kidney Disease (CKD). SPIO tracer, on the other hand, is cleared through the liver, so poses no threat to patients with CKD.

MPI is highly sensitive, detecting 5 nanograms of iron per voxel (or 200 labeled cells) [24]. MPI is also linearly quantitative, as shown in Figure 1.3. Stem cells labeled with

Resovist SPIOs were placed in a plastic imaging phantom at different concentrations in 6 wells. An MPI image was acquired, and the signal in each well was analyzed. There was a linear relationship between the cell number and MPI signal with an r^2 value of 0.994. The superb contrast, sensitivity, safety, and ability to image anywhere in the body gives MPI great promise for various applications. In this thesis, I will describe two proof-of-concept *in vivo* studies and hardware development.

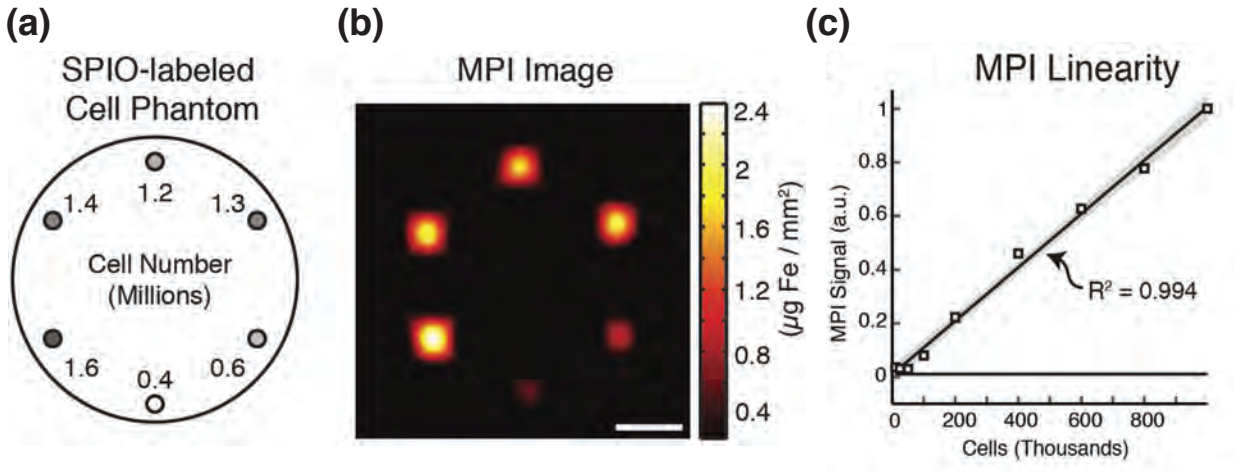

Figure 1.3: **MPI is Linearly Quantitative.** (a) Illustration of phantom with Resovist SPIO labeled cells samples of 6 different concentrations and (b) corresponding FFP MPI image. (c) MPI signal and cell number have a linear relationship ($r^2 = 0.994$). This shows that MPI is a linearly quantitative imaging modality. Image Courtesy of Dr. Bo Zheng [24]

In Chapter 2, I will describe the first *in vivo* demonstration of quantitative cancer detection with MPI. This work was done with the field-free point (FFP) 3D imager in our lab. The FFP imager creates a 3D image by rastering the FFP across the imaging volume. Nanoparticles of sizes between 10–100 nm in diameter are known to preferentially accumulate in tumors through enhanced permeability and retention (EPR) effect [41, 42, 43]. The hydrodynamic size of SPIOs used for MPI are within this range. Hence, we explored quantitative cancer imaging with MPI using long circulating SPIOs. The tumor was highlighted with tumor-to-background ratio of up to 50 due to EPR effect. The nanoparticle dynamics in the tumor was also well appreciated, with initial wash-in on the tumor rim, peak uptake at 6 hours, and eventual clearance beyond 48 hours. Lastly, we demonstrate the quantitative nature of MPI through compartmental fitting *in vivo*.

In Chapter 3, I will describe the design, construction, and characterization of the world's highest resolution field-free line (FFL) imager. This is the first scanner in our lab to use an iron-core electromagnet, instead of permanent magnets, to create the selection field gradient. The FFL imaging format can produce 2D projection images [17] as well as 3D images using projection reconstruction (magnetic computed tomography) [37]. We have shown with our

previous FFL system that the FFL imaging format has the potential for higher SNR and higher speed [6]. The resolution of MPI is fundamentally governed by gradient strength and nanoparticle properties. The Full Width of Half Maximum (FWHM) resolution improves linearly with magnetic field gradient strength [16]. Our previous FFL system had a gradient of 2.35 T/m. In this project, we designed and constructed a 6.3 T/m FFL imager.

In Chapter 4, I will describe the first demonstration of *in vivo* gastrointestinal (GI) bleed detection with MPI. This work was done using the new high resolution FFL imager described in Chapter 3. The FFL scanner enabled high resolution projection imaging, which allows for faster scanning speeds than the FFP imaging format. The ability to quantitatively image anywhere in the body makes MPI a promising technique for perfusion and blood pool imaging [28, 31]. When the SPIO tracer is used as a blood pool agent, tissue perfusion and tracer extravasation are clearly visualized. We used a long circulating SPIO tracer to quantitatively detect GI bleeding in mice. Armed with high speed projection capabilities, we were able to quantitatively track the gut bleed over time and determine the bleed rate. The robust contrast, sensitivity, safety, ability to image anywhere in the body, along with our MPI-tailored long-circulating SPIOs, render MPI a promising clinical diagnostic tool for GI bleeding.

1.2 MPI Imaging Theory and System Architecture

In this section, I will describe the signal generation and localization of MPI. In addition, a description of scanner architectures and image reconstruction algorithms will be provided.

1.2.1 Superparamagnetic Iron Oxide Nanoparticles for MPI

Most SPIO tracers for MPI consist of magnetite (Fe_3O_4) cores ranging from 5–30 nm. There are three general categories of iron-oxide cores: (1) monodispersed single cores [13, 15], (2) polydispersed (Resovist, Bayer Schering Pharma AG, Berlin, Germany), and (3) multicore clusters (Nanomag-MIP, micromod Partikeltechnologie GmbH, Rostock, Germany). Resovist, a discontinued MRI contrast agent, was the first tracer used for MPI [3], and most tracers are benchmarked against it. Tailoring SPIO core size and size distribution ensures optimum MPI performance. In fact, it was shown that SPIO tracer with ∼25 nm monodispersed cores results in nearly three-fold gain in sensitivity and ∼30% improvement in spatial resolution compared with Resovist [13].

The second important component of SPIO tracers is the surface coating that render the SPIO cores soluble in biologically relevant media. Various polysaccharides and polymers such as dextran, carboxydextran, starch, PMAO, chitosan, PEG, and combinations of these are used to coat iron oxide cores [12, 44]. The hydrodynamic size, surface charge, and coating density can be carefully optimized for each application (long circulation, cellular uptake, etc) [45]. The *in vivo* work described in this thesis were done using MPI-tailored long circulating particles from the Prof. Krishnan's Lab and Lodespin Labs. Theses tracers have 25 nm

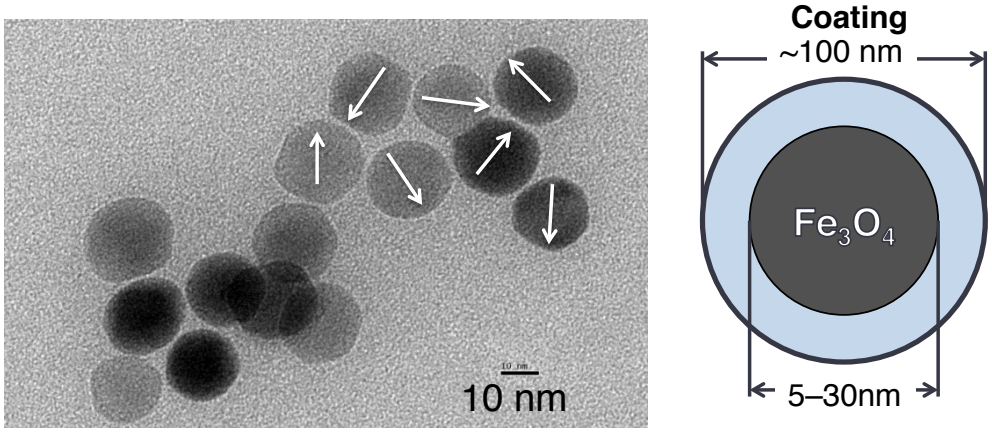

Figure 1.4: **Superparamagnetic Iron Oxide Nanoparticles for MPI.** *Left*: Transmission Electron Microscopy (TEM) image of monodispersed SPIO cores optimized for MPI. Image courtesy of Dr. Laura Rose Croft. *Right*: Diagram of SPIO tracers used for MPI.

monodisperse cores with high SNR and resolution, and are coated with PMAO-PEG for 105 min blood circulation half-life in mice, a breakthrough compared to Resovist with a half-life of less than 5 minutes of the injection [46, 47].

1.2.2 MPI Signal Generation

In standard MPI imaging, SPIOs are assumed to adiabatically align to an externally applied field. This means that there are no relaxation or hysteresis effects. The SPIOs are also saturated with an applied magnetic field $\geq$5 mT. A nonlinear Langevin equation is used to analytically describe the response of SPIOs to an externally applied field [3]. As shown in Figure 1.5, with a negative applied field, the particles are saturated negative and the corresponding bulk magnetization response is highlighted. Similarly, when there is zero applied field, there is zero magnetization from the particles. When the applied field is positive and $\geq$5 mT, the particles are saturated positive. When experiencing an alternating applied field, or drive field, the particles experience a 180° flip and traverse the Langevin curve.

When an inductive coil is placed near the SPIOs, their nonlinear magnetization response to alternating applied field is detected as a voltage signal according to the Faraday's law of induction. The signal detected is therefore the derivative of the Langevin response, which is our imaging point spread function (PSF). This can also be known as our imaging blurring function, as the resolution is determined by the width of the PSF. In our imaging systems, we apply a sinusoidal drive field with amplitudes from -20 mT to +20 mT at $\sim$20 kHz to excited the SPIOs using a transmit coil, and a receive coil is placed inside the transmit coil to detect the particle signal.

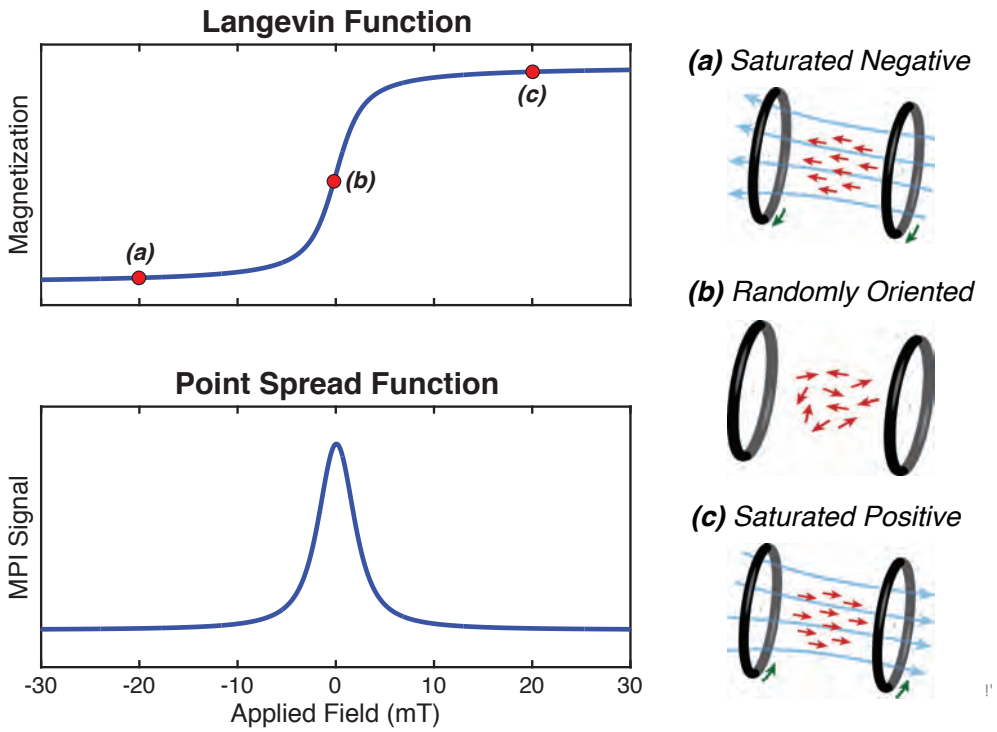

Figure 1.5: **Magnetic Property of SPIO used in MPI.** The magnetic response of SPIOs to an external applied field is analytically described by a Langevin function. When the applied field is negative (point a), the particles are saturated negative. When there is zero applied field, the particles are randomly oriented, resulting in zero bulk magnetization (point b). When the applied field is positive, the particles are saturated positive (point c). A time-varying applied field results in signal that can be detected in an inductive receive coil. The resulting signal is the derivative of the Langevin function.

1.2.3 MPI Signal Localization

In order to localized the particle signal in an imaging volume, a field-free region (FFR) is created with a selection field gradient. Note that the definition of the FFR is a region in which the applied field is less than H_{sat} [A/m], the field sufficient for saturation of the nanoparticle. Only the particles within the FFR are free to respond to the sinusoidal excitation drive field, while all the particles outside the FFR are saturated. This allows the particle signal to be localized. By shifting this FFR throughout the imaging volume in a specified trajectory and assigning the signal back to the instantaneous location of the FFR, an image can be made. An illustration of the selection field is shown in Figure 1.6(a). Two magnets facing each other are used to create a field gradient, thereby forming a FFR. Separate sets of Helmholtz coils are used to generate homogeneous field throughout the imaging field of view (FOV). By modulating the current strength in the coils, the FFR can be shifted throughout the FOV.

We call this component in our system the slow shift coils. Most of the MPI imaging systems so far have used permanent magnets (NdFeB) to create the selection field gradient and separate sets of Helmholtz coils to shift the FFR. In Chapter 3 of this thesis, I will describe a novel system which uses a pair of coils along with an iron return. This electromagnet takes care of both the selection field gradient and the slow shift components of the MPI system simultaneously.

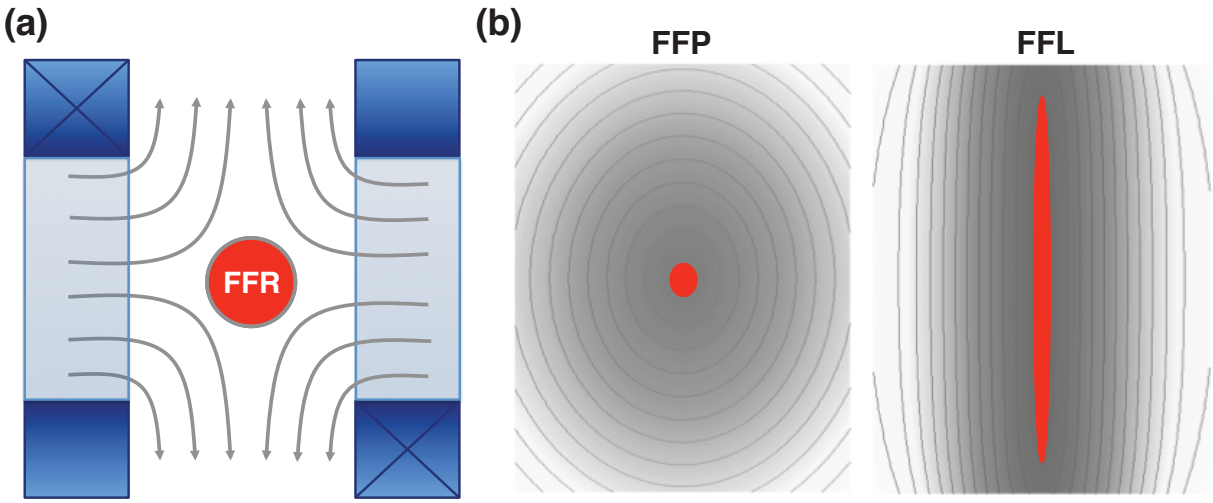

Figure 1.6: **Selection Field for Signal Localization.** (a) Two magnets facing each other are used to create a selection field. The FFR is defined as the region in which the applied field is $\leq H_{sat}$. (b) Field contour of the two different MPI selection field formats: field-free point (FFP) and field-free line (FFL).

There are two types of selection field formats for MPI: field-free point (FFP) and field-free line (FFL). Example field contours of both formats are shown in Figure 1.6(b). The FFP is shifted in all 3 dimensions to create a 3D MPI image. The FFL, on the other hand, can be shifted in the two dimensions perpendicular to the axis of the FFL to create a 2D projection image. The FFL format is also capable of making 3D images by taking projections at various angles and reconstructing the image through projection reconstruction. In many clinical situations, projection images provide sufficient information for diagnosis. A good example of this is coronary angiography, where iodinated contrast is injected through a catheter into the coronary artery, and real time projection X-ray images are acquired. The FFL format is therefore advantageous, as it enables high speed projection imaging and is still capable of 3D imaging when needed. The 3D images acquired using FFL and projection reconstruction have also been proven to have higher SNR than their FFP counterparts [37]. I will describe the projection reconstruction technique and SNR boost in further detail in the introduction of Chapter 3.

1.2.4 Image Reconstruction Algorithms

There are two main techniques for MPI scanning and reconstruction: (1) harmonic space system matrix MPI and (2) x-space MPI. The harmonic space method uses a system matrix that is comprised of the Fourier components of the temporal signal for every possible location of a point source [3, 9]. Reconstruction is achieved by regularization and inversion of the system matrix. Since the system matrix contains millions of elements, this inversion can be complex. Although resolution improvements are possible through this deconvolution-based technique, it also results in significant noise gain [48]. The second technique, x-space reconstruction, is used in this work. This technique allows real time reconstruction speeds, since there is no matrix inversion involved. In addition, it makes no attempt to deconvolve the MPI signal to improve resolution beyond what is determined by the physics of the particle and field gradient.

The drive field is sinusoidal, while the nonlinear particle response generates harmonics, allowing the particle signal to be distinguished from the signal from the drive field. However, since the particles are excited with a time-varying drive field, and the signal is detected with a inductive receive coil, the drive field is detected along with the particle signal. This direct feedthrough interference can be minimized by designing the receive coil as a tunable symmetric second-order hardware gradiometer [49]. This reduces the total magnetic coupling of the receive coil to the drive field. However, even with the gradiometer, the remaining signal from the drive field can still obscure the desired SPIO magnetization signal and limit SNR. To further reduce the direct feedthrough interference, a two stage passive notch filter is used. Dr. Bo Zheng from our lab has designed optimally noise-matched preamplifiers to amplify the filtered signal. Three additional stages of commercial preamplifiers and amplifiers are then used prior to digitization. Due to the nonlinear magnetiztaion of SPIOs, the MPI signal for a 20 kHz sinusoidal drive field can range from 40 kHz–1 MHz depending on the SPIO tracer. Therefore, the amplifiers are designed to be broadband. Both system matrix and x-space MPI suffer from direct feedthrough interference.

Due to magnetostimulation limits inherent to the operational frequency range of MPI [23], both system matrix and x-space methods scan the field of view in patches and then stitch them together afterwards. In x-space MPI, we refer to these patches as partial fields of view (pFOV). After the filtered and amplified received signal is velocity compensated, it is gridded into pFOVs based on the instantaneous position of the FFR. Since the drive field signal is filtered out, the DC value of each pFOV is lost, as shown in Figure 1.7(a), rendering the signal non-quantitative. Dr. Kuan Lu from our lab has devised a DC recovery method which minimizes the difference between overlapping segments of the pFOVs to restore the native MPI image (Figure 1.7). With this algorithm, x-space MPI has been experimentally proven to be Linear Shift-Invariant (LSI) [5]. Therefore, x-space MPI images can be used to quantify SPIO tracer *in vivo* anywhere in the imaging volume.

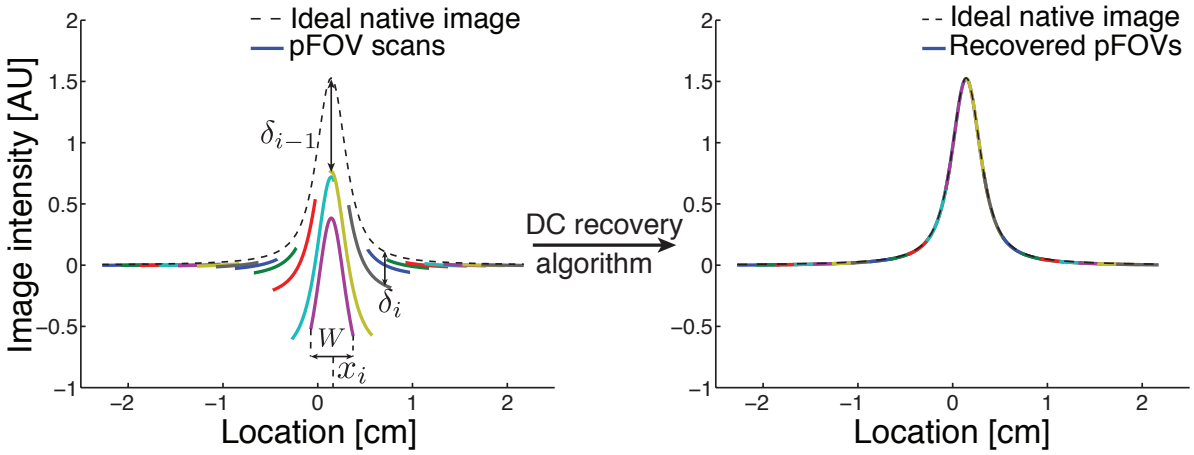

Figure 1.7: **DC Recovery of MPI Signal.** *Left*: pFOV scans with lost DC information due to direct feedthrough interference. *Right*: The DC recovery algorithm restores the lost DC offsets to each pFOV. The reconstructed image closely matches the ideal native MPI image. Image courtesy of Dr. Kuan Lu [5], Copyright ©2013, IEEE.

1.2.5 Improving MPI Resolution

Based on x-space MPI theory [4], the SPIO response in magnetization to applied field can be described in the following form:

$$M(H) = Nm\mathcal{L}(kH) \tag{1.1}$$

where $k = \dfrac{\mu_0 m}{k_B T}$ and $m = \dfrac{M_{sat}\pi}{6d^3}$. N is the number of particles per unit volume, μ_0 is the vacuum permeability, k_B is the Boltzmann's constant, T is the temperature, and d is the particle diameter. m is the magnetic moment of a spherical single domain magnetic nanoparticle, where M_{sat} is 0.6 T/μ_0 for SPIOs [9].

The imaging 1D PSF is the derivative of the magnetization as follows:

$$\dot{\mathcal{L}}(kH) = Nm\left(\frac{1}{(kH)^2} + \frac{1}{\sinh^2(kH)}\right) \tag{1.2}$$

The resolution of the system can be characterized by the full width at half maximum (FWHM), which can be analytically described as follows [4]:

$$FWHM_x = \frac{24k_BT}{\mu_0\pi M_{sat}}G^{-1}d^{-3} \tag{1.3}$$

where G [A/m/m] is the selection field gradient strength. As you can see, the resolution of MPI is fundamentally governed by selection field gradient strength and nanoparticle prop-

erties. In this work, we aim to build a high gradient FFL selection field to improve imaging resolution.

Chapter 2

Magnetic Particle Imaging: A Novel *in vivo* Imaging Platform for Cancer Detection

2.1 Introduction

2.1.1 Cancer Imaging: State-of-the-art

Biomedical imaging plays a key role in every phase of clinical cancer management, starting from initial screening through diagnosis, staging, treatment planning, and treatment monitoring [50]. The defining challenge in all cancer imaging is to robustly distinguish tumor from healthy tissue. Current anatomical imaging techniques such as X-ray, X-ray computed tomography (CT), ultrasound, and MRI are very useful for detecting tissue architecture changes that generally accompany cancer, but the native contrast of tumors may not differ sufficiently from healthy tissues for a confident diagnosis, especially for metastatic or diffuse tumors [51]. Hence, exogenous contrast agents such as Iodine (for X-ray CT), Gadolinium (for MRI), microbubbles (Ultrasound) and ^{18}FDG or ^{99m}Tc (for PET and SPECT) are often administered to highlight crucial physiologic contrast between normal and cancerous tissue for screening, diagnosis, staging, and treatment planning. These agents are all injected intravenously but their method of highlighting tumors differs considerably. Nuclear medicine uses metabolic tracer reporters, which preferentially accumulate in cancer due to the enhanced metabolic activity of tumors. Iodine and Gadolinium-based contrast agents distribute throughout the extracellular space and are cleared rapidly by glomerular filtration. This simple process has been exploited extensively in radiology to indirectly highlight tumors [51].

Nano-sized agents are known to be advantageous over conventional low molecular weight agents for several reasons. Nano-sized agents that are carefully designed to be large enough to escape excretion by the kidney, yet small enough to prevent immediate clearance from the reticuloendothelial system (RES), are able to circulate in the blood for extended peri-

ods of time. In some tumors, leaky vasculature permits these long-circulating nano-sized agents to preferentially leak into tumor tissue where they are then retained in the tumor bed due to reduced lymphatic drainage. This process is known as the enhanced permeability and retention (EPR) effect [41, 42, 43]. Physicians choose the ideal diagnostic imaging modality for each clinical presentation based on complex trade-offs between spatial resolution, sensitivity, contrast, access, cost, and safety. X-Ray systems, including CT, have mmol/kg sensitivity to iodinated contrast [52]. Gd-MRI T1 agents show *positive contrast*, with relaxivity of 5 Hz/mM [53], showing roughly 200 micromolar gadolinium concentration sensitivity. Superparamagnetic iron oxide (SPIO) nanoparticles, on the other hand, have a much larger effect on the MRI signal with the trade-off that they typically show T2* "negative contrast," which is difficult to distinguish from tissues such as bone, tendon and the lung. PET and nuclear medicine has exquisite sensitivity, ranging from nmol/kg to pmol/kg [52]. However, preparation of radiopharmaceuticals is expensive and requires cumbersome "hot chemistry". Moreover, nuclear medicine relies heavily on ^{99m}Tc (6-hour half-life) and ^{18}FDG (2-hour half-life), which fundamentally limits the duration of pathophysiology one can monitor with these radionuclides. Longer half-life tracers are available for monitoring slowly evolving pathophysiology (e.g., Indium 111 2.8-day half-life), but the longer half-life involves either greater net dose to the patient or weaker SNR. Indeed, X-ray, CT, and nuclear medicine expose patients to ionizing radiation and contrast media used for MRI and CT can be harmful to patients, especially patients with Chronic Kidney Disease (CKD). Due to the risks, and in many cases low diagnostic benefit due to insufficient contrast as well as high cost, most existing imaging techniques are carefully evaluated before incorporation into the cancer management workflow.

2.1.2 Magnetic Particle Imaging for Cancer Detection

Magnetic Particle Imaging (MPI) [3, 4, 14, 54], introduced by Philips Research in 2005, is a tracer imaging modality that directly measures the location and concentration of SPIO nanoparticles *in vivo*. MPI images the SPIO electronic moment, which is 22-million times more intense than **nuclear** MRI moments [55]. During signal generation, the application of a time-varying homogeneous excitation field causes SPIOs to instantaneously flip, thereby inducing a signal in the receive coil. To localize this signal, a field-free point (FFP) is created with a strong magnetic gradient. All particles outside the FFP are saturated, and only the particles at the FFP are able to flip when an addition of time-varying homogeneous excitation field is applied to the imaging field of view (FOV). The FFP is then rastered throughout the FOV, and the signal detected is assigned to an image location corresponding to the instantaneous location of the FFP [36]. This imaging process is illustrated in Figure 2.1(a). Note that this is just one of the many possible trajectories suited for FFP MPI [54, 56].

MPI is linearly quantitative, as shown in Figure 2.1(c). Although an ensemble of particles responds nonlinearly to an applied magnetic field, the voltage induced in the receiver coil is directly proportional to the amount of iron present at the FFP. MPI is also highly sensitive,

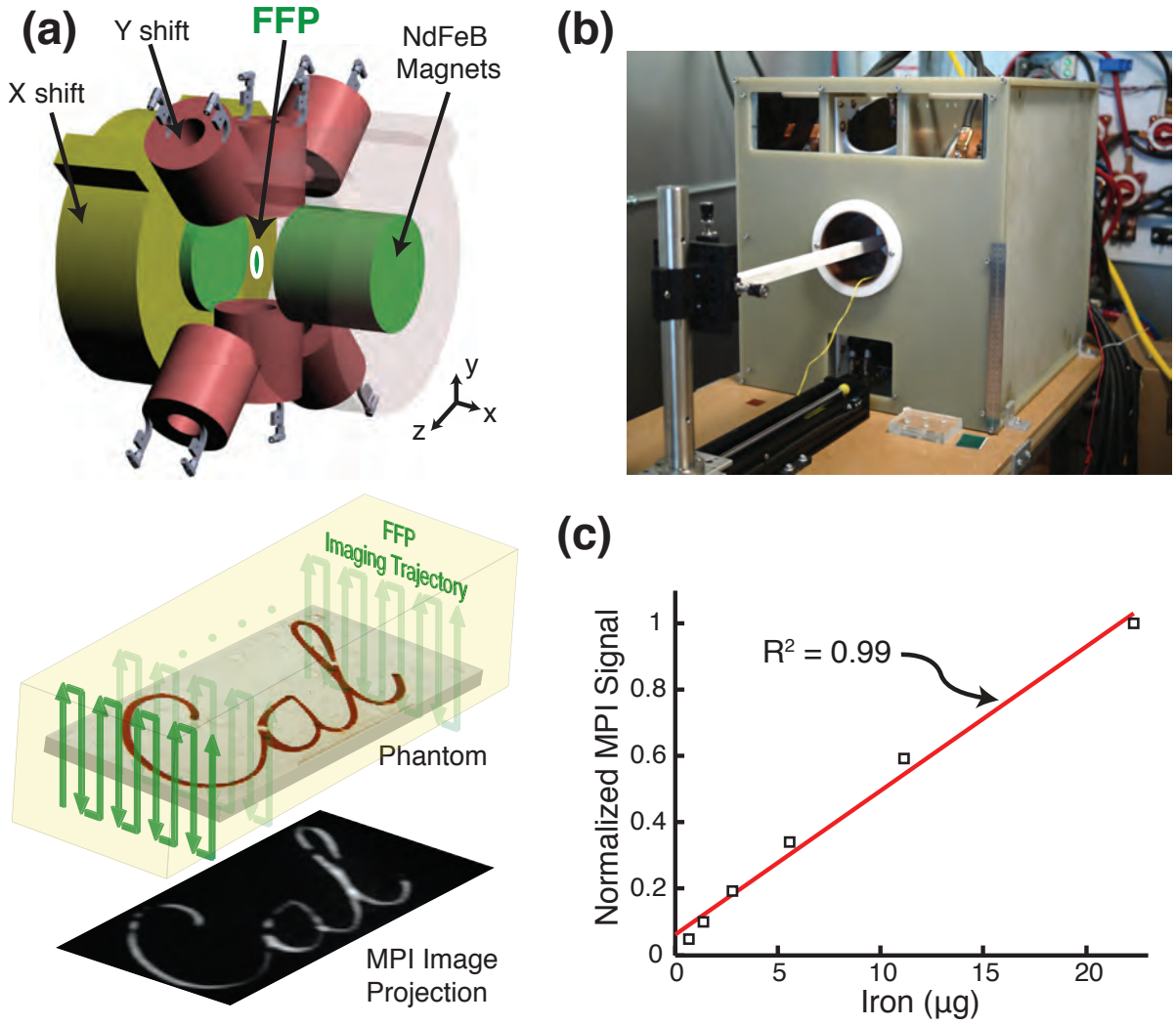

Figure 2.1: **Field-Free Point (FFP) Magnetic Particle Imaging.** (a) Illustration of 3D FFP Magnetic Particle Imaging. A magnetic field gradient is created with NdFeB permanent magnets (green) and the FFP is shifted in x- and y-directions with electromagnets (yellow and red, respectively), and the animal bed is translated via a motor in the z direction. The FFP follows the specified trajectory through the sample in the FOV as shown, and a 3D MPI image is acquired. A maximum intensity projection of the 3D MPI image is shown. (b) Photograph of our custom-built FFP MPI scanner. (c) Plot of MPI signal from six samples of LS-008 particles from Lodespin Labs with concentrations ranging from 36 μg Fe/mL to 1.2 mg Fe/mL. SPIO signal in MPI is linear with SPIO concentration (r^2= 0.99).

detecting nanograms of iron (or 200 labeled cells) per voxel [2, 24]. The current resolution with MPI-tailored SPIOs [13, 57] is approximately 1 mm, but may improve to better than

300 μm resolution with optimized nanoparticles, improved imaging hardware, and pulse sequences [58]. In addition, due to the low frequency magnetic fields used in MPI, there is zero signal depth attenuation from biological tissue, and there is zero signal from the tissue itself – only particle signal is visualized. This high contrast is highly enabling, as it allows clear visualization of tissue perfusion and targeting processes. In addition to producing no ionizing radiation, iron-oxide tracers are also safe, some of which are clinically approved as MRI contrast agents [39, 59]. Hence, it is safe to repeat serial scans on an animal or human. At present, no human MPI scanner has been developed, but the small animal MPI scanners are comparable in complexity to MRI scanners, so clinical translation should be feasible. The superb contrast, sensitivity, safety, and ability to image anywhere in the body gives MPI great promise for cancer imaging.

In this study, we show for the first time the use of MPI for *in vivo* cancer imaging. We used the first MPI-tailored particles which exhibit superior resolution, circulation time, and SNR over existing MPI tracers, which was invaluable for this study. We intravenously administered the SPIOs in tumor bearing rats and monitored the dynamic *in vivo* distribution of SPIOs using MPI over a period of 6 days. Due to the high contrast inherent to MPI, we captured clear images of the nanoparticle dynamics in the tumor and measured vascular wash-in, accumulation due to Enhanced Permeability Retention (EPR) effect, and subsequent clearance. The high contrast images also enabled quantitative analysis on tracer dynamics.

2.2 Methods and Materials

2.2.1 Magnetic Particle Imaging

A custom-built FFP MPI imager was used for this study, the construction of which is previously described [60, 61]. The 3D MPI scanner has a drive field frequency of 20.225 kHz and an excitation strength of 40 mTpp. The FFP is created with NdFeB permanent magnets (gradient of 7 $\times$ 3.5 $\times$ 3.5 T/m) and shifted with electromagnets following a trajectory through the field of view. All images were reconstructed using x-space MPI reconstruction algorithm [4, 5, 36]. Each z frame, as shown in Figure 2.1(a), covers a FOV of 40 mm $\times$ 40 mm $\times$ 1.66 mm, and is separated into 48 lines in the x direction. The z frames (5.76 seconds per frame) are acquired at 2 mm increments, allowing for the stitching required in x-space MPI reconstruction.

2.2.2 Magnetic Nanoparticle Synthesis and Characterization

MPI-tailored SPIO tracer (LS-008, LodeSpin Labs) was synthesized [14, 45] to achieve optimal resolution and blood circulation half-life. The iron oxide nanoparticles were synthesized by thermolysis of iron III oleate in 1-octadecene, with subsequent oxidation to achieve desired magnetic behavior using a mix of 1 % oxygen in argon [62]. Biocompatible

poly(maleic anhydride alt-1-octadecene) (PMAO)-PEG(20k) coatings were prepared by attaching 20 kDa Methoxy-PEG-amine (JenKem USA) to PMAO (Sigma) (30-50 kDa) [45]. The iron-oxide nanoparticles were then coated with amphiphilic polymer coating and dispersed in PBS buffer for characterization and animal studies.

Bright field TEM and Selected Area Electron Diffraction (SAED) were performed at 200 keV to characterize nanoparticle morphology and size, and crystalline phase, respectively. For size determination, n=1,960 particles were analyzed from 4 different images at 195k magnification. Inverse spinel (magnetite/maghemite) phase structure was confirmed by SAED. Blood half-life of the tracer was determined by fitting MPS signal data to a first-order pharmacokinetic elimination profile (single exponential decay). Hydrodynamic size of the coated nanoparticles was measured in PBS using Dynamic Light Scattering (DLS, Malvern ZetaSizer Nano ZS). Magnetic properties were measured by VSM (Lakeshore) and by a custom-built magnetic particle spectrometer MPS. Magnetic size was determined by fitting of M(H) data to a Langevin function (following Chantrell's method [63]).

Tracer was injected in the tail vein of female CD-1 mice (7 weeks old, n = 9) at 5 mg Fe/kg dose. Tracer blood half-life was then characterized according to a previously published method [57] based on *ex vivo* Magnetic Particle Spectrometry (MPS) measurements of blood drawn at various time points during circulation. Using MPS, the magnetization response of SPIOs in an AC field can be measured, allowing quantitation of SPIO concentration in the collected blood samples. These animal procedures were approved by the IACUC at University of Washington.

2.2.3 *In vivo* MPI Cancer Imaging

We evaluated the potential of *in vivo* MPI cancer imaging in 7 athymic nude rats bearing xenograft breast tumors. The animals were prepared by subcutaneous implantation of 7 million MDA-MB-231-luc cells. The presence of the tumor was confirmed with optional bioluminescence imaging (IVIS Lumina) after intraperitoneal injection of luciferin substrate. MPI-tailored long circulating SPIO tracer (LS-008) was administered systemically through the tail vein 4 weeks post tumor implantation.

The animals were separated into 3 groups, Groups A, B, and C. In Group A (n = 3), the tumors were implanted in the left lower mammary fat pad and LS-008 was intravenously administered at a dose of 15 mg/kg. MPI images with a field of view (FOV) of 40 mm × 40 mm × 85 mm were captured for these rats with respiratory gating over 5 minutes. The FOV captured only the lower abdomen where the tumor was present, along with and part of the liver and spleen. In Group B (n = 3), the tumors were implanted at the right lower flank and LS-008 was intravenously administered at a dose of 5 mg/kg. Here, MPI images with a FOV of 40 mm × 40 mm × 145 mm were captured with respiratory gating over 9 minutes. The whole body tracer biodistribution was captured. In Group C (n = 1), control animal had no tumor and was injected with LS-008 at a dose of 15 mg/kg, with the same imaging protocol as Group A. For reference, the ranges of dosages reported for human and small animal imaging studies in literature are 0.5 – 7.3 mg Fe/kg and 0.0145 – 56 mg Fe/kg,

respectively [12, 39, 64]. For animals in Groups A and C, MPI scans were acquired at 10, 30 minutes, 1, 2, 4, 6 hours, and 1, 2, 4, 6 days. For Group B animals, MPI scans were acquired at 10, 30 minutes, 1, 3, 6, 9, 12 hours, and 1, 2, 4, 6 days. These animal procedures were conducted in accordance to the National Research Council Guide for the Care and Use of Laboratory Animals and approved by the UC Berkeley Animal Care and Use Committee. The experimental workflow is illustrated in Figure 2.2.

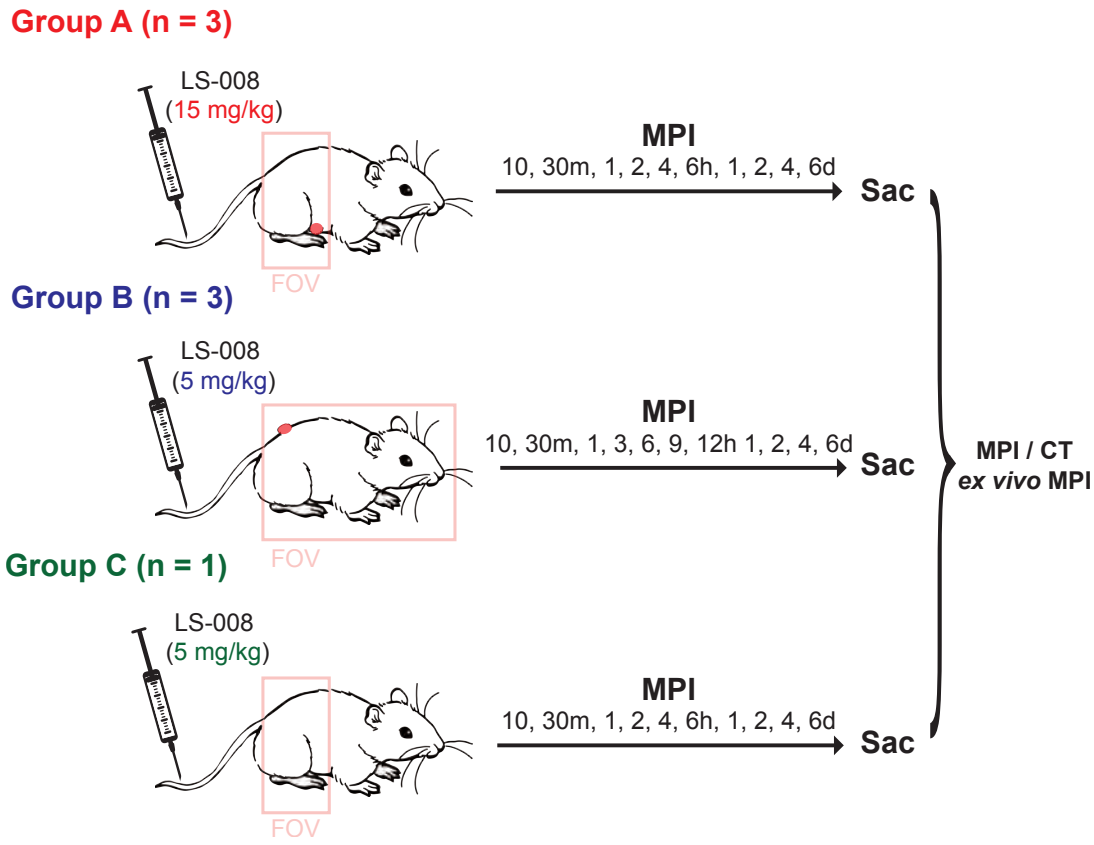

Figure 2.2: **Experimental Workflow.** Rats were separated into 3 groups. In Group A (n = 3), the tumors were implanted in the left lower mammary fat pad and LS-008 was intravenously administered at a dose of 15 mg/kg. In Group B (n = 3), the tumors were implanted at the right lower flank and LS-008 was intravenously administered at a dose of 5 mg/kg. In Group C (n = 1), control animal had no tumor and was injected with LS-008 at a dose of 15 mg/kg. The MPI FOV in Groups A and C covered the lower abdomen only, where as the FOV in Group B covered the entire body. MPI scans were acquired at multiple time points up to 6 days, followed by CT and *ex vivo* MPI.

2.2.4 *Ex vivo* MPI and Histology

Post-mortem CT scans were acquired on a RS9-80 Micro CT scanner (GE) with 17-minute acquisition time and 93 μm isotropic resolution for anatomical reference. The heart, lung, liver, spleen, kidneys, tumor, as well as samples of the muscle and skin were dissected and imaged with MPI to confirm tracer presence. Corresponding photographs of ex vivo scan layout were taken for reference.

After ex vivo MPI, the tumors, liver, and spleen were fixed in neutral buffered formalin (NBF) and transfered to 70 % ethanol after 24 hours. Each tissue sample was placed in a pre-labeled cassette for automated processing on the Ventana Renaissance. The automated tissue processing protocol consists of 45 exchanges in 70 %, 95 % ($\times$3), and 100 % ($\times$3) ethanol, followed by three exchanges in xylene and three exchanges in paraffin. Upon completion of overnight processing, the cassettes were removed from the processor and placed in the Rushabh embedding station. Embedding was done by standard methods using metal molds, hot paraffin dispenser, and cold plate.

The formalin-fixed paraffin-embedded (FFPE) tissue samples were sectioned at 5 μm thickness. Hematoxylin and eosin (H & E) staining was performed for morphological analysis. FFPE sections were stained for ferric iron using the Iron Stain Kit (Diagnostic BioSystems, Cat. #KT021); staining was performed according to protocol provided by manufacturer. Macrophages were stained for the CD68 maker using an anti-CD68 antibody (Abcam, Cat. #ab125212) at a final concentration of 2 μg/mL. A rabbit IgG antibody was used at the same concentration as an isotype control. FFPE sections were stained on the Biocare IntelliPATH$^{\text{TM}}$ automated platform using a heat-induced antigen retrieval method: Diva Decloaker (proprietary citrate-based buffer, pH 6.2). Detection of mouse antibodies was done using an anti-mouse secondary reagent followed by the Biocare intelliPATH$^{\text{TM}}$ FLX Universal HRP polymer system. Stained slides were digitized with a TissueScope LE whole slide scanner (Huron Digital Pathology) at 20$\times$ magnification. Photographs of individual tissues were captured with Huron Viewer software.

2.2.5 Quantitative Compartmental Analysis

For each 3D MPI volume, the MPI signal was first calibrated to a known concentration based on the calibration curve shown in Figure 2.1(c). Regions of interest (ROI) were identified for each organ in which the concentration is averaged. For the blood, the ROI was drawn in the left femoral artery. For two-compartmental fitting, the estimated blood pool volume of the blood pool based on weight of the animal and measured size of the tumor were used for one representative rat in each group.

2.3 Results

2.3.1 Magnetic Nanoparticle Characterization

Nanoparticle morphology and size were characterized with bright field TEM as shown in Figure 2.3(a). Crystalline phase as characterized by SAED is shown in Figure 2.3(a) inset. Inverse spinel (magnetite/maghemite) phase structure was confirmed by SAED. Tracer half-life in mice ($t_{1/2}$) was determined to be 105 ± 10 minutes ($R^2 = 0.99$), as shown in Figure 2.3(b). Hydrodynamic diameter of the coated nanoparticles was measured to be 90.7 nm (Figure 2.3(c)). Magnetic properties measured by VSM is shown in Figure 2.3(d)). Magnetic size was determined to be 26.3 nm by Langevin function fitting.

2.3.2 High Contrast MPI Cancer Imaging

For Group A rats (high dose, 15 mg/kg), a representative maximum intensity projection of the 3D MPI image acquired 6 hours after injection of long circulating LS-008 particles is shown with CT overly in Figure 2.4. The nanoparticle tracer preferentially accumulated in tumor due to Enhanced Permeability and Retention (EPR) effect, reaching peak enhancement at 6 hours. The tumor is seen with extraordinary contrast. Note that this level of contrast would be visible anywhere in the body, as MPI signal does not suffer from depth attenuation. In addition, MPI captures the 3D distribution of tracer throughout the body.

The corresponding bioluminescence image of the MDA-MB-231-luc xenograft tumor is also shown in Figure 2.4. As the implanted cancer cells are designed to express luciferase, upon injection of luciferin substrate, the tumor glows. Note that the tumor is implanted subcutaneously in this study. If the tumor were a just few millimeters deeper anywhere else in the body, optical imaging techniques would suffer significantly from signal depth attenuation. For this reason, bioluminescence imaging also cannot be used to quantitatively determine tracer biodistribution. This was used merely to confirm the presence of the tumor.

The tracer biodistribution through time in Group A rats is shown in Figure 2.5. The MPI images with a FOV of 40 mm × 40 mm × 85 mm were cropped to a FOV of 40 mm × 40 mm × 58 mm to focus on particle dynamics in the tumor. Coronal slices through the tumor were taken from the 3D volume and coregistered with corresponding CT slices for anatomical reference. The initial vascular wash-in is characterized by the rim enhancement of the tumor. This rim enhancement is difficult to visualize with such high contrast using other imaging modalities without parametric fitting or baseline subtraction. Consistent with the enhanced permeability and retention (EPR) effect reported in literature, nanoparticles preferentially accumulate in tumors due to their abnormally leaky vasculature [41, 43]. The dynamics of EPR effect is clearly captured with MPI, with a tumor-to-background ratio of up to 50 at 6 hours post injection. The nanoparticles are then gradually cleared from the tumor over time, with high contrast enhancement remaining at 24 hours. Due to the high contrast inherent to MPI and long tracer half-life, tracer present in the tumor was detectable as long as 6 days post injection.

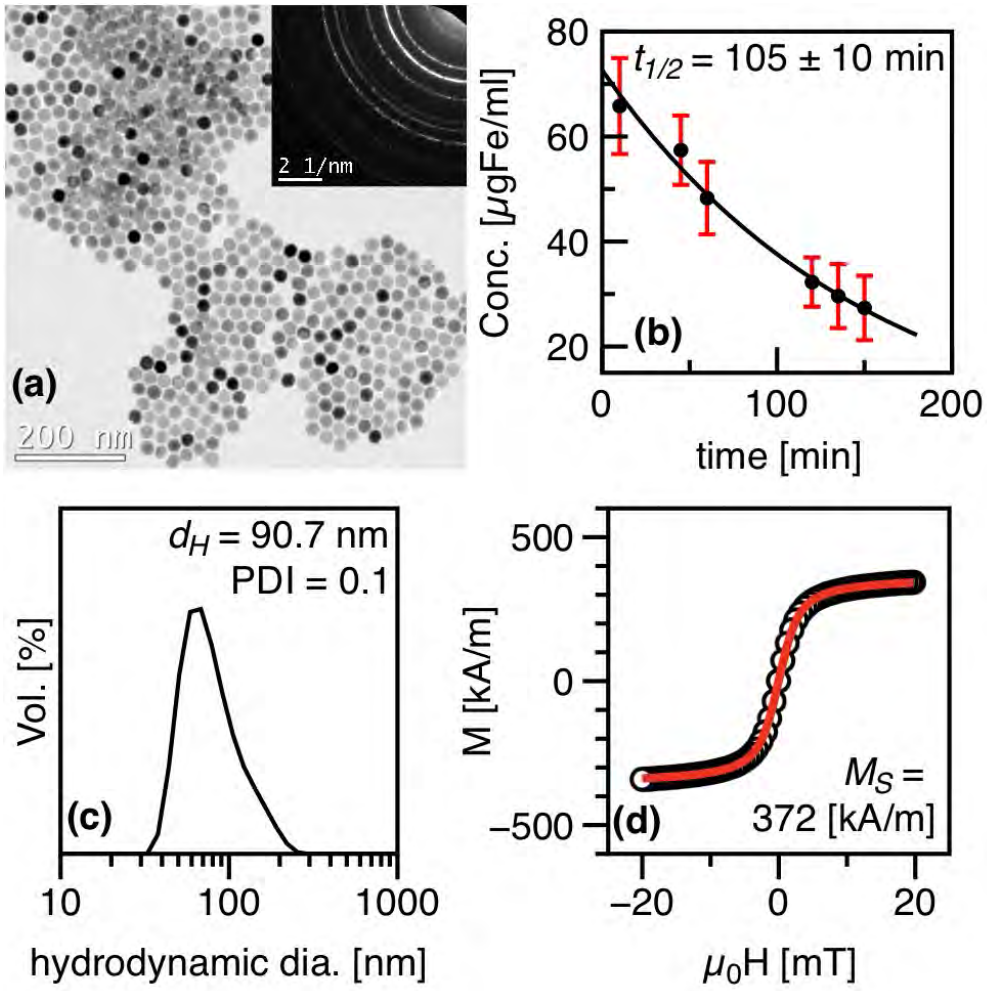

Figure 2.3: **LS-008 SPIO Characterization.** (a) Bright field TEM image of uncoated iron oxide cores of LS-008 and (inset) Selected Area Diffraction pattern showing crystal morphology and characteristic spinel diffraction rings. (b) MPS signal intensity vs. time of blood samples taken from female CD-1 mice following tail vein injection of 5 mg Fe/kg. (c) Hydrodynamic size measured by DLS. (d) Magnetization curves measured by VSM at room temperature.

2.3.3 Imaging Whole Body Tracer Dynamics with MPI

The tracer biodistribution through time in Group B rats (low dose, 5 mg/kg) is shown in Figure 2.6. Here, we measured the full body biodistribution with a FOV of 40 mm × 40 mm × 145 mm with an acquisition time of 9 minutes. Whole body maximum intensity projection (MIP) of the 3D MPI image volumes were coregistered with CT skeletal reference. As is apparent in Figure 2.6, the injected LS-008 particles are first distributed uniformly in the intravascular system, yielding a blood volume image. Organs with larger blood volume such

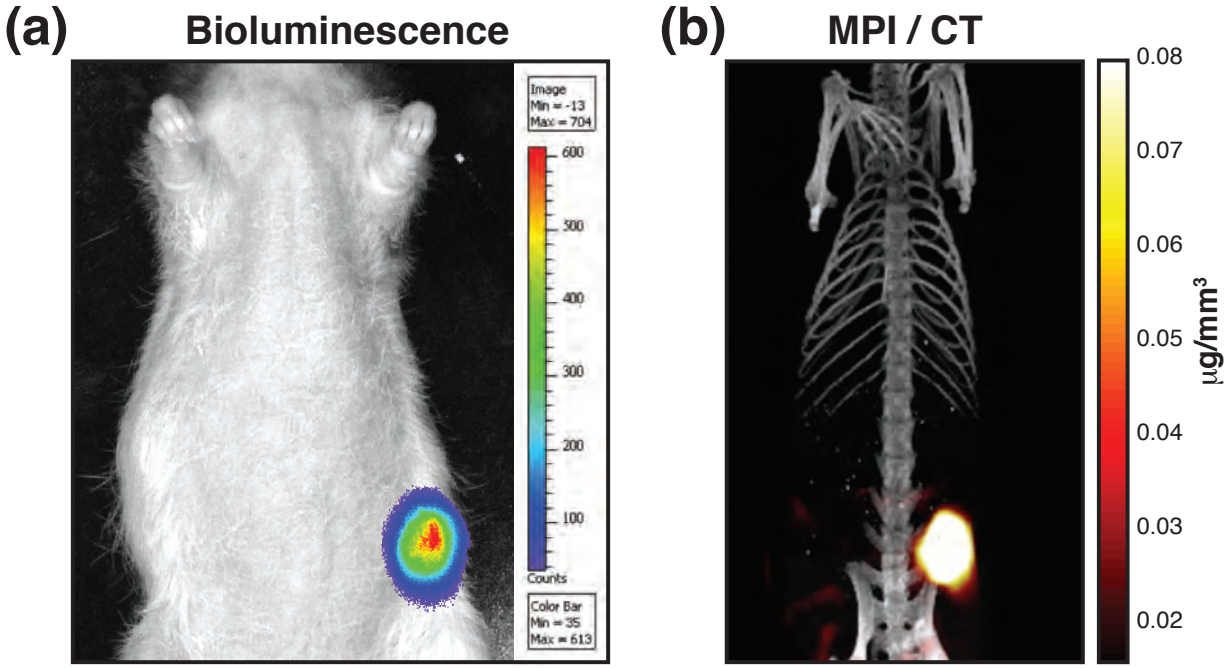

Figure 2.4: **BLI and MPI/CT image of Xenograft Tumor.** (a) Representative bioluminescence image of the MDA-MB-231-luc xenograft tumor. (b) Corresponding maximum intensity projection of the 3D MPI image (FOV: 40 mm × 40 mm × 58 mm) acquired 6 hours post injection with CT overlay.

as the heart and lungs are therefore distinguishable. Although specific biodistribution and clearance parameters depend on particle properties such as surface characteristics, shape, and size, iron oxide nanoparticles are primarily cleared from the blood by the RES [65]. Our MPI measurements confirm this: intravascular signal decreases gradually with time, while signal in the liver and spleen increase over time. Simultaneously, the contrast and sensitivity inherent to MPI allows for the tumor to be clearly visible through time. Since the tumors in this study are subcutaneous xenografts, the tumors are prone to slight shifts while being loaded into the scanner for each time point. This is reflected in the slight changes in tumor position in the MPI scans over time.

To better illustrate the entire MPI volume taken at each time point, maximum intensity projections of the 3D volume taken at 12 hours are shown in the sagittal, coronal, and transverse directions with CT overlay in Figure 2.7. As expected, the tracer is accumulated in the liver and spleen at this time due to nanoparticle clearance through the RES. Due to the high contrast and linearity inherent to MPI, the tumor is clearly visualized alongside the liver and spleen. Quantitative 3D tracer maps such as this one is captured at every time point, allowing whole body dynamic 3D analysis.

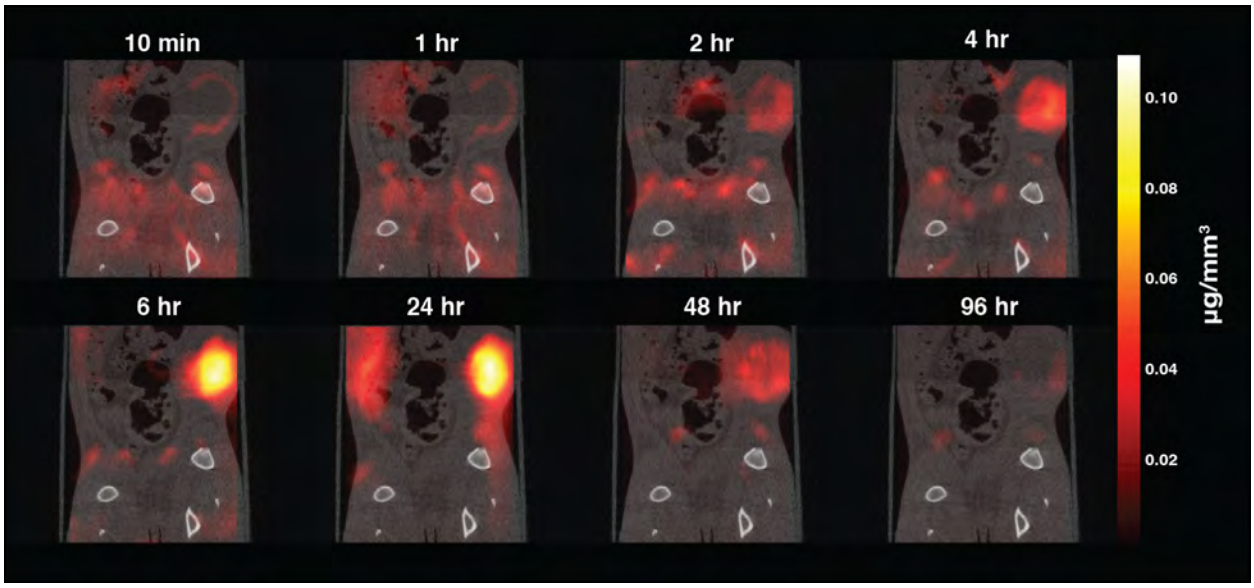

Figure 2.5: **Tracer Dynamics in Group A Rats.** Cropped FOV: 40 mm × 40 mm × 58 mm. Slices through the MPI volume over time are coregistered to corresponding CT slices and shown here. The exquisite contrast of MPI allows clear visualization of the dynamics: initial rim enhancement, followed by accumulation and then clearance.

2.3.4 Quantitative Compartmental Analysis and *ex vivo* Imaging

Due to the quantitative nature of MPI with zero depth attenuation, we were able to not only noninvasively track the biodistribution through time, but also model the tracer dynamics in a two compartment model. Biodistribution and compartmental fitting result of Group A and B animals are shown in Figure 2.8(a) and (b), respectively.

Group A was injected with 3-fold the dose of Group B, and the measured concentration of tracer in blood (derived directly from *in vivo* MPI signal) differed by 3-fold, as apparent in Figure 2.8(a) and (b). This gives us confidence in the quantitative nature of MPI for SPIOs *in vivo*. Tracer blood circulation half-life was calculated to be 4.25 ± 0.28 hours for group A (high dose) and 3.65 ± 0.71 hours for group B (low dose). This dose dependency of iron-oxide blood half-life due to progressive saturation of the macrophage uptake in macrophage-rich organs is a well-known phenomenon that has been demonstrated for various particle systems [66]. This could explain the relatively larger accumulation of particles in Group A tumors. Although EPR effect is known to passively target tumors, there is also a large variability of vascular development across tumor types and sizes. Therefore, it is well-known that EPR effect does not manifest in all tumors. We observed this variability in enhancement at later time points in our experiment as shown in the bottom panels of Figure 2.8(a) and (b). However, the initial vascular wash-in rim enhancement was readily apparent in all animals.

To confirm the presence of tracer, organs were dissected at the end point and imaged

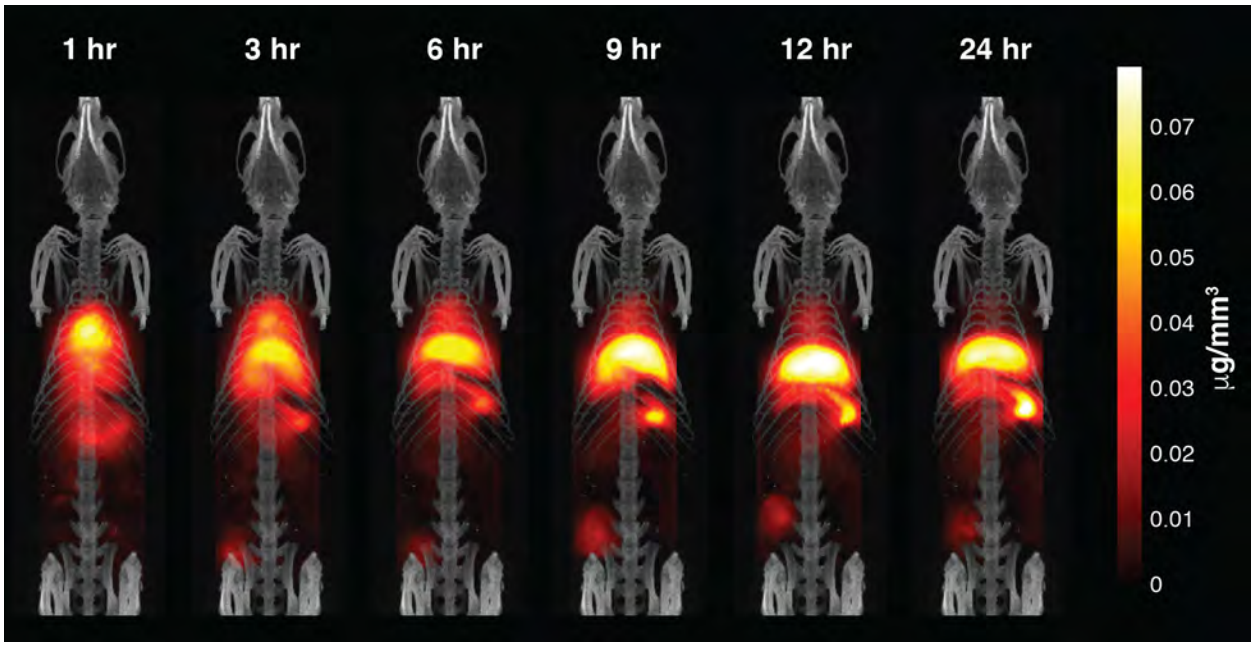

Figure 2.6: **Tracer Dynamics in Group B Rats.** Maximum intensity projection of 3D MPI volumes coregistered with a CT skeletal reference. The whole body tracer dynamics along with the tumor are clearly visualized.

with MPI as shown in Figure 2.8. Presence of SPIO signal was observed in liver, spleen, as well as the tumor 2 days post injection. In one case, the rat was sacrificed 6 days post injection, and SPIO signal was still observed in the tumor with a tumor to muscle signal ratio as high as 4.98.

2.3.5 Histology

Representative H & E and Prussian Blue images of the tumor, liver, and spleen are shown in Figure 2.10. Prussian Blue staining in control liver showed only speckles of iron deposits in macrophages and occasionally hepatocytes. In treated liver the staining revealed the presence of significant iron deposits within the cytoplasm of resident macrophages (Kupffer cells) and in small amount in the cytoplasm of hepatocytes. In both control and treated spleen the staining revealed the presence of a large number of iron-laden macrophages within the red pulp of spleen. Staining showed the presence of moderate number of macrophages containing iron deposits within the tumor stroma and mostly concentrated within the central part of the tumor.

To determine whether the iron particles were present in rat macrophages in the tumor, we stained for iron particles using Prussian Blue stain and for macrophages by IHC in sequential sections and evaluated the co-localization of the markers. As seen in Figure 2.11, a number of macrophages within the central stroma stained positive for both markers. However, there

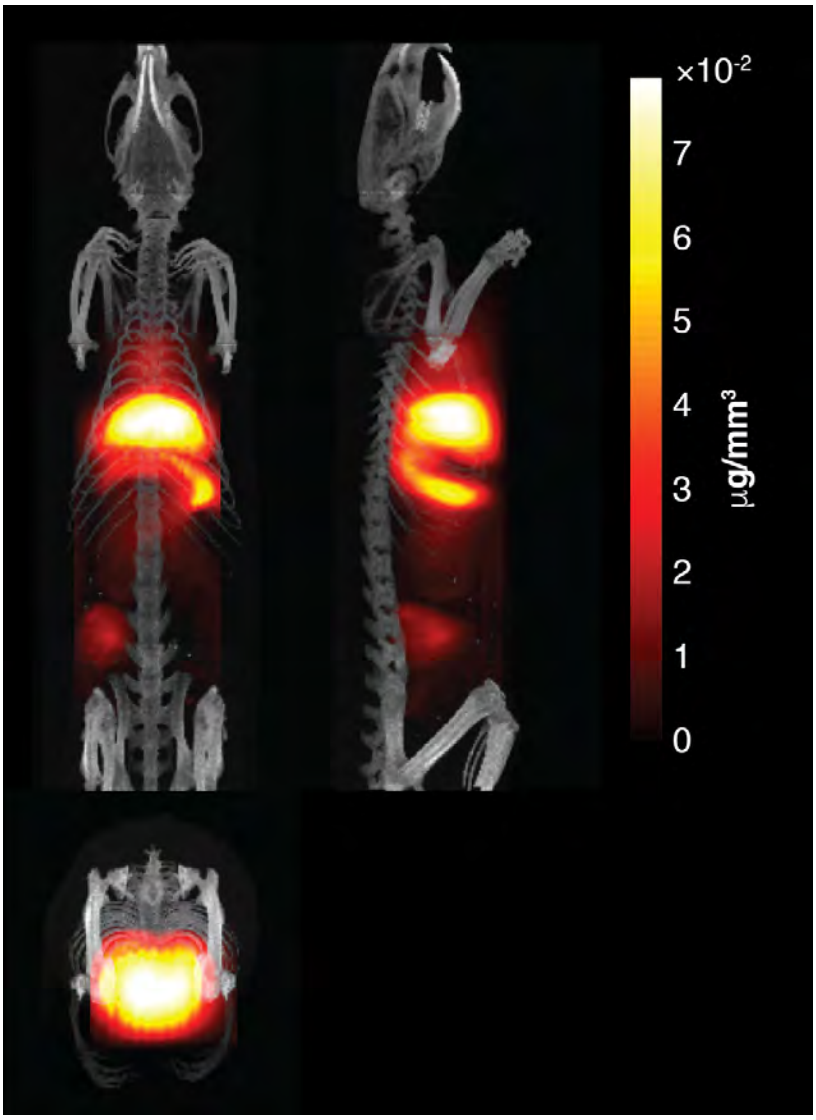

Figure 2.7: **Representative 3D MPI Volume of Group B Rats at 12 hours.** Maximum intensity projections of the 3D volume are shown in the sagittal, coronal, and transverse directions with CT overlay.

were numerous macrophages in other parts of the tissue that were positive for CD68, but not for iron.

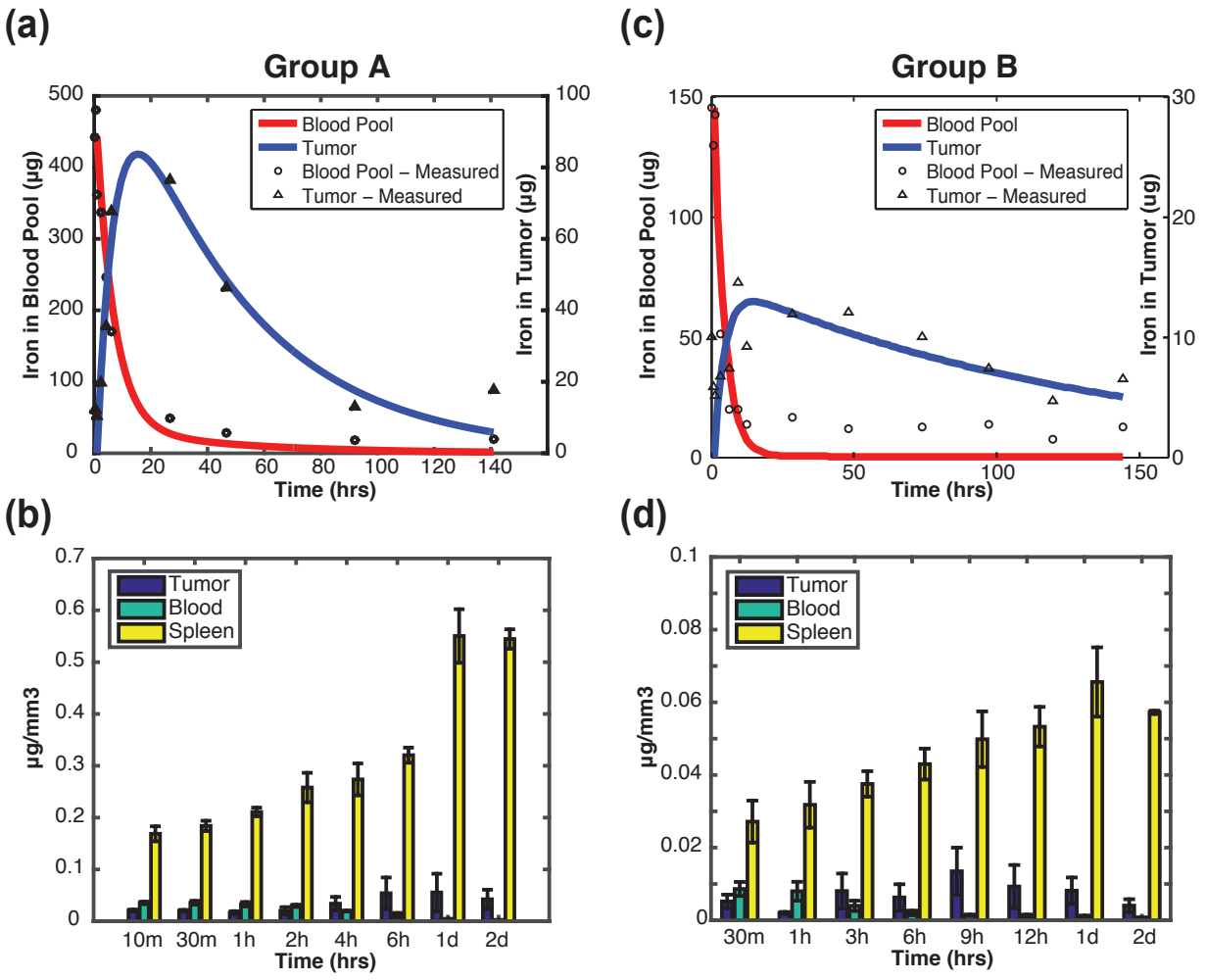

Figure 2.8: **Tracer Biodistribution and Compartment Model Fitting Results.** (a) Group A (n = 3) representative two-compartment model fitting result and (b) tracer biodistribution through time. (c) Group B (n = 3) representative two-compartment model fitting result and (d) tracer biodistribution through time.

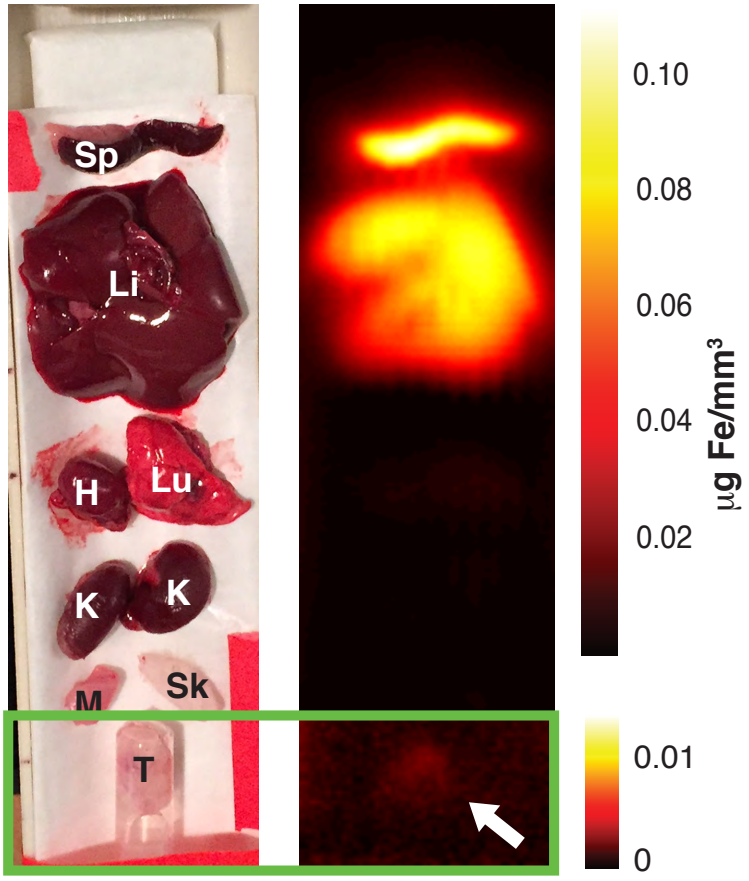

Figure 2.9: ***Ex vivo* MPI.** *Ex vivo* MPI scan (right) and corresponding photograph (left) 2 days post SPIO injection. Tracer is present in the liver, spleen, and tumor, confirming what is seen *in vivo*.

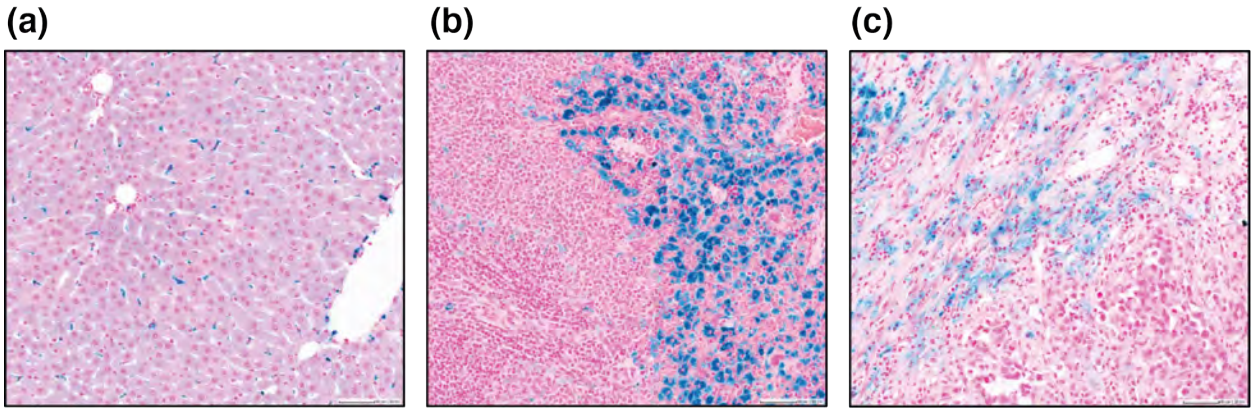

Figure 2.10: **H & E and Prussian Blue Histology.** Representative H & E and Prussian Blue images of the (a) liver, (b) spleen, and (c) tumor xenograft taken at 20× magnification.

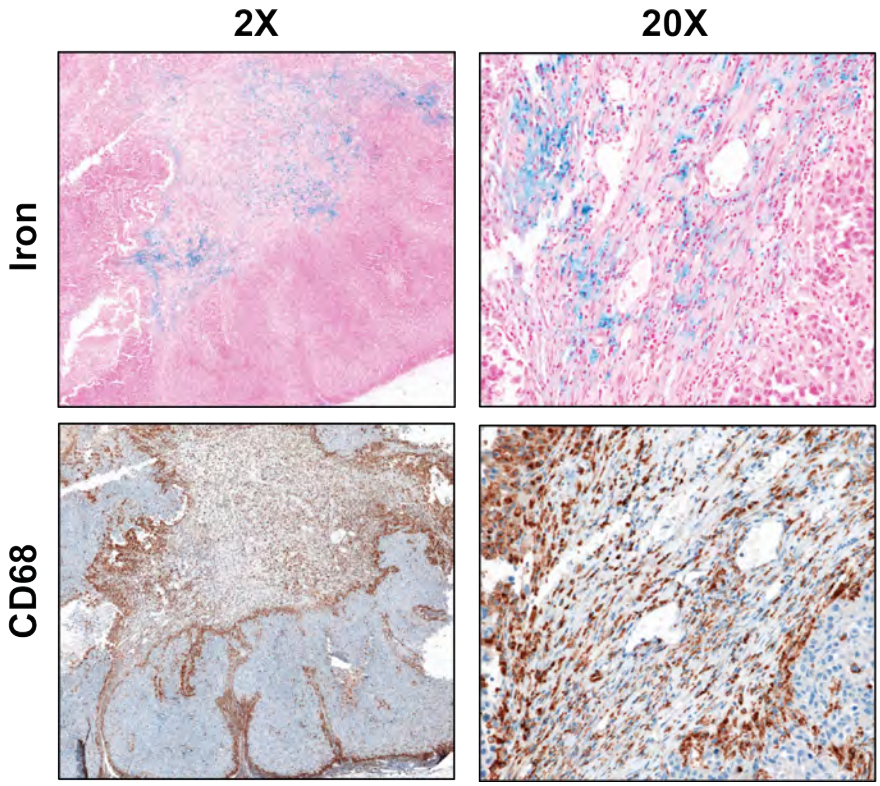

Figure 2.11: **Iron and Rat Macrophage Co-localization Histology.** Side-by-side comparison of sequential sections stained with Prussian Blue and CD68 shows iron-laden macrophages (blue) present in the central stroma of xenograft positive for macrophages marker CD68 (brown).

2.4 Discussion & Conclusion

This is the first demonstration of cancer detection with MPI through passive targeting – perfusion and EPR effect. Another study has shown MPI of direct SPIO injections into tumor [27]. Indeed, EPR effect is not without its limitations. There is significant heterogeneity within and between tumor types – different types of tumors have different pore dimensions in the vasculature and the maximum pore size changes with the location for a given type of tumor. Most studies demonstrating nanotechnology platforms that effectively exploit the EPR effect have been done in implanted tumors, with limited data on metastatic lesions [67]. Therefore, continued development is required before nanoparticles can be fully realized in clinical use for cancer. Our current SPIO tracer has around 2 hour circulation half-life in mice and around 3.5 hour half-life in rats, which may be adequate for cardiovascular imaging and for certain cancer studies as shown here. However, it may be the case that extended circulation time is attractive for improving the contrast of certain pathophysiology. For these applications, nanoparticles can be encapsulated in PEGylated PRINT nanoparticles with circulation half-life of 19.5 hours [68] or in red blood cells with tracer life span in the mice bloodstream prolonged to 12 days [69].

To improve the specificity of cancer imaging, researchers have bound the most common contrast agents and nuclear medicine tracers to moieties that are thought to home to tumor biomarkers, including peptides [70], antibodies [71], and cells [72]. These are all targeting strategies that can be realized with MPI. In particular, MPI is capable of *in vivo* non-invasive cell tracking with MPI with 200-cell sensitivity [2, 24, 25, 73]. Additionally, the use of relaxation and aggregation-based SPIO contrast mechanisms have been demonstrated [8, 74]. This may enable *in vivo* sensing of tumor micro-environment factors such as viscosity and pH to provide additional contrast.

There is a growing field of magnetic nanomaterial development for targeted drug delivery [75] and hyperthermia [76], many currently designed to be used as contrast agents in MRI [77]. Due to the inherently lower sensitivity and negative contrast of SPIOs in MRI, rim enhancement of the tumor as we have observed in this study with MPI is difficult to see with MRI, even with dosages as high as 27.92 mg Fe/kg. Tumor enhancement is seen at later time points in the center of the tumor [78], similar to what we have also observed in our study. There have been several promising demonstrations of MPI guided magnetic hyperthermia [27, 34]. In addition, we are in the early stages of demonstrating the potential for localized magnetic hyperthermia with simultaneous imaging using the existing gradient field in MPI [79]. It is evident that many cancer targeting strategies for magnetic nanoparticles are already widely investigated. MPI, with its superb sensitivity and contrast, is uniquely poised to harness this existing work to even more efficiently target and image cancer. Indeed, MPI can also serve as a powerful tool for researchers developing targeted magnetic nanoparticles, and may ultimately enable safe and high contrast cancer detection in the clinic.

2.5 Acknowledgement

This work was done in collaboration with lab members Mindy Bishop, Dr. Bo Zheng, Dr. Prashant Chandrasekharan, and David Mai. The FFP MPI scanner used for this study was built by Dr. Patrick W. Goodwill. CT scans for anatomical reference were done with the help of Dr. Michael F. Wendland at the Berkeley Preclinical Imaging Center (BPIC). Histological sectioning and staining was done by Ensigna Biosystems, Inc. MPI-tailored long circulating SPIOs work was done in collaboration with University of Washington and Lodespin Labs, LLC: Dr. Amit P. Khandhar, Dr. R. Matthew Ferguson, Dr. Scott J. Kemp, and Prof. Kannan M. Krishnan.

Chapter 3

High Resolution Field-Free Line Magnetic Particle Imaging

3.1 Introduction: Field-Free Line MPI Theory

A field-free line (FFL) is a full line in space of zero magnetic field which localizes signals from SPIOs along a line. In our system, the FFL is along the y-axis. Rastering this line in x-direction and z-direction yields a projection image of particle concentration. The reduced dimensionality from 3D to 2D enables an order of magnitude speed improvement over the FFP format [17]. This is highly enabling, as in many applications, high speed is crucial, and projection images are sufficient for diagnostic information. A prime example of this is X-ray fluoroscopy which is used for real-time imaging in the clinic. The real-time video feed is used for diagnosis as well as guidance for surgery, catheter placement, biopsy, and more. Since there is only signal from the SPIOs in MPI, there is no anatomical reference as there is in X-ray. However, in many cases, high contrast with no anatomical background is desirable. For applications such as angiography, blood pool imaging and perfusion imaging, high contrast and high speed are both essential, and only signal from the blood vessels are of interest. Other applications such as investigations of the gastrointestinal tract (barium swallow in X-ray) also leverage the high contrast and speed for diagnosis. Note that SPIO tracer is much safer than iodine and gadolinium agents for patients with Chronic Kidney Disease (CKD), and no ionizing radiation is used. This unprecedented combination of high contrast, speed, and safety can potentially open doors for new applications.

When a projection format is coupled with rotation of the scanner or imaging specimen, a 3D imaging volume can be reconstructed. This is done by filtered back projection (FBP), a projection reconstruction algorithm commonly used in Computed Tomography (CT). Each projection, acquired at angle θ, is filtered with a ramp filter, and subsequently projected onto the resulting imaging volume at θ [37, 80]. See Figure 3.1 for an illustration of an angular projection at θ. The projection angle θ is varied between 0–180 degrees. All the back-projected images are then summed for the resulting image. Due to projection acquisition

capabilities, coupled with rotation, FFL MPI is capable of projection reconstruction, or magnetic computed tomography.

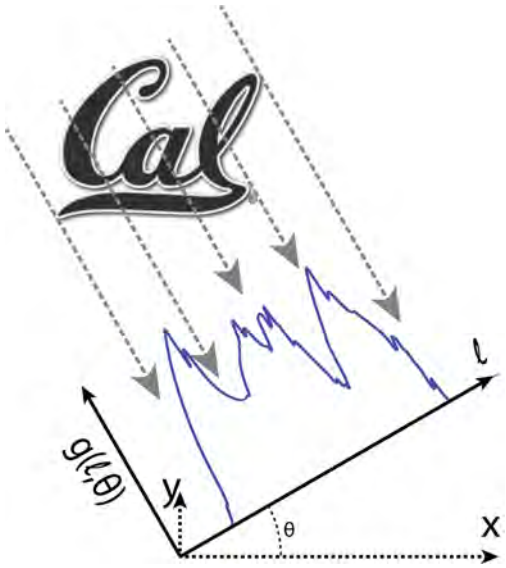

Figure 3.1: **Projection Reconstruction in MPI.** Shown here is a projection of our "Cal" object being taken at angle θ to result in the line profile $g(l, \theta)$. Projection angle θ can be varied to acquire multiple projection. Projection reconstruction is then performed using the acquired projections to recreate the "Cal" image.

Theory and simulation studies for various designs of FFL MPI magnets have been performed to demonstrate the potential SNR gain of projection reconstruction MPI over traditional FFP MPI imaging [81, 82, 83, 84, 85]. Dr. Justin Konkle from our lab has experimentally validated the SNR and resolution benefits of projection reconstruction MPI over traditional FFP MPI. The resolution benefits arise from image sharpening from the ramp filter, and the SNR improves $\propto \sqrt{N}$, where N represents the number of projections acquired [6, 37]. In fact, with the same image acquisition time, projection reconstruction MPI has the potential to increase SNR by an order of magnitude over a 3D scan with a FFP MPI scanner due to signal averaging. This sensitivity gain is highly empowering for applications such as cell tracking, where picogram levels of iron are present in each cell. The sensitivity can also be traded off for imaging speed based on the application. In the following section, I will briefly introduce the theoretical imaging point spread function (PSF) for projection MPI and projection reconstruction MPI.

A linear representation of the selection field gradient is necessary for the derivation of the theoretical imaging PSF. In multidimensional x-space MPI, the 3D linear gradient in the following form [36, 86]:

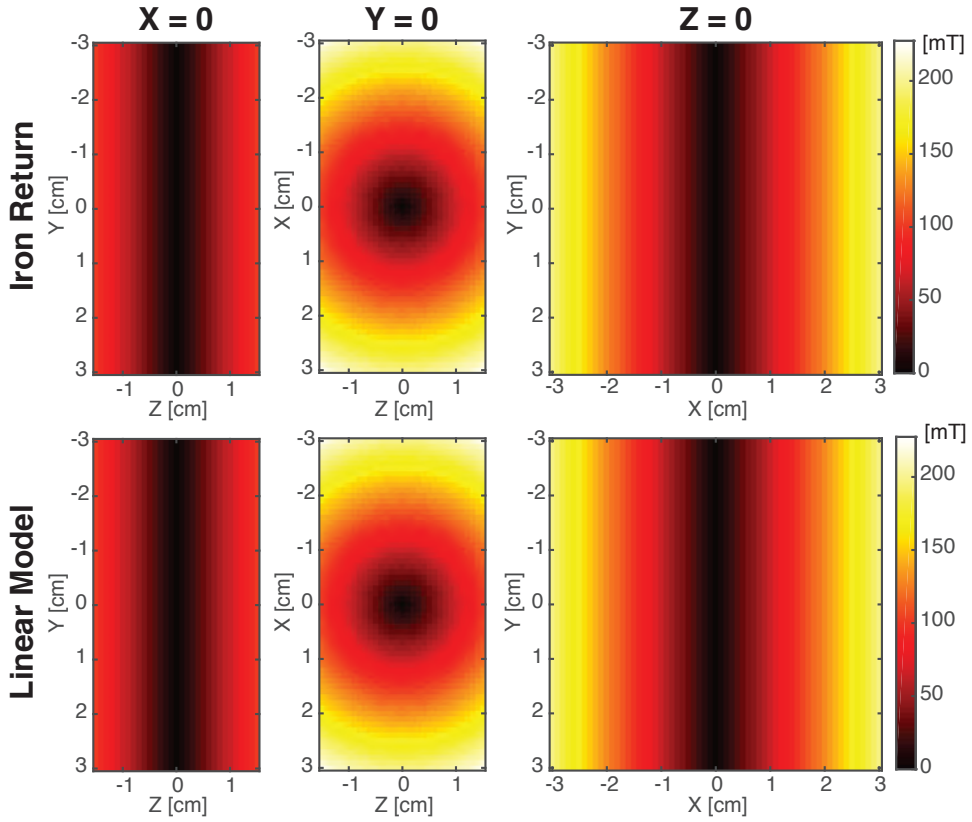

Figure 3.2: **Linear Estimation of Magnetic Field Gradient.** *Top row*: simulated field contour from our iron return FFL magnet. *Bottom row*: corresponding field contour calculated from a linear gradient matrix. This matrix is used to determine our theoretical PSF. Note that the two field contours closely resemble each other, lending us confidence in our theoretical PSF.

$$\mathbf{H}(\mathbf{x}) = \mathbf{G}\mathbf{x} = \begin{bmatrix} -\alpha G_{zz} & G_{xy} & G_{xz} \\ G_{xy} & (\alpha - 1)G_{zz} & G_{yz} \\ G_{xz} & G_{yz} & G_{zz} \end{bmatrix} \begin{bmatrix} x \\ y \\ z \end{bmatrix} \tag{3.1}$$

where $\mathbf{x} = [xyz]^T$ represents position in space, and G is the gradient matrix. The trace of matrix G is zero, consistent with Maxwell's Equations in a source-free space [87]. An FFL gradient where $\alpha = 1$ and all the cross terms G_{xy}, G_{xz} and G_{yz} are all zero is physically realizable:

$$\mathbf{G} = \begin{bmatrix} -G_{zz} & 0 & 0 \\ 0 & 0 & 0 \\ 0 & 0 & G_{zz} \end{bmatrix} \tag{3.2}$$

The FFL in our system is created using an iron return electromagnet. The field map calculated from our iron return electromagnet can be approximated by the 3D linear gradient form (Figure 3.2). As you can see, the field map from the iron return simulation closely resembles that of $\mathbf{H}(\mathbf{x}) = \mathbf{G}\mathbf{x}$. The method used to simulate the iron return electromagnet will be described in more detail in Section 3.2.2. The particle signal from the location of the FFL is detected as a sum, hence a projection along the direction of the FFL is made.

Based on the linear gradient matrix, the multidimensional MPI PSF is defined as follows [36]:

$$\mathbf{h}(\mathbf{x}) = \dot{\mathcal{L}}[\left\|\mathbf{G}\mathbf{x}\right\|/H_{sat}]\frac{\mathbf{G}\mathbf{x}}{\left\|\mathbf{G}\mathbf{x}\right\|}\left(\frac{\mathbf{G}\mathbf{x}}{\left\|\mathbf{G}\mathbf{x}\right\|}\right)^T\mathbf{G} + \frac{\mathcal{L}[\left\|\mathbf{G}\mathbf{x}\right\|/H_{sat}]}{\left\|\mathbf{G}\mathbf{x}\right\|/H_{sat}}\left(\mathbf{I} - \frac{\mathbf{G}\mathbf{x}}{\left\|\mathbf{G}\mathbf{x}\right\|}\left(\frac{\mathbf{G}\mathbf{x}}{\left\|\mathbf{G}\mathbf{x}\right\|}\right)^T\right)\mathbf{G} \tag{3.3}$$

where H_{sat} is the applied field necessary for saturation of the magnetic nanoparticles. The dimensionality of the matrix PSF is reduced due to the projection so that $\mathbf{h}(\mathbf{x}) \in \mathbf{R}^{2\times 2}$. The theoretical 2D xz PSF is shown in the left panel of Figure 3.3, and the profile of the PSF along the x- direction is shown in the top panel of Figure 3.4. Note that these are based on a particle diameter d of 25 nm, and a field gradient (G_{zz}) of 6.3 T/m. The particles with core diameter of 25 nm are used in both biomedical application studies in this thesis.

An image of the theoretical projection reconstruction PSF is shown in the right panel of Figure 3.3. This was created by conducting filtered back projection on the theoretical projection PSF. Notice that the FOV in x is reduced by $1/\sqrt{2}$ due to the sufficient sampling in the center of the FOV in the filtered back projection procedure [37]. The profile of the PSF in the x-direction is shown in the bottom panel of Figure 3.4. The FWHM comparisons of different particles used is shown in Table 3.1. Notice that the FWHM$_x$ is improved by 40% after projection reconstruction, as noted in [37].

		LS-008	Nanomag-MIP
Particle Core Diameter	[nm]	25	22.7
Projection FWHM$_x$	[mm]	1.59	2.12
Projection FWHM$_z$	[mm]	0.7	0.94
PR FWHM$_x$	[mm]	0.91	1.21
PR FWHM$_z$	[mm]	0.7	0.94

Table 3.1: Theoretical FFL Imaging Resolution at 6.3 T/m.

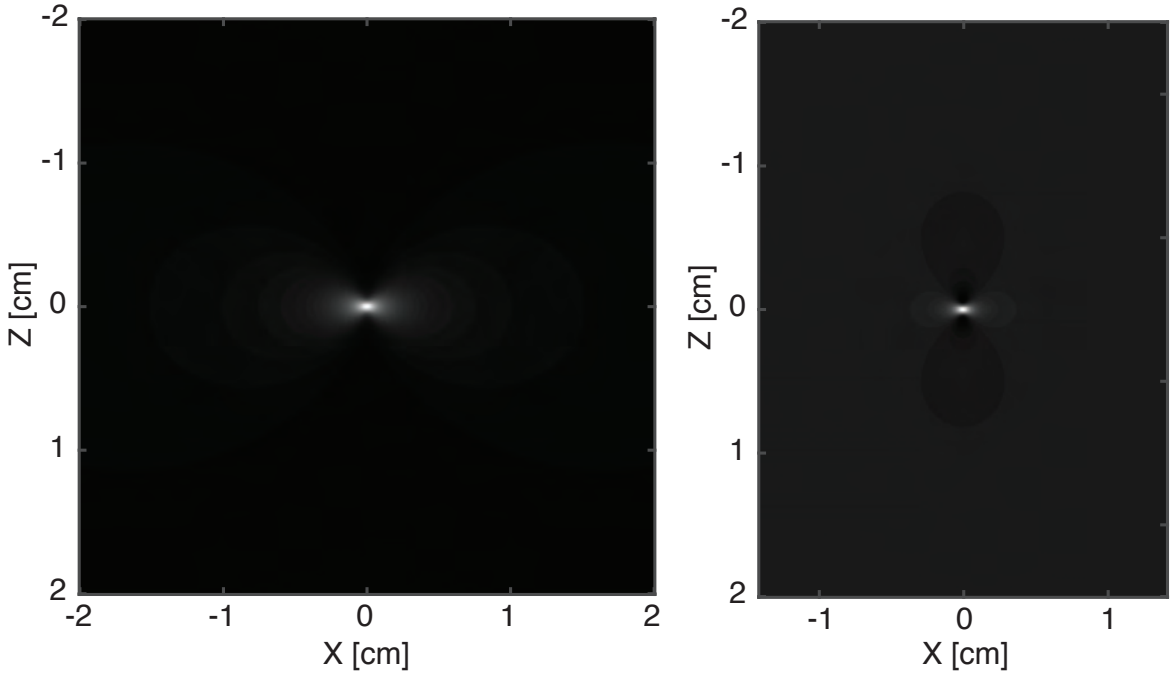

Figure 3.3: **PSF in xz-plane for LS-008 Particles.** *Left*: Theoretical projection PSF of our 6.3 T/m FFL system using SPIO tracer with core diameter of 25 nm. The FFL is along the y-direction, and is rastered in the x- and z-directions to create a projection as shown. *Right*: Projection reconstruction was performed on the projection PSF. The xz plane of the resulting 3D PSF is shown here.

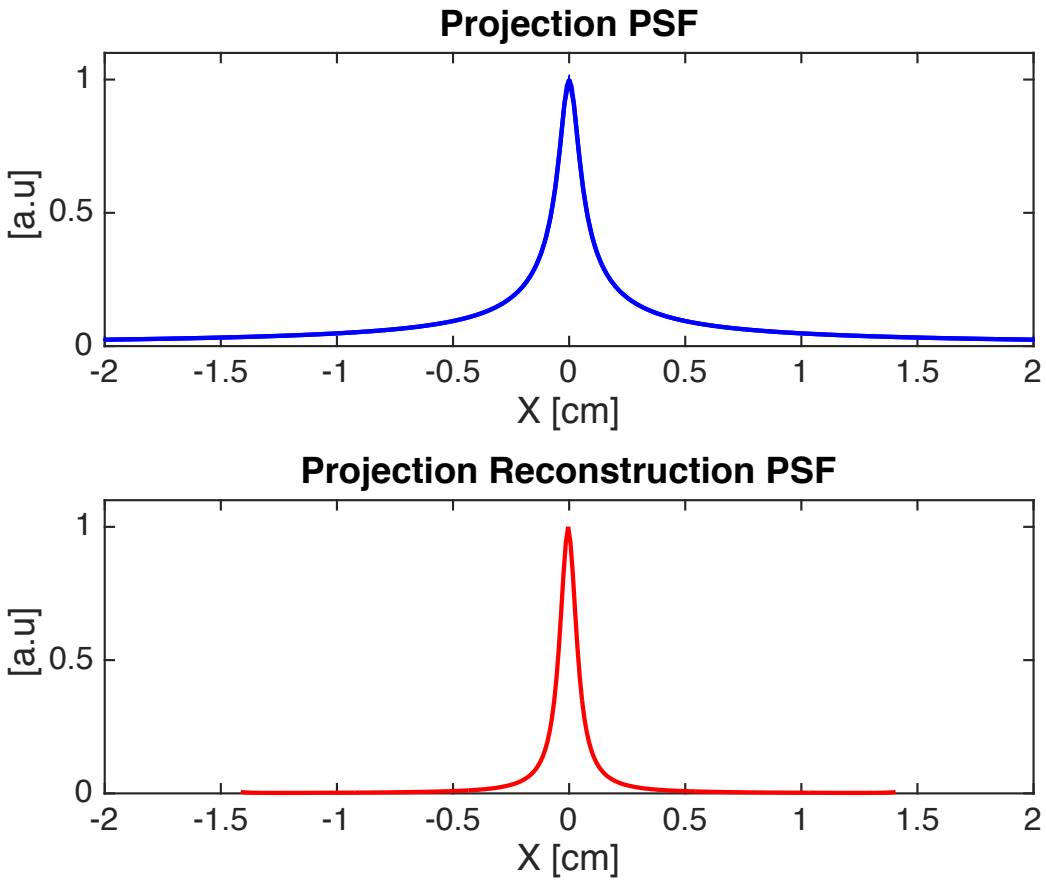

Figure 3.4: **PSF in x-axis for LS-008 Particles.** *Top*: Normalized profile of the 2D projection PSF along the x-axis. *Bottom*: Normalized profile of the 3D projection reconstruction PSF along the x-axis. Note that there is a sharpening in the PSF due to projection reconstruction.

3.2 Simulation and Design

3.2.1 Permanent Magnet Assembly

All of our existing MPI imagers up to this point used permanent magnets to create the main gradient field, and shifted the field-free region in each dimension by adding a spatially homogeneous field using copper Helmholtz coils. We investigated the possibility of building a high gradient version in simulation.

We used the surface current model to simulate blocks of permanent magnets using MATLAB [88]. In this method, the magnet is reduced to a distribution of equivalent current. The current distribution is then input into magnetostatic field equations as a source term, and the field is obtained using standard methods for steady currents. We simulate the surface current density with the following equation:

$$j_m = M \times \hat{\mathbf{n}} \tag{3.4}$$

where j_m represents surface current density, M represents the magnetization vector of the permanent magnet, and $\hat{\mathbf{n}}$ represents the unit surface normal. For manufacturability, we decided to limit ourselves to rectangular blocks of neodynium magnets with residual flux density B_r of 1.25 T ($M = 9.95 \times 10^5$ A/m). Lengths of wires are distributed throughout the magnet surface to simulate the magnet, and the field is calculated for current carrying finite wire segment with the following equation:

$$B = \frac{\mu_0 I}{4\pi a}(cos\theta_1 + cos\theta_2) \tag{3.5}$$

where B is the magnetic field evaluated at a point of interest (P) in space, I represents the current in the wire, θ_1 and θ_2 represent the angles between the finite wire and the line between point P and either end of the finite wire, a represents the shortest distance between point P and the finite wire. The simulation setup is shown in Figure 3.5.

The size and position of each magnet were optimized to increase field gradient and create near zero field in the axis of the FFL (y-axis), while allowing a 5.125″ bore for murine imaging. The field profiles along the x-, y- and z-axes are shown in Figure 3.6(a). The field gradient along the x-, y-, and z-axes were simulated to be 8.455 T/m, 0.097 T/m, and 7.9 T/m, respectively. The FFL is electronically shifted for an imaging field of view (FOV) of 40 mm in the x-direction, and the simulation of the entire assembly is shown in Figure 3.6(b). The electromagnets were simulated to consist of 1/4″ square wire with a 1/8″ diameter extruded circular channel in the center for water cooling. The total weight of the NdFeB magnets was estimated to be 60.9 kg. Due to the size of the permanent magnet assembly, the Helmholtz coil pair was required to be large enough to create enough field to shift the FFL 20 mm away from the center. Each coil had 195 turns, with an estimated peak power consumption of 10.6 kW. The coils were estimated weigh 117.6 kg.

The design yielded desired field gradient specifications. Nevertheless, there were a few construction feasibility challenges. Although the magnets were designed to be rectangular,

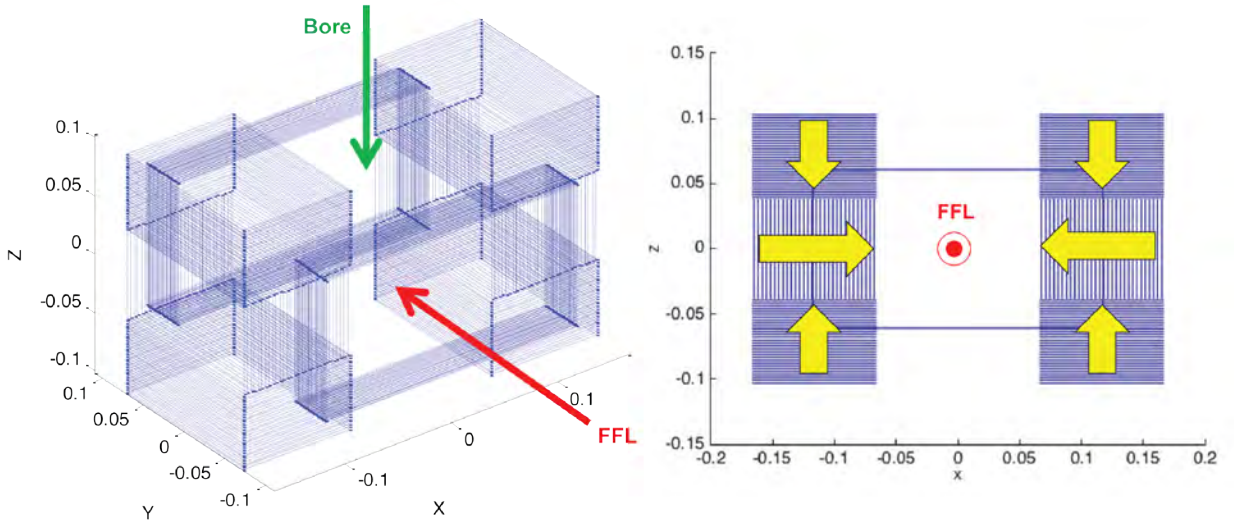

Figure 3.5: **Permanent Magnet FFL Layout.** Four pairs of permanent magnets opposing each other were used to create a high gradient FFL. The xz view of the assembly is shown on the right, with the FFL vertical to the page. Axes units in meters.

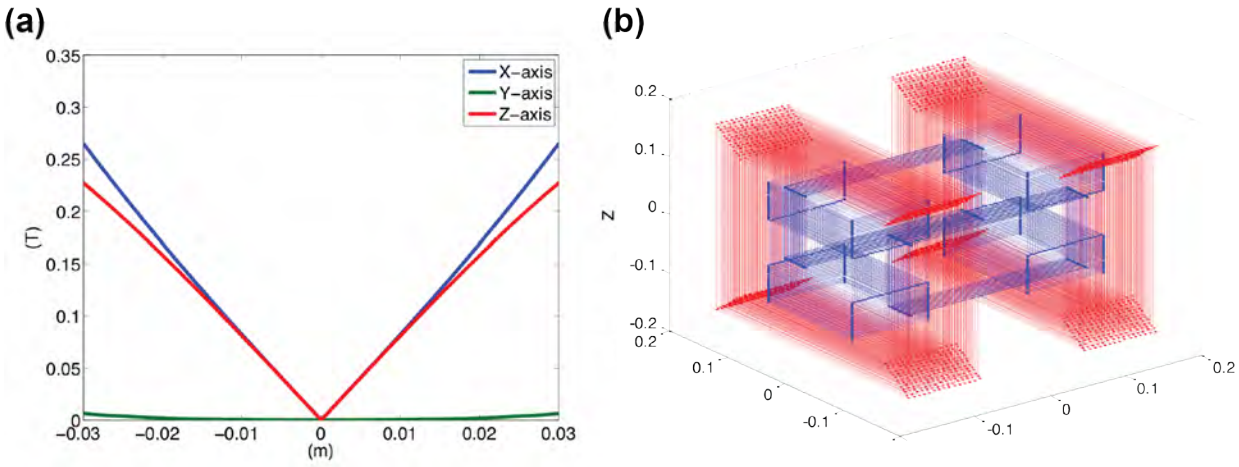

Figure 3.6: **Permanent Magnet FFL Field in Axes and Shift Coils.** (a) The field gradient along the x-, y-, and z-axes were simulated to be 8.455, 0.0965, and 7.9 T/m, respectively. (b) Permanent magnet FFL with slow shift Helmholtz coil pair.

size customization at that scale would have been costly. The main concern, however, was the strong opposing force between the permanent magnet pairs. We have constructed imagers with one opposing pair of magnets at similar distances from each other. However, the design with four opposing pairs of magnets that are within close proximity of each other will

significantly increase the difficulty of assembly due to high force and torque. Not only will the assembly process be challenging, the fixture for all the parts will also need to be extensively modeled to ensure stability and safety. To manufacture a strong enough fixture that is non-magnetic or close to non-magnetic will also be challenging. Due to these challenges, along with the concern of high power consumption for electronically shifting the FFL, we decided to test an alternative design using electromagnets with iron return.

3.2.2 Electromagnet with Iron Return

Motivation

Akin to electrical circuits where the current finds the path with the least resistance to travel, magnetic fields also find the path with least reluctance. It is very common to use an iron return to reduce total reluctance of an air-gap magnetic circuit, with two to four-fold power reduction. As shown in Figure 3.7, the same electromagnet pair with and without iron return was simulated. The resulting field maps and axis field profiles are shown. A 3× boost in field gradient is achieved when the iron returns are present. This magnet serves to create the gradient and simultaneously shift the FFL in the x-direction by altering the currents each of two coils. The shifting trajectory will be discussed in further detail.

Simulation Tool: ESRF Radia

The linear current carrying coils and permanent magnets that we have been using thus far in our systems were easy to simulate as described in the previous section. The iron return material, on the other hand, is nonlinear. We used an open source software package developed by the European Synchrotron Radiation Facility (ESRF) to simulate the iron return electromagnet. This is a 3D magnetostatics computer code optimized for accurate and fast computation of the magnetic field and the field integrals along a line. Radia uses boundary integral methods to solve for magnetic fields, a method that differs significantly from Finite Element Methods (FEM). Volume objects are created, and material properties are subsequently applied to these objects. Each object can be subdivided into a number of smaller objects. A large interaction matrix is created in memory which represents mutual interactions between the objects. The final magnetization in each small object is obtained iteratively by a sequence of multiplications of the interaction matrix by the instant magnetization vector, taking into account the material properties [89]. The Radia software package is used as an integrated module of Wolfram Mathematica.

Design Specifications

We designed our iron core by iteratively simulating geometries to satisfy the following constraints and goals:

- Through access for imaging bore (5.125″ diameter)

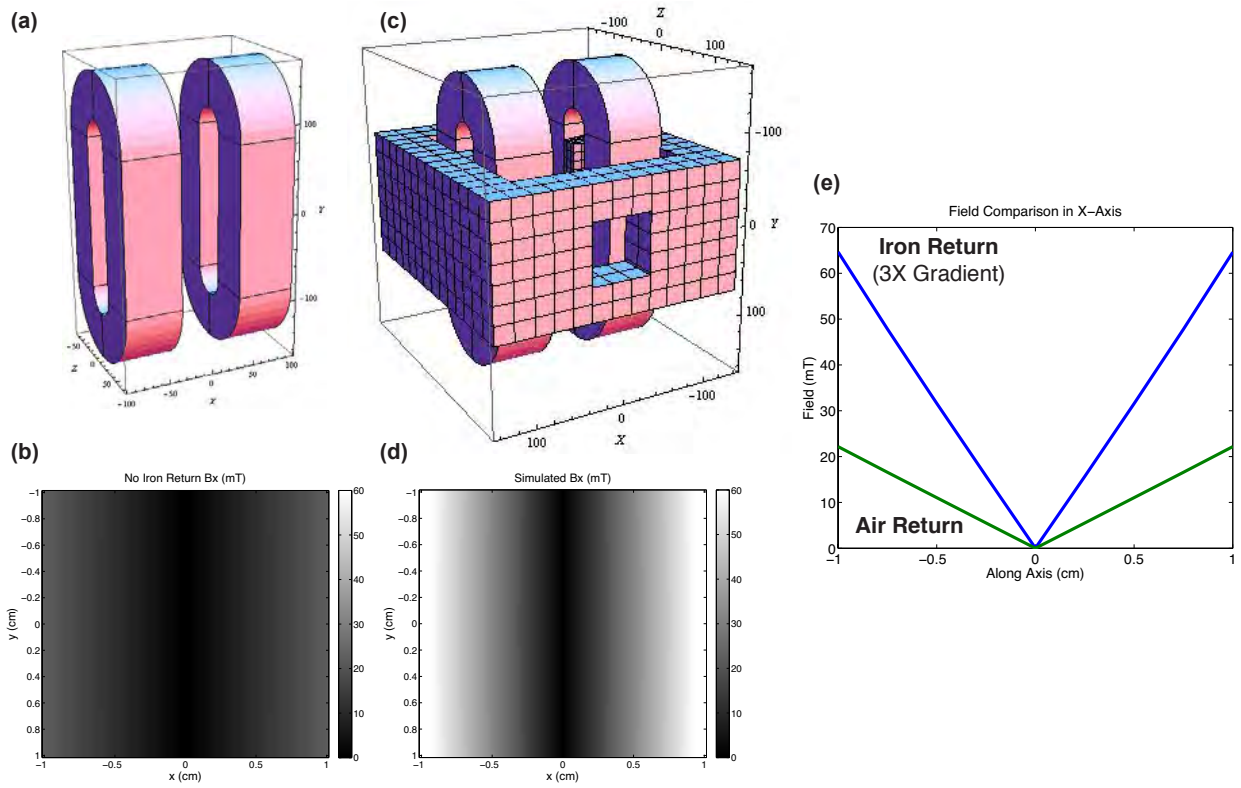

Figure 3.7: **Electromagnet Field Boost due to Iron Return.** Simulated geometry (a) without iron return and (c) with iron return. Resulting field map in the xy-plane in mT (b) without iron return and (d) with iron return. (e) Magnetic field profile along x-axis in mT. Three fold gradient boost is apparent when the iron return is present.

- Maximize field gradient in x- and z-directions (> 6 T/m)
- Minimize field gradient in y-direction for FFL (≤ 0.1 T/m)
- Minimize size of coils and power consumption
- Minimize iron return weight

Here, we will first introduce the coordinate system with respect to the iso-center of our magnet for ease of describing the design. The y-axis of the magnet is parallel to the FFL, and coincides with the FFL when baseline gradient is applied. In order to make projections through the imaged specimen, a through access imaging bore is required to load the imaging specimen. The axis of this imaging bore is defined as the z-axis of the magnet. The x-axis is defined as the direction in which the FFL is being shifted.

The geometry of the electromagnet with iron return was inspired by quadrupole magnets used for accelerator physics [90]. The primary difference between quadrupole accelerator

magnets and MPI magnets is the through access imaging bore required for MPI. The FFL in MPI needs to be perpendicular to the sample for projections to be taken through the sample. This requirement results in a magnet geometry that is vastly different from accelerator quadrupole magnets. A second difference is that an additional homogeneous field is required to shift the position of the FFL in the x-direction. During shifting, the FFL needs to be sufficiently homogeneous to ensure that there is not signal fading or loss of resolution at the edges of the field of view in the x-direction. The shape of the pole had to be adjusted to ensure that a long FFL along the y-direction could be generated and shifted while minimizing the weight of the iron and size of the coils.

In order to minimize the power and weight of the iron return, we employed stepped poles. Instead of using a flat pole piece where the thickness of the pole piece in x remains the same along y, we varied the x thickness of the pole piece. The pole pieces were stepped closer to iso-center in the x on either side of the imaging bore in y. This allowed for the imaging bore to not be breached, while minimizing the total length of the magnet and the pole piece in the y-direction. If a uniform pole were used instead of the stepped pole, the magnet and iron core would need to be much longer in the y-direction to match the same level of homogeneity in the FFL.

To boost the gradient strength, the pole pieces were tapered in the z-direction, whereby the z thickness of the pole tip is smaller than that of the base of the pole. Tapering the pole piece allows the flux to be more optimally channeled through the imaging region, thereby increasing the field efficiency. The tapered pole piece also ensures a more uniform magnetic flux density over the pole area to to prevent saturation at high fields. By removing sharp corners in the pole pieces, we can prevent the flux lines from piling up in the corner and saturate. These features ensure that the field remains linear over a wider range of excitations [91].

To reduce hysteresis loss, the iron return was made of soft iron. Low carbon cold-rolled steel was selected for low cost, as it is frequently used in motor and transformer iron cores. Using the properties of low carbon steel, the following parameters were iterated in simulation to achieved the desired constraints and specifications:

- **Top/Bottom pole**: base width in z, tip width in z, height in y and depth in x
- **Center pole**: base width in z, tip width in z, height in y, depth in x
- **Coils**: total width in z, total height in y, thickness in x, cross section width in z and racetrack curvature in x and z
- **Entire Iron Return**: base width in z, base depth in x and gap width between halves in x

Iron Return Signal Interference

Our system consists of 4 major components: gradient and shift electromagnets, iron return, transmit coil, and receive coil. The electromagnets with the iron return create and

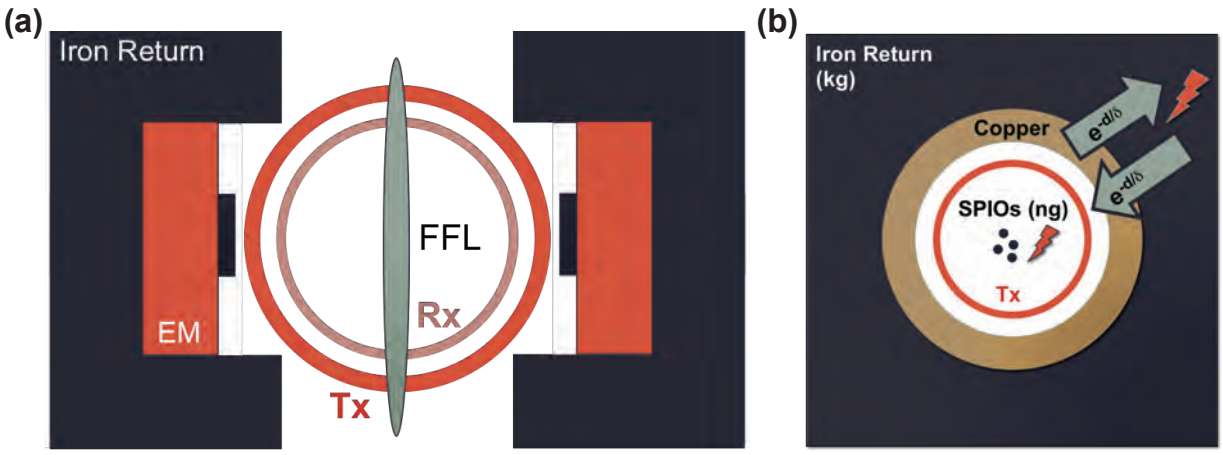

Figure 3.8: **Iron Return System Illustration.** (a) Simplified top view schematic of system consisting of iron return, pair of electromagnets (EM), generated FFL, transmit (Tx) coil, and receive (Rx) coils. (b) Diagram of signal from SPIOs and iron return and effect of copper shielding.

shift the FFL. The transmit coil is a solenoid that creates a 40 mT peak-to-peak (mTpp) sinusoidal waveform at 20.225 kHz and the receive coil picks up the corresponding nonlinear response of the nanoparticles. A simplified schematic of these components is shown in Figure 3.8(a).

MPI detects signal from iron, and the relevant amount of SPIOs we are detecting in our phantoms or animal is in the nanogram to microgram range. Our iron returns, on the other hand, also consists of iron, but weighing hundreds of kilograms. The implication here is that the signal from the iron return could be significantly larger than that from the particles. The normalized magnetization vs. applied field curves for our SPIOs (25 nm core size) and the low carbon cold-rolled steel iron return are shown in Figure 3.9. The black circles indicate the baseline field that the iron is experiencing and its corresponding normalized magnetization. This also corresponds to the center of the 40 mTpp sinusoidal excitation. The SPIOs at the Field Free Region (FFR) are not experiencing any baseline field. Therefore, when the 40 mTpp sinusoidal excitation is applied, the corresponding magnetization, as shown in Figure 3.9(b), is not sinusoidal. This nonlinear response results in harmonics and ultimately the detection of the SPIOs. The iron return, on the other hand, is being excited in a fairly linear regime near saturation due to the effect of the gradient and shift coils. The response to sinusoidal excitation is therefore nearly sinusoidal, as shown in Figure 3.9(d). This results in minimal harmonics in the signal, allowing us to separate out particle signal from that of the iron return.

A copper bore is used for shielding to further combat this potential problem. The copper bore attenuates the transmit signal that excites the iron return as well as the corresponding signal from the iron return. This is illustrated in Figure 3.8(b). Faraday's Law of induction

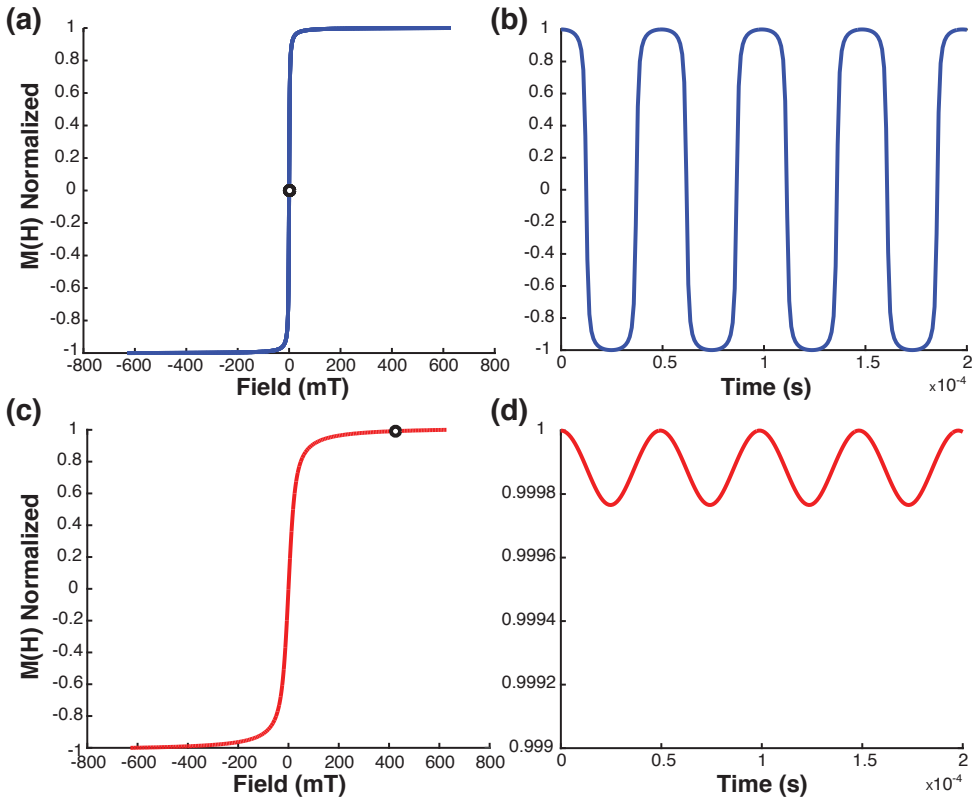

Figure 3.9: **SPIO vs. Iron Return: Langevin Curve and Signal.** (a) Normalized M-H curve of 25 nm core size SPIOs. (b) Normalized signal from SPIOs in response to 40 mTpp applied excitation field from the transmit coil. (c) Normalized M-H curve of the cold-rolled steel iron return. (d) Normalized signal from the iron return in response to 40 mTpp applied excitation field from the transmit coil. Black circles in (a) and (c) indicate center of sinusoidal applied field.

states that a time-varying magnetic field induces closed loop electrical current in conductors in planes perpendicular to the magnetic field. This current is called eddy current. Lenz's law states that an eddy current will create a magnetic field that opposes the change in the magnetic field that created it. Hence, eddy currents counteract the original alternating magnetic field, as illustrated in Figure 3.10(a). This results in a time-varying magnetic field near a conductor decreasing exponentially from its value at the surface of the conductor (B_s), as described by the following equation:

$$B = B_s e^{-d/\delta} \tag{3.6}$$

where δ is the material specific skin depth in meters, and d is distance from the surface of the conductor, also in meters. The skin depth is given by:

$$\delta = \frac{1}{\sqrt{\pi f \mu \sigma}} \tag{3.7}$$

where σ is the conductivity of the conductor, f is the frequency of the magnetic field, and μ is the absolute magnetic permeability of the material. In our case, we are using copper as our shield, which has conductivity of $\sigma = 5.96 \times 10^7$ S/m and relative permeability of $\mu = 1.256629 \times 10^{-6}$ H/m. As mentioned previously, signal attenuation is a function of frequency. The copper tube used in our system has a wall thickness of 2.77 mm, for which the field attenuation as a function of frequency is shown in Figure 3.10(b). Since the iron return is also further from the receive coil, the resulting signal is further attenuated. A conservative estimate where the iron return is 70 mm away from the center of the bore yields field attenuation of -130 dB.

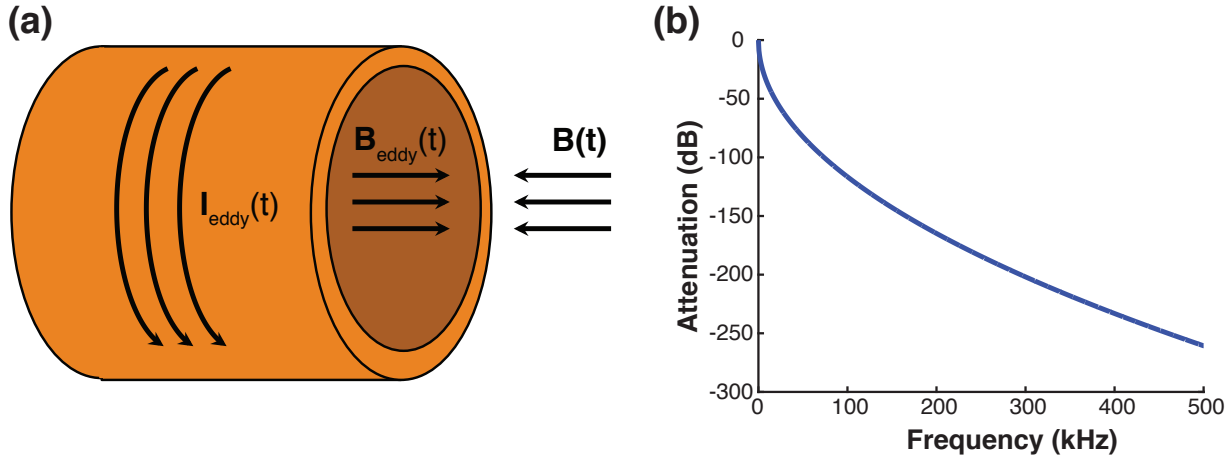

Figure 3.10: **Skin Effect Copper Shielding.** (a) Eddy currents counteracting the original alternating magnetic field due to skin effect. (b) Magnetic field attenuation in dB as a function of frequency with our copper bore with wall thickness of 2.77 mm.

Iron Return Eddy Current Loss

SPIOs are excited with the transmit system at 20.225 kHz and particle signal is picked up by the receive system. This signal is spatially localized by the selection field gradient. To create an image, the selection field gradient is shifted in the x-direction, and the specimen is mechanically translated in the z-direction. The maximum frequency to shift the FFL in our system is estimated to be 10 Hz. Similar to the copper shield, since the iron return is also conductive, the slow shift at 10 Hz causes eddy currents in the iron return, which in turn attenuates the selection field gradient. However, unlike the copper shield which is designed to attenuate the transmit and receive signal from the iron return, we would like to minimize losses in the selection field gradient from the iron return. Eddy currents in the iron return

will require significantly higher power to achieve the same gradient strength. In addition, this will result in heat loss in the iron return. Eddy current losses cannot be eliminated completely, but can be greatly reduced by minimizing the length of the conductive path, as illustrated in Figure 3.11. Instead of having one big solid iron core, the iron return is split up into many thin pressed steel plates called laminations. These laminations are coated by electrically insulating varnish to ensure high effective resistivity in the core. The laminations in our system had C-5 electrical steel insulating coating.

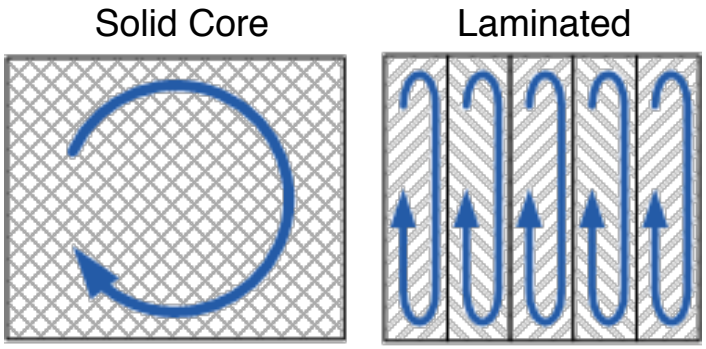

Figure 3.11: **Iron Core Laminations.** Electrically insulated laminations are used to increase the resistivity and in turn reduce the eddy current strength in the iron core. This ensures that the selection field gradient is not attenuated by eddy currents.

The low carbon cold-rolled steel used for our iron return has a relative permeability μ_r of $\sim$200 [92] and a conductivity of $2.17 \times 10^6\ \Omega^{-1}m^{-1}$. The skin depth ($\delta$) at 10 Hz is calculated to be 7.64 mm (Equation 3.7). We used 16 gauge laminations in our system, which are 1.52 mm thick. The field attenuation is characterized by the following equation [93]:

$$a(\Delta) = \frac{\sqrt{2}}{\Delta}\sqrt{\frac{\tan^2(\Delta/2) + \tanh^2(\Delta/2)}{1 + \tan^2(\Delta/2) + \tanh^2(\Delta/2)}} \tag{3.8}$$

where Δ is the ratio of lamination thickness and skin depth ($\Delta = d/\delta$). This yields an attenuation factor of 0.9903, meaning less than 1% of the field is attenuated due to eddy current losses.

3.3 Prototype Construction and Characterization

Both the FFP and the FFL in our lab had main field gradients created by permanent magnets. These were easily simulated with the linear surface current model [88], as mentioned in the previous section. Iron-core magnets, on the other hand, are more difficult to simulate due to the nonlinear nature of the iron material interactions. Other potential issues we identified include eddy currents, hysteresis, saturation of the iron core, and signal

interference from the iron core material. With these potential issues, it became clear that the construction and characterization of a prototype is necessary.

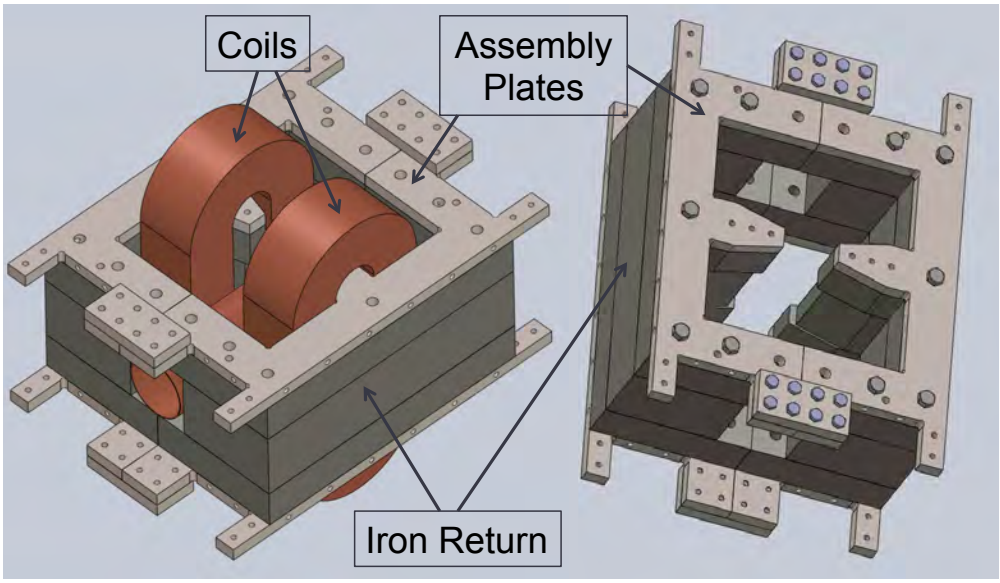

Figure 3.12: **1/8th Size Prototype Mechanical Design.** Our prototype consisted of low carbon cold-rolled steel 16 gauge laminations, custom-made assembly plates, and hand-wound coils, and a copper bore. This was built to validate our magnetic field simulations of our first iron-dominated electromagnet design.

After the design was finalized through simulations, a $1/8^{th}$ scale model of the magnet was constructed. The laminated iron core consisted of laser-cut 16 gauge low carbon cold-rolled steel sheets that were individually coated (C-5 electrically insulating coating). The thickness was chosen to minimize eddy current loss (5 skin depths at slow shift frequency of 10 Hz). The individually coated laminations were bonded with epoxy to make a pair of lamination assemblies (Polaris Laser Laminations, LLC, West Chicago, IL, USA). Stainless steel plates ($0.5''$ thick, 18-8 stainless steel) were manufactured (Brightlight Welding & Manufacturing, Santa Clara, CA, USA) for assembly and structural support. Stainless steel, $3/8''$-16, $7''$ long bolts (McMaster-Carr, Elmhurst, IL, USA) were electrically insulated with heat shrink (R.K.B. Industrial, Inc., Ogden, UT, USA) and used in conjunction with fiberglass washers as well as locknuts (Seastrom Manufacturing Co., Inc., Twin Falls, ID, USA) to hold the laminations and structural plates together. The Solidworks model of the mechanical design is shown in Figure 3.12.

Two 1000-turn racetrack coils were hand-wound with 14 gauge magnet wire (Rea Magnet Wire, Fort Wayne, IN, USA) and mechanically affixed with flame retardant thermally conductive epoxy resin (Epoxies, Etc., Cranston, RI) during winding. Photos of the winding rig and winding process are shown in Figure 3.13. A winding rig was assembled with a hardened precision steel shaft, stamped-steel mounted ball bearings, an aluminum hand wheel,

galvanized steel brackets and wooden frame, as shown in Figure 3.13(b). Square-flanged aluminum clamp-on framing fittings, 3D printed components, steel threaded rods and nuts, (Figure 3.13(a)) along with laser cut acrylic sheets were assembled as a winding former to couple to the rig, as shown in Figure 3.13(c). The finalized coils were covered with kapton tape and mechanically coupled to the stainless steel plates on the iron return by 3D printed brackets and threaded steel rods and nuts, as shown in Figure 3.13(a). All 3D printing was done with a powder bed and ink jet printer (ZPrinter 150, 3D Systems, Rock Hill, SC, USA) and post-processed with epoxy binding. All off-the-shelf components were purchased from McMaster-Carr. The final assembled prototype is shown in Figure 3.14.

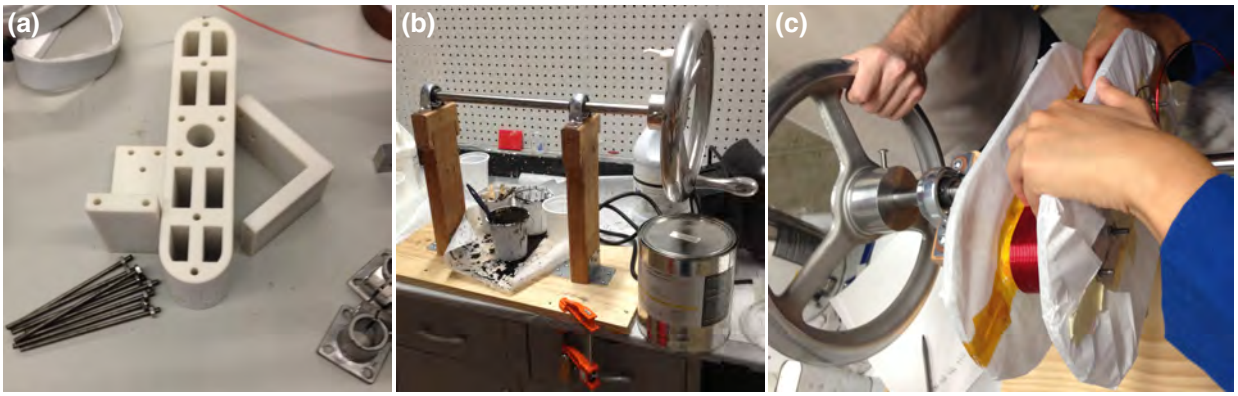

Figure 3.13: **1/8th Size Prototype Winding.** (a) Components for coil winding former and final mechanical assembly. (b) Assembled coil winding rig. (c) Coil winding process using winding assembly.

For system characterization, a linear amplifier (AE Techron LVC 5050, Elkhard, IN) was used to control the current in the coils. To measure static magnetic field maps, the two coils were connected in series, and a DC current density of 4.65 A/mm^2 was used (power limited). A hall effect gaussmeter (Lake Shore DSP 475, Westerfield, OH) was used with transverse and axial probes for magnetic field characterization. Three linear motor stages and a rotation stage (Velmex, Blookfield, NY) were used for accurate positioning of the gaussmeter probe. MATLAB (Mathworks, Natick, MA) was used in conjunction with a DAQ module (National Instruments USB-6259 Austin, TX) to control and monitor all components of the characterization system. Preliminary magnetic field maps were measured with this device. A photo of the characterization setup is shown in Figure 3.15

Measurements of the magnetic field map are shown in Figure 3.16. As seen in Figure 3.17, we found excellent correspondence between the simulated and measured axis field profiles. We have also been able to shift the FFL through the field of view for imaging by altering the currents in the two coils, as predicted in our simulations. For this test, the coils were connected individually to two separate channels of the AE Techron LVC 5050 amplifier, and the currents were offset in the opposite direction from baseline gradient level to shift the FFL. The shift waveforms will be described in more detail in the full scale scanner section.

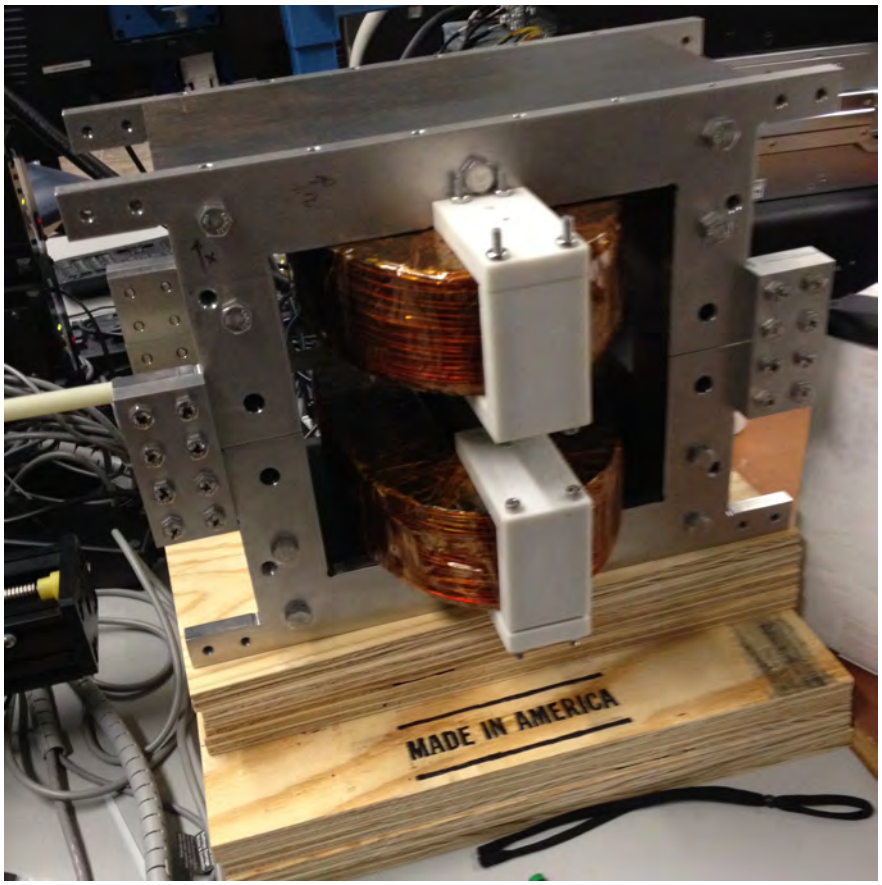

Figure 3.14: **Photo of Assembled 1/8th Size Prototype.** The measured field from this prototype closely matched the simulated field.

Measurements indicated consistent homogeneity of the FFL with negligible eddy currents or hysteresis effects.

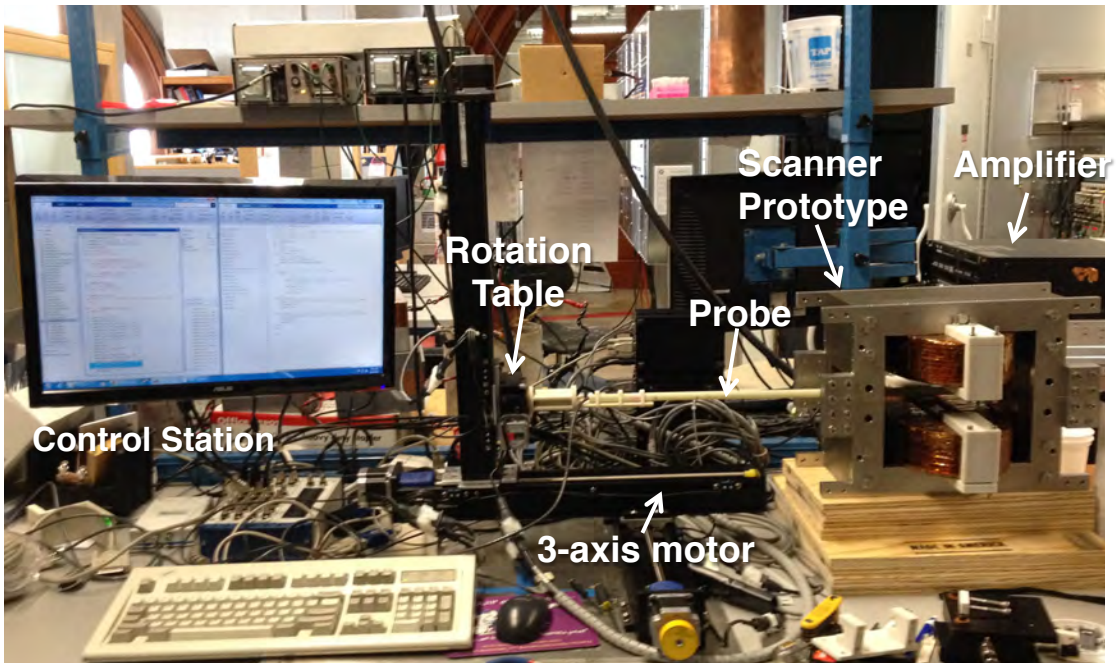

Figure 3.15: **1/8th Size Prototype Characterization System.** A linear amplifier was used to supply current to the gradient and slow shift coils. A gaussmeter was used with axial and transverse probes to measure magnetic field maps. Three linear motor stages and a rotational stage were used for accurate positioning of the gaussmeter probe. All components were controlled by MATLAB through a DAQ module.

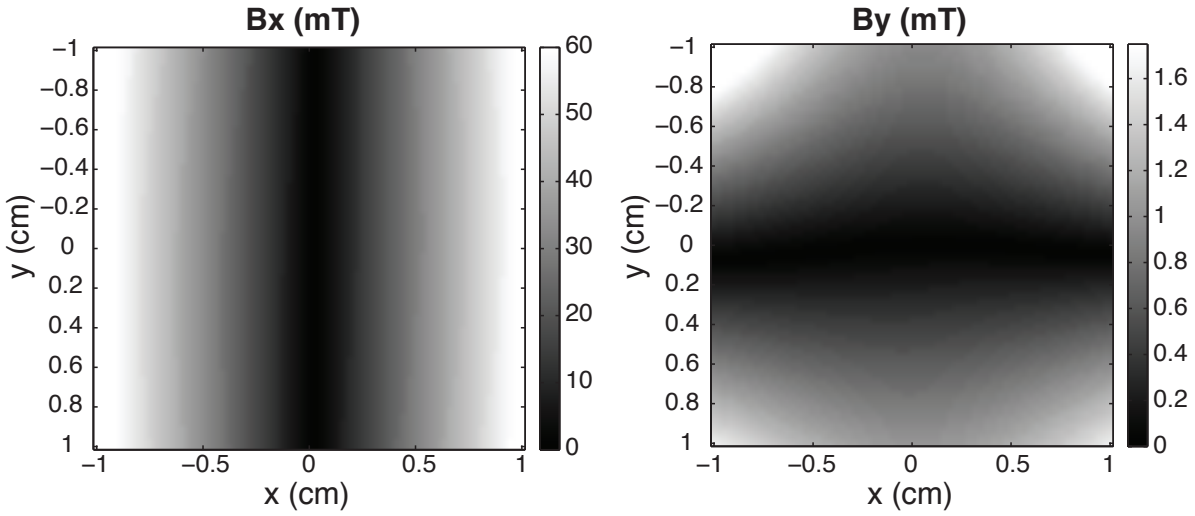

Figure 3.16: **1/8th Size Prototype Field Maps.** *Left:* Interpolation of measured field in x-direction in 20 mm $\times$ 20 mm xy plane at iso-center of scale model. *Right:* Interpolation of measured field in y-direction in 20 mm $\times$ 20 mm xy plane at iso-center of scale model. From this scale model, we generated a 6.3 T/m gradient in x-direction and 0.1 T/m gradient in the FFL.

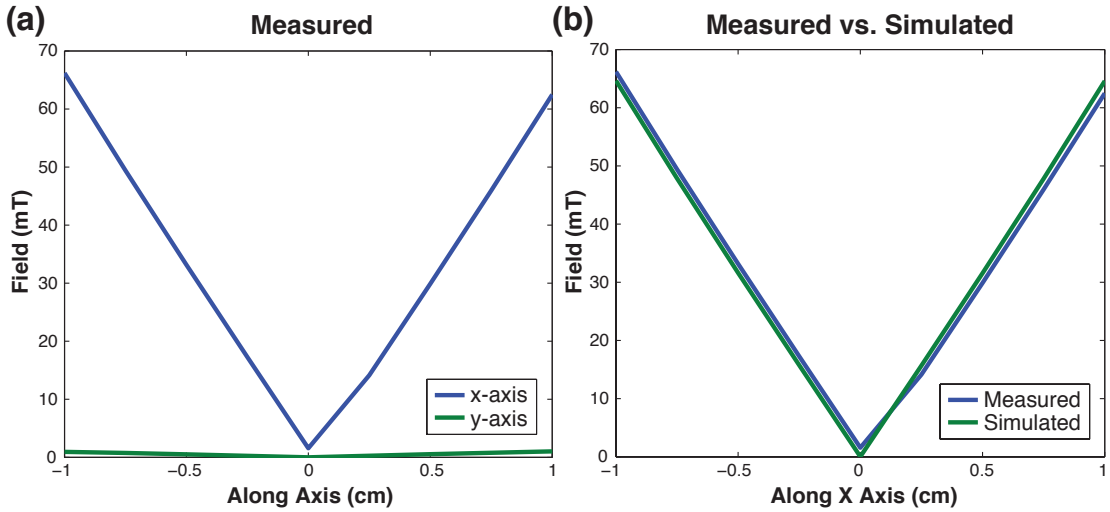

Figure 3.17: **1/8th Size Prototype Field in Axes.** (a) Measured field along x-axis and y-axis. This prototype system generated a 6.3 T/m gradient in x-direction and 0.1 T/m gradient in the y-direction. (b) The measured and simulated field in axis had excellent agreement.

3.4 Full Scale Scanner Design

After magnetic field simulations were validated from experimental measurements with the prototype, we proceeded to design and construct the full scale preclinical imaging system. The scanner consists of the following major components: (1) Laminated iron return, (2) Gradient and slow shift coils, (3) Copper bore shielding, (4) Transmit and Receive systems, (5) Water cooling system, (6) Specimen Mechanical Motion System, (7) Respiratory gating system. All these components will be discussed in detail in the following sections. An illustration of the iron return electromagnet assembly is shown in Figure 3.18.

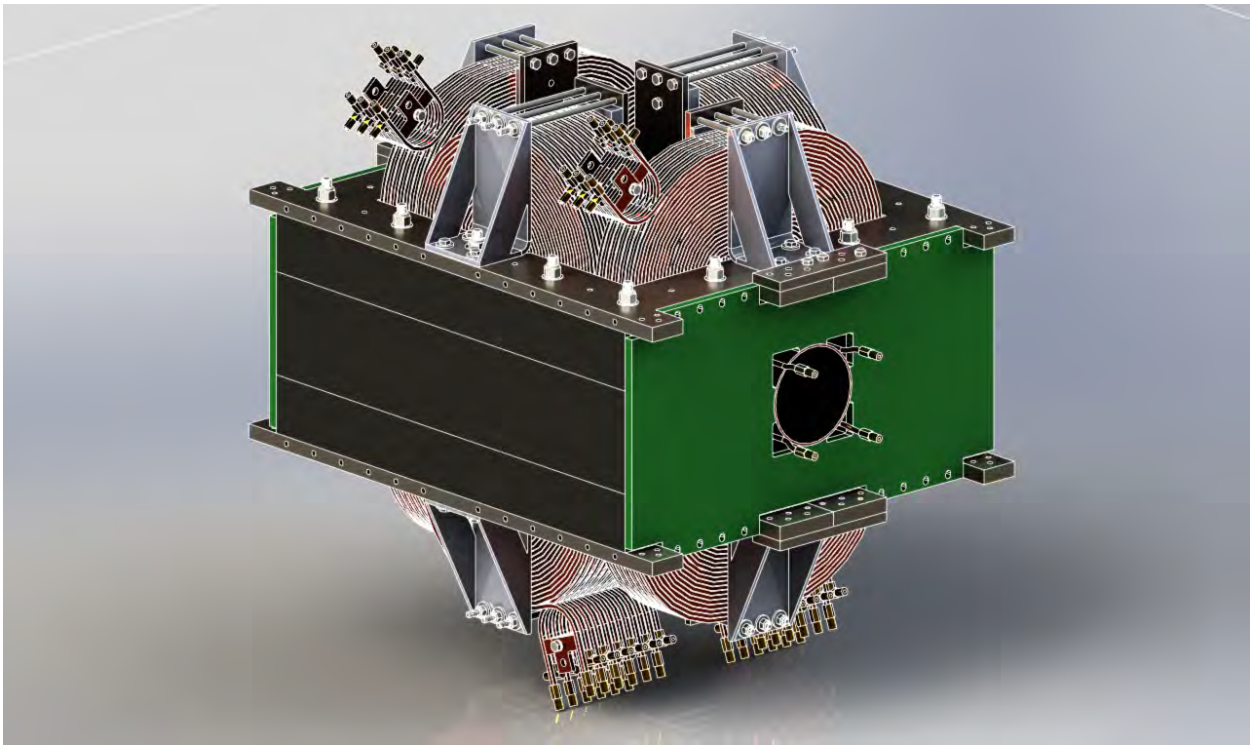

Figure 3.18: **High Resolution FFL Assembly Illustration.** The scanner consists of water-cooled electromagnets, laminated iron return, water-cooled copper bore, as well as transmit and receiver coils inside the copper bore.

3.4.1 Laminated Iron Return

The iron return was scaled up from our prototype with slight changes incorporated for mechanical assembly. The laminations thickness was the same as the prototype: 16 gauge cold-rolled steel sheets, C-5 Coated and epoxy bonded. The assembled iron core was painted with electrically insulating polyurethane varnish (John C. Dolph Co., Monmouth Junction,

NJ, USA) to prevent corrosion in the long term. Stainless steel plates (3/4″ thick, 18-8 stainless steel) were manufactured (Brightlight Welding & Manufacturing, Santa Clara, CA, USA) for assembly and structural support. Stainless steel, 1/2″-13, 14″ long bolts (McMaster-Carr, Elmhurst, IL, USA) were electrically insulated with heat shrink (R.K.B. Industrial, Inc., Ogden, UT, USA). These bolts were used in conjunction with stainless steel and fiberglass washers, as well as locknuts (Seastrom Manufacturing Co., Inc., Twin Falls, ID, USA) to hold the laminations and structural plates together. The stainless steel plates and fasteners were sent to Polaris Laser Laminations, LLC (West Chicago, IL, USA) along with assembly instructions. The resulting iron assemblies prior to shipping are shown in Figure 3.19.

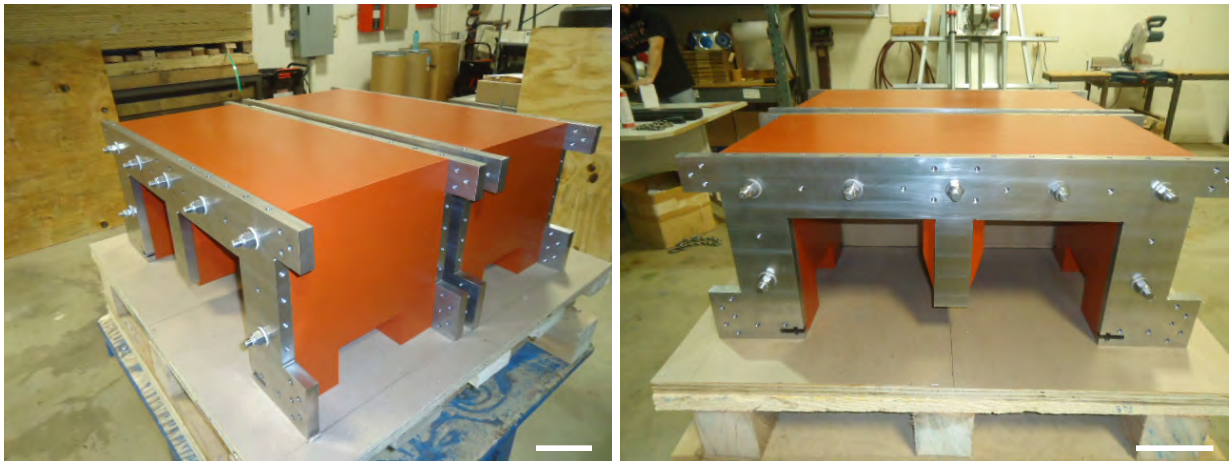

Figure 3.19: **Photo of Assembled Iron Return Laminations.** The iron return (in two halves) was assembled with C-5 coated, 16 gauge cold-rolled steel sheets. The epoxy-bonded laminations were then painted with a polyurethane varnish (orange) to prevent corrosion. Each half was then mechanically secured by custom stainless steel plates with electrically insulated bolts for structure support. Scale bars: 0.1 m.

3.4.2 Gradient and Slow Shift Coils

The gradient and slow shift coils were racetrack coils made of square wire (0.22″ × 0.22″ cross section) magnet wire with an extruded water channel (0.142″ diameter). The wire is coated with a thin layer of electrically insulating enamel (0.0025″) both on the inner surface of the extruded water channel and on the outer surface. The coils consist of 12 two-layer pancakes. These pancakes are electrically connected in series, but have individual water cooling circuits for optimal cooling efficiency. The stacks are held together by electronically insulated bolts that go through machined copper tabs connected to the wire. The copper tabs are insulated with custom kapton sheets at staggered positions to prevent shorts while

connecting the pancake coils in series electrically. Extensive testing was done for each pancake coil to ensure consistency in electrical and hydraulic properties. Custom Coils, Inc. (Benicia, CA, USA) sourced the extruded magnet wire, manufactured the coils, and tested them to ensure that they were made to our specifications.

3.4.3 Copper Bore Shielding

The copper bore was made with Schedule M 5″ copper pipe (OD = 5.125″, ID = 4.907″). The size of the bore was chosen to accommodate the transmit and receive coils necessary to image a small rat. Skin depth and shielding analysis was provided previously in Section 3.2. A custom designed copper ring with clearance holes was brazed to the copper tube to serve as a coupling flange to the main magnet. Four copper tubes (straight 0.25″) were soft soldered to the copper bore for cooling of the bore. These copper tubes were evenly spaced around the perimeter of the copper tube and bent at the ends to allow for 0.25″ hose fittings to be attached.

3.4.4 Transmit and Receive Systems

The analog signal chain consists of the transmit and receive systems. The transmit system excites the SPIOs with a pure sinusoidal waveform while the receive system inductively detects the particle signal simultaneously. The receive system is designed to reject the large transmit field to isolate the nanoparticle signal.

A transmit filter composed of a third order low-pass filter that is power matched to a resonant transmit coil. The transmit coil (27-turn, ID = 2.8″) was manufactured by Custom Coils, Inc. (Benicia, CA, USA). Square wire with an extruded water channel (0.27″ × 0.27″, d = 0.125″) was used. A litz wire receive coil of 45 mm diameter with (-1, 2, -1) gradiometer configuration was wound on a 3D printed former. Custom MATLAB Biot-Savart simulation software was created to simulate coil sensitivity, cancellation, and field homogeneity. This gradiometer was design to be tunable, and ultimately achieved 30 dB attenuation of direct feedthrough signal. A 90 dB passive notch filter at 20.225 kHz is used to further attenuate the direct feed through signal from the drive field. Commercial low noise preamplifiers were used for signal amplification and filtering for this experiments (SR560, Stanford Research Systems, Sunnyvale, CA). Commercial data acquisition units were used for signal generation and collection (National Instruments, Santa Rosa, CA, USA). More details of the transmit and receive signal chains can be found in [16].

3.4.5 Coil Cooling System

The transmit coil is cooled by a ThermoCube 600 system (Solid State Cooling Systems, Wappingers Falls, NY, USA). The ThermoCube system pumps fluorinert to the transmit coil which recirculated back to the cooling manifold of the unit. Cooling water is supplied to the ThermoCube from building tap supply to cool the recirculating processed fluorinert.

The gradient and slow shift coils are water-cooled using a NESLAB Coolflow System II Liquid to Liquid Heat Exchanger. The liquid exchanger pumps processed water (clean tap water) at 60 psi to a manifold. This manifold supplies the processed water to 24 parallel water circuits (12 two layer pancakes in each coil) as well as the cooling pipes attached to the copper bore. The water from all channels is recirculated back to the heat exchanger reservoir through a separate manifold system. Cooling water is supplied to the heat exchanger from building tap supply to cool the recirculating processed water. Each 2-layer pancake coil has flare to pipe fittings machined and brazed onto the hollow conductor ends. Female Flare to Push-to-connect adapters are connected to each fitting on the coil, while NPT push-to-connect fittings are attached to the plastic manifolds. We used $1/4''$ plastic tubing to connect the inlet and outlet manifolds to the coils.

We determined the number of water circuits in our coils by calculating the expected change in temperature based on the available pressure as well as the power deposited to create and shift the gradient. The power requirements for our coils are reported in Table 3.4. This is assuming the baseline power required to create a gradient of of 6.3 T/m. Note that this is a liberal estimate in terms of power usage, as the actual pulse sequence is not continuous. Due to motor movement and respiratory gating, the duty cycle is at most 70%.

Property	Unit	Value
Wire Length	[m]	611.73
Current Density	[A/mm^2]	4.6289
Current	[A]	156.21
Resistance	[Ω]	0.54
Power	[kW]	13.215

Table 3.2: Gradient and Slow Shift Coil Power Requirement at 6.3 T/m

The following assumptions are made for cooling calculations:

- Heat transfer through the thin fluid film separating the conductor surface and the bulk fluid flow is high at high Reynolds number (turbulent flow)
- The temperature at the inner surface of the conductor cooling channel is nearly the same as the coolant temperature
- The entire conductor cross section temperature is approximately equal to the cooling channel surface temperature due to the high thermal conductivity of the conductor

These assumptions allow us to estimate the maximum coil temperature by computing the maximum exit temperature of the coolant flow alone. Fixed parameters used for cooling calculations are listed in Table 3.3.

Note the listed kinematic viscosity is that of water at 60 °F. Instead of taking into account variations of the kinematic viscosity along the flow passage due to change in temperature, a

Property	Unit	Value
Mass Water Density (δ)	[kg/m^3]	1×10^3
Water Heat Capacity (c$_p$)	[kW–sec/kg–°C]	4.19
Kinematic Viscosity (ν)	[m^2/sec]	1.13×10^{-6}
Roughness (ε)	[m]	1.5×10^{-6}

Table 3.3: Fixed Cooling Parameters

simpler and more conservative approach is chosen by assuming that the kinematic viscosity is constant and equal to the maximum value expected over the cooling water temperature range at 60 °F. The roughness parameter is an estimation of the surface roughness of the cooling channel. The friction factor (f) is calculated using the following equation:

$$\frac{1}{\sqrt{f}} = -2log_{10}(\frac{\varepsilon}{3.7d} + \frac{2.51}{\frac{d}{\nu}\sqrt{\frac{2\Delta p}{\delta}\frac{d}{l}}}) \tag{3.9}$$

where d [m] is the diameter of the cooling channel, l [m] is the length of the hollow conductor, Δp [Pa] is the pressure drop available, ε [m] is the surface roughness of the copper cooling channel, and ν [m] is the kinematic viscosity of water at 60 °F, as described previously. The flow velocity, v [m/s], is then calculated using the following equation:

$$v = \sqrt{\frac{2\Delta p}{\delta f}\frac{d}{l}} \tag{3.10}$$

The flow velocity is used to calculated the volume flow rate (q [m^3/sec]):

$$q = \frac{\pi d^2}{4} \tag{3.11}$$

The change in coil temperature (ΔT [°C]) is then calculated using the following equation:

$$\Delta T = \frac{P}{\delta c_p q} \tag{3.12}$$

As a rule of thumb, an acceptable coil temperature rise which protects coil epoxy encapsulation from damage is 30 °C [91]. Assuming Δp of 60 psi and each coil is separated into 12 parallel water circuits, our liberal estimate of ΔT is 21.5 °C, which is safely below the recommended limit.

3.4.6 Specimen Mechanical Motion Systems

For projection MPI, the specimen is translated in the vertical direction over the desired field of view. For the purposes of 3D projection reconstruction imaging, the specimen is

rotated and projections are taken at various angles. The scanner was designed to be mounted on a Heavy Duty Composite-Wood-Top Table (McMaster-Carr, Elmhurst, IL, USA) with 4000 lbs capacity. The table top was machined for access of the motor and the imaging bore and reinforced with 1/4″ thick stainless steel angles (Discount Steel, Inc., Minneapolis, MI, USA). We machined 1/8″ thick stainless steel angles to secure the magnet to the steel angle that is fixed to the table.

A linear motor stage with 30″ travel (BiSlide, Velmex, Inc., Bloomfield, NY, USA) was purchased and mounted to the frame of the heavy duty table using custom-machined aluminum support plates (Brightlight Welding & Manufacturing, Santa Clara, CA, USA). A 1.5″ diameter mounting post along with a post mounting clamp and plate (Thorlabs, Inc., Newton, NJ, USA) were mounted onto the carriage of the BiSlide. A motorized rotating table (B48 Series, Velmex, Inc., Bloomfield, NY, USA) was attached to the post mounting plate. A garolite rod (30″ long and 1.25″ in diameter) was machined and mounted to the rotary table with a 3D printed base. Stainless steel shim stock was used to ensure that the rod is rotating on center in the imaging bore for optimal projection reconstruction image quality. A 3D printed coupler was pressure fitted onto the other end of the garolite with a rectangular couple to ensure stable and easy specimen mounting. Imaging specimens are loaded from the top of the magnet, and subsequently moved into the center of the magnet by the motor. Stepper motors were coupled to the linear and rotation stages. Each motor is controlled by an AE Techron LVC 5050 with a custom step/direction input and filters to minimize signal interference from motor movement. Animal beds were custom designed with nose cones and bite bars for vertical imaging of mice and rats.

3.4.7 Imaging Pulse Sequence & Respiratory Gating System

As previously described, a homogeneous sinusoidal drive field is applied to excite the SPIOs, and the nonlinear response is inductively detected by the receive coil. In order to localize this signal, a FFL is created, whereby only particles within the field free line will respond to the drive field. To make an image, this FFL is shifted throughout the specimen, and the signal is gridded based on the spatial location of the FFL with time. The gradient and shift coils are used to create the FFL and shift it in the x-direction, while the linear motor stage translates in the z-direction to make a projection image. The pulse sequence for the gradient and shift coils is shown in further detail in Figure 3.20. As you can see, the current from each coil is offset from the baseline gradient level and linearly varied over time to shift the FFL (highlighted in pink). When no respiratory gating is required, multiple lines in x can be scanned without ramping the current all the way to and from zero for each line. The FFL is held at the edge of the FOV while the linear motor moves the specimen in the z-direction.

Respiratory gating is enabled during *in vivo* imaging studies. A small pneumatic pillow is placed next to the animals' abdomen and used in conjunction with a BIOPAC system (BIOPAC Systems, Inc., Goleta, CA) to collect a respiratory waveform of the animal. A digital triggering unit is used to create pulses from the respiratory waveform. An example

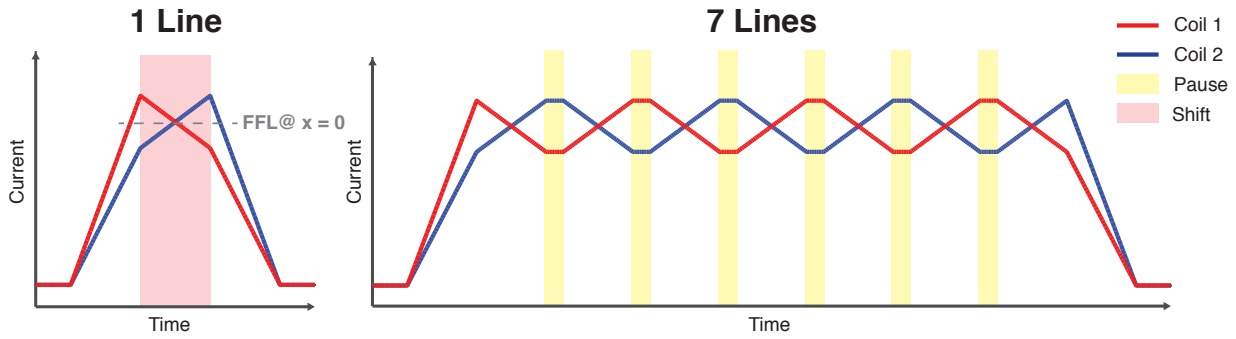

Figure 3.20: **FFL Shift Coil Pulse Sequence.** *Left*: When shifting the FFL from x = -FOV/2 to +FOV/2 once. The current is ramped up from zero, the FFL is shifted (highlighted in pink), and then the current is ramped back to zero. The gray dotted line represents the current level required in both coils for the FFL to be at the iso-center of the magnet in the x-direction. *Right*: When shifting the FFL from x = -FOV/2 to +FOV/2 for 7 times. Instead of ramping the current all the way back down to zero for each line in x, the position of the FFL is held at the edge of the FOV (highlighted in yellow) while the motor moves the specimen in the z-direction to create a 2D projection.

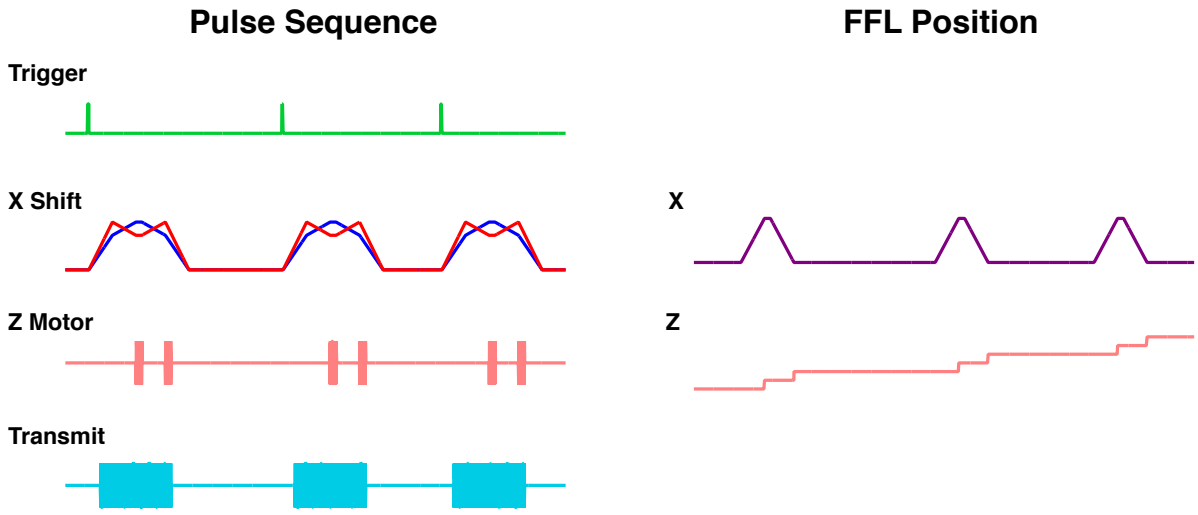

Figure 3.21: **FFL Imaging Pulse Sequence.** *Left*: Example pulse sequences with respiratory gating. During animal's breath hold, the transmit drive field is turned on, and the gradient and shift coils shift the FFL in the x-direction. The linear motor is turned on when the FFL is held in place at the edge of the field of view. *Right*: Corresponding FFL position. The x-axis of all plots represent time.

imaging pulse sequence and corresponding FFL position is illustrated in Figure 3.21. In this sequence, two lines in the x-direction are scanned in each breath hold as a module. The current is ramped from and to zero between breaths for safety. The breath trigger pulse, currents in the gradient/shift coils, as well as currents in the transmit coil and linear motor are illustrated. Note the corresponding FFL position shown in the panel on the right. The number of lines and length of pauses are determined by the FOV in the z-direction as well as the z increment required. The offset current can be changed to change the FOV in the x-direction, while the baseline current can be changed to achieve different gradient strengths for the magnet. The field contour maps of shifted and centered FFL are shown in Figure 3.22.

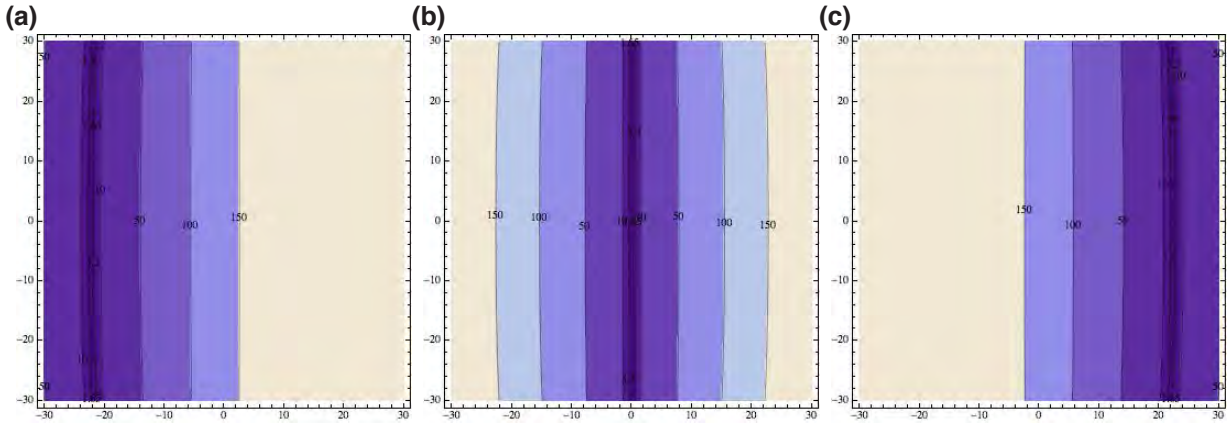

Figure 3.22: **Field Contour Map of Shifted FFL.** (a) FFL at left edge of the FOV, current is offset by 20% of baseline level in each coil (Left coil: -20%, Right coil: +20%). (b) Both coils are supplied the same baseline gradient current for the FFL to be at the center of the FOV, (c) FFL at right edge of the FOV, current is offset by 20% of baseline level in each coil (Left coil: +20%, Right coil: -20%).

3.5 Full Scale Scanner Construction

A 2-ton capacity Strongway Hydraulic engine hoist (Northern Tool & Equipment Company, Inc., Burnsville, MN, USA) was used to assemble the iron returns and coils. As described previously, the iron returns were held together by custom E-shaped stainless steel plates (18-8, 3/4″ thick). Thirty 5/16″-18 through-tapped screw holes were placed on the structure plate surface, and 5/16″-18 screw holes with 0.6″ or 1″ thread depth were placed throughout the sides of the plate for assembly. Four 5/16″-18 swivel hoist rings (Carr Lane Manufacturing Co., St Louis, MO, USA), a four leg web slings with hooks (McMaster-Carr, Elmhurst, IL, USA) and 5/8″ anchor shackles (The Home Depot Inc., Emeryville, CA, USA) were used to lift and turn the iron returns. Two 24″ × 36″, 2000 lb capacity steel dolly

(McMaster-Carr, Elmhurst, IL, USA) were lined with a 1/16″ neoprene rubber or composite wood panels and used to transport assembled components.

Figure 3.23: **Coil Transportation & Assembly.** (a) A forklift was used to move each coil onto a steel dolly for transportation. (b) The coils were lowered onto the iron return assembly and centered using an engine hoist, a load leveler, and web slings.

Each E-shaped iron return half assembly was prepared for coil mounting (Figure 3.24(a)). Neoprene rubber sheets of 1/16″ thickness were used to line all surfaces of the iron return designed to be in contact with the coils for additional electrical insulation. Custom 18-8 stainless steel angle brackets and clamping plates were manufactured (Brightlight Welding & Manufacturing, Santa Clara, CA, USA) to mount the gradient and shift coils. Delrin slabs of 1/4″ thickness with 5/16″-18 through tapped holes (Vanderveer Industrial Plastics, Placentia, CA, USA) were manufactured and attached to the custom angle brackets for insulation and friction fit. The clamping plates were lined with neoprene rubber for the same purpose. The steel angles and delrin slabs were attached to the iron return assembly plate. Nylon web twisted eye web slings were then secured around the coil and mounted onto a Duralast Engine Leveler (AutoZone, Oakland, CA, USA) with 3/8″ anchor shackles (The Home Depot, Emeryville, CA, USA). The entire assembly was lifted by the engine hoist and lowered onto the iron return (Figure 3.23(b)). After the magnets were centered, 7″ long 5/16″-18 bolts were used along with stainless steel washers and nylon insert lock nuts (McMaster-Carr, Elmhurst, IL, USA). The bolts connected the insulated mounting plates and clamping plates across the coil to mount the coil to the iron return by friction fit. A photo of the iron return half assemblies with mounted coils is shown in Figure 3.24(b).

After the coils were mounted, the two halves were assembled. This was done by turning one of the halves by 180° and slowly lowering it onto the other half assembly. Four custom stainless steel assembly straps (Brightlight Welding & Manufacturing, Santa Clara, CA, USA) were secured onto the bottom iron return half assembly to and used as a guide during the assembly process. After both halves were aligned, Forty 1.25″ long 5/16″-18 bolts were

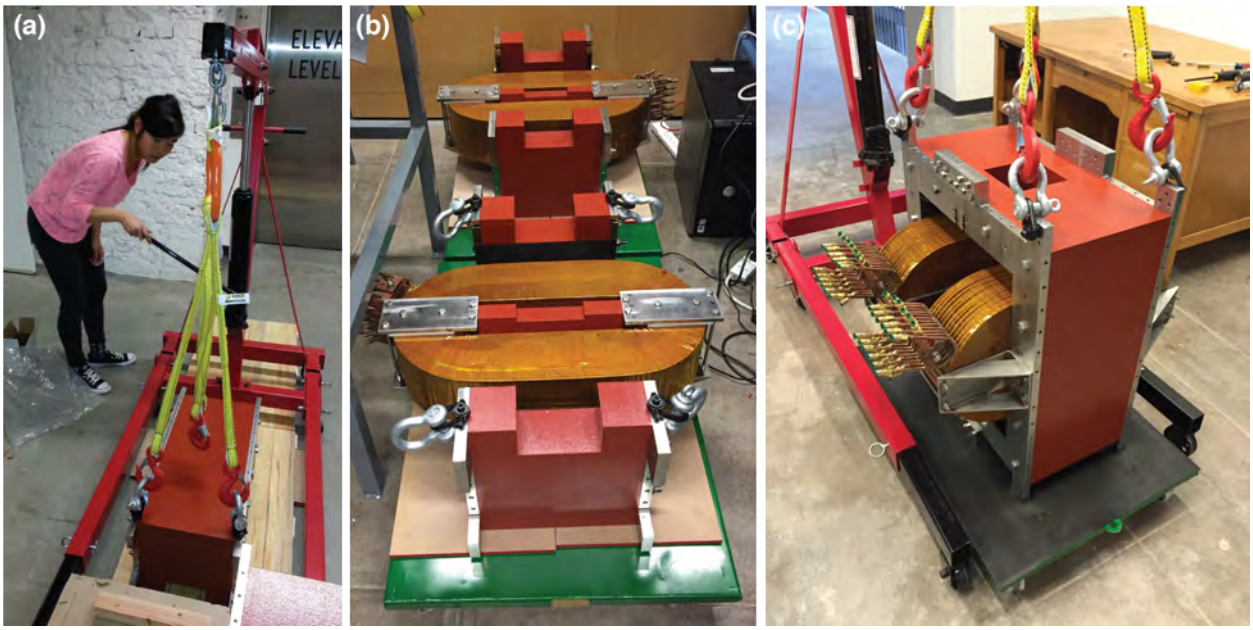

Figure 3.24: **Magnet Assembly Photos.** (a) Each half of the iron return is flipped and transported for coil mounting. (b) Each coil is centered and securely mounted onto the one of the E-shaped iron return half assemblies. (c) The two halves are assembled with custom stainless steel plates, and the entire assembly is turned for final mounting in the shield room.

used to secure the two halves together using the custom stainless steel straps. The entire assembly is then flipped to the final orientation. As mentioned previously, the scanner is designed to be mounted on a heavy duty steel table with a linear motor as well as electrical and cooling connections to be accessed below the scanning. The entire assembly needs to be inside our existing shielded room (ETS-Lindgren, Cedar Park, TX, USA) to prevent EM interference. As seen in Figure 3.25, there is a 6″ threshold at the shielded room door. Therefore, we constructed two temporary platforms to straddle the shielded room threshold. A 3/4″ × 4′ × 8′ particle wood panel, 2″ × 8″ × 8′ wood and 1″ × 6″ × 4′ pine boards (The Home Depot, Emeryville, CA, USA) were cut to size with a jigsaw and assembled using nails into two separate platforms. The magnet assembly was first lifted onto a steel dolly placed on one of the platforms outside the shield room. The engine hoist was then moved into the shield room. The platforms were then used along with the dolly to move the magnet assembly across the threshold. Once inside the shield room, the magnet assembly was lifted for the platform to be removed and lowered onto the steel dolly on the ground, as shown in Figure 3.25(a). The heavy duty table was brought to the center of the shield room when the magnet assembly was lifted, and the magnet was lowered gently while being aligned onto the custom steel enforcement angle brackets on the surface of the table, as seen in Figure 3.25(b). The steel angle brackets were machined with through holes and secured to the table top with 2.5″ long 1/4″-20 bolts. Copper shims were used at the contact points

between the magnet and the steel angle brackets, and the whole assembly was secured with 5/16″-18 bolts onto the table via custom machined brackets. The table was subsequently bolted down to the concrete floor.

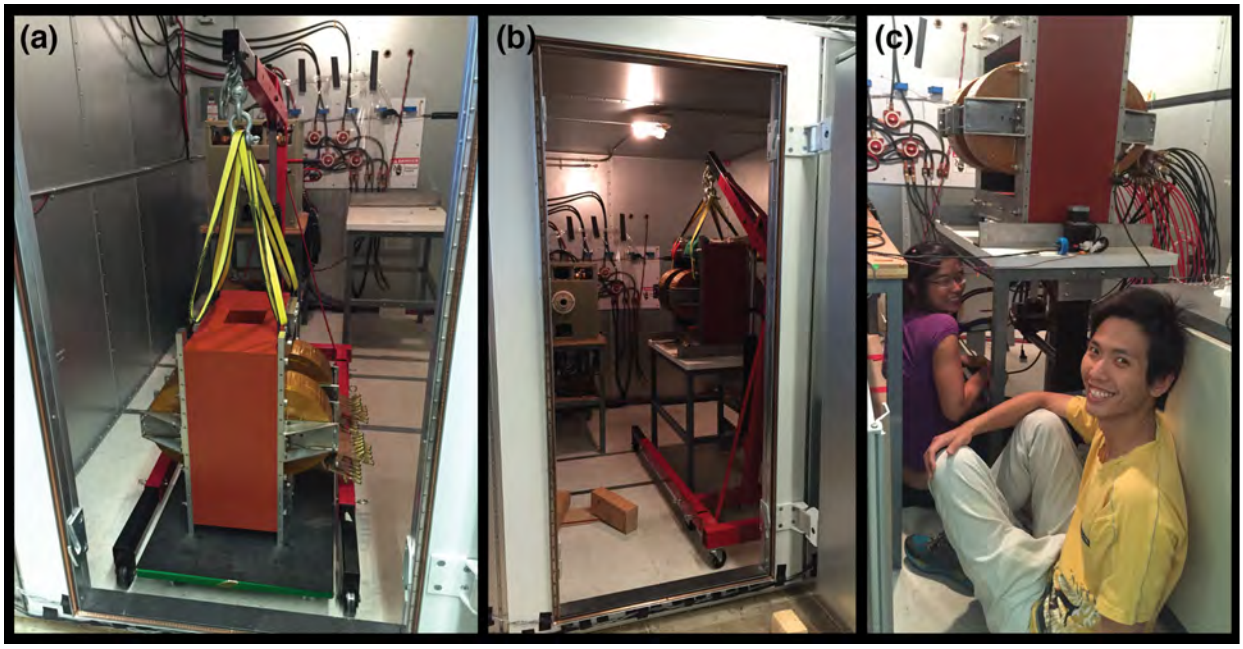

Figure 3.25: **Final Magnet Mounting & Cooling System Installation.** (a) The magnet assembly successfully transported into shield room. (b) The magnet assembly mounted onto the table to enable vertical bore imaging. (c) Installation of cooling manifolds, fittings, and plastic tubing for 24 parallel water circuits.

Custom 1/2″ thick G10 fiberglass plates (Vanderveer Industrial Plastics, Placentia, CA, USA) with tapped and clearance holes throughout were mounted onto two sides of the assembly for assembly and protection. The copper bore was lowered into the magnet assembly and secured to the top fiberglass plate. A custom delrin ring and a 3D printed former were secured to the lower fiberglass plate and end of the copper bore. The 3D printed former was used to center and mount the transmit coil. The receive coil was wound on a separate 3D printed former and secured to the transmit coil assembly with 8-32 nylon cap screws. We soldered 1/0 gauge wires onto welding lugs (McMaster-Carr, Elmhurst, IL, USA) for power connections. All power and water cooling systems are designed to be switchable between our FFL and FFP systems. See the switching panel in the back of the shield room in Figure 3.25(a). The water circuits of the two systems are connected by a T-valve for ease of switching. A photo of the final assembly is shown in Figure 3.26.

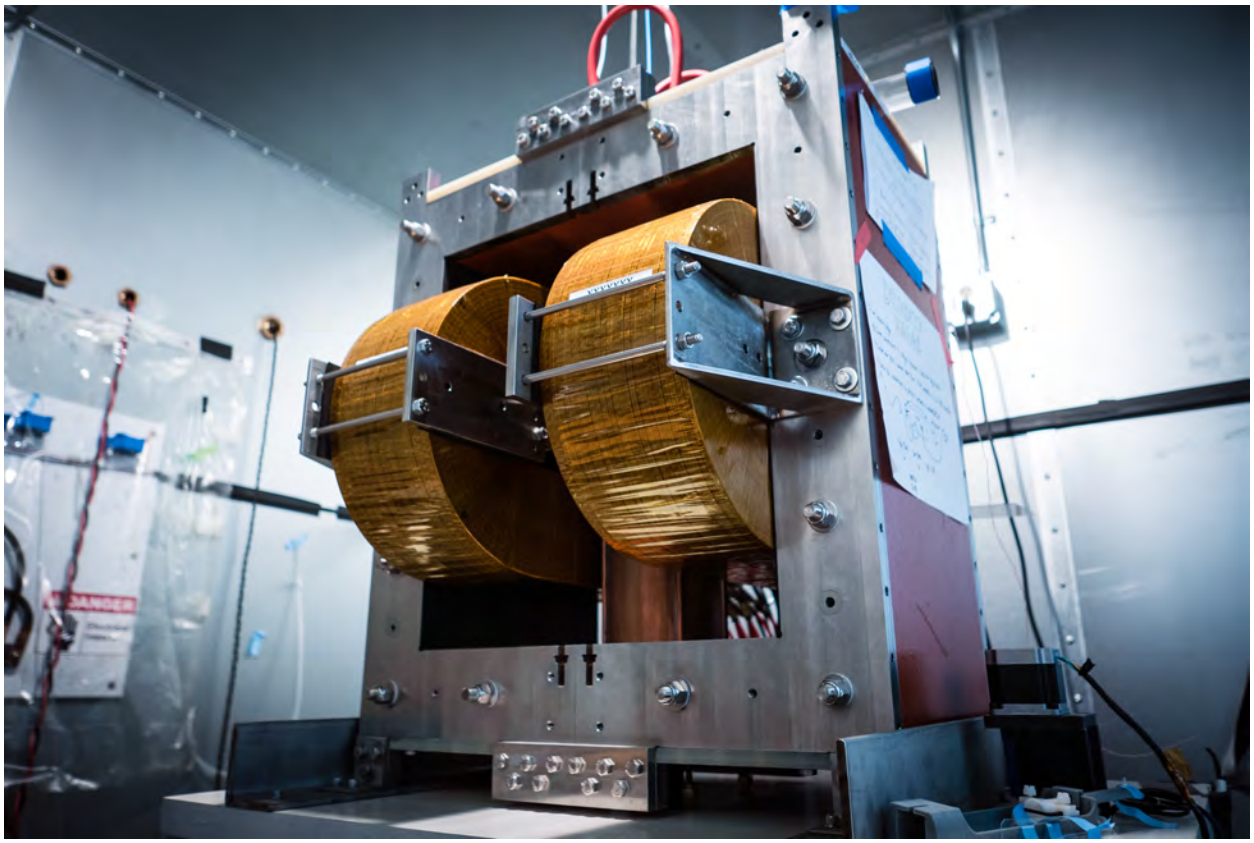

Figure 3.26: **Photo of Final Full Scale FFL scanner.**

3.5.1 Power & Field Gradient

A high voltage differential probe (Tektronix, Beaverton, OR, USA) was used to measure the voltage in each coil during a normal scanning sequence. An AC/DC current clamp (Fluke Corporation, Everett, WA, USA) was used to measure the current supplied to each coil. The results, along with specifications of the imager in its current form are summarized in Table 3.4. The power settings chosen were power and cooling limited.

3.6 High Resolution Imaging Results: Phantom

3.6.1 3D MPI of Spiral Phantom

To test the projection 3D imaging capabilities of our imager, we created a spiral phantom. Microbore PTFE Tubing with an ID of 0.032″ ID and an OD of 0.056″ (Cole-Parmer, Vernon Hills, IL, USA) was taped around a 15 mL conical tube, as shown in Figure 3.27. MPI-tailored SPIO tracer solution (LS-008, Lodespin Labs, Seattle, WA, USA) was diluted to 0.344 Fe mg/mL concentration and injected into the phantom. The ends of the tubing

Property	Unit	Value
Magnet Size	[m]	$0.605 \times 0.325 \times 0.75$
Magnet Weight	[kg]	1000
Peak-to-Peak Voltage	[V]	250
Peak-to-Peak Current	[A]	197
Peak Power	[kW]	12.3
Field Gradient (x)	[T/m]	6.3
Magnet Free Bore	[m]	0.125
Imaging Bore	[mm]	50
Imaging FOV	[mm]	$50 \times 50 \times 150$

Table 3.4: Specification Summary of FFL at 6.3 T/m

were sealed using a Sigillum wax sealant tray (Globe Scientific, Inc., Paramus, NJ, USA). This phantom was taped to our 3D printed imaging bed and loaded into the scanner. We acquired 35 projections of the phantom and performed projection reconstruction using the x-space reconstructed projection images. Each projection had a FOV of 50 × 40 mm and was acquired over the course of 15 seconds. A maximum intensity projection of the resulting 3D MPI volume is shown in Figure 3.27. The spiral tubing is faithfully captured with high image contrast.

3.6.2 3D MPI of Resolution Phantom

An MRI resolution phantom (Bruker Corporation, Billerica, MA, USA) was used to test the resolution of our system. As shown in Figure 3.28, this is a phantom with a grid of small reservoirs spaced at varying distances. All of the 16 tracer reservoirs were filled with MPI-tailored SPIO tracer (LS-008, Lodespin Labs, Seattle, WA, USA) at 3.44 mg Fe/mL concentration. Twenty-seven projections were acquired, and projection reconstruction was performed on the projection images. Each projection image had a FOV of 40 mm × 40 mm × 35 mm. A maximum intensity projection of the 3D MPI volume is shown in Figure 3.28. As you can see, the reservoirs that were spaced 1 mm apart were clearly resolved. Based on analysis of the image, we estimate the spatial resolution to be ∼700 μm in the z-direction, which matches theoretical predictions.

3.6.3 3D MPI of Coronary Phantom

A coronary phantom was created by engraving the shape of a coronary artery into 3 mm thick cast acrylic using a laser cutter (Universal Laser Systems, Inc., Scottsdale, AZ, USA). Thin clear tape was used to create a seal in the coronary shaped channels, and a 30 gauge needle was used to create pressure outlets at the ends of the channels in the phantom. The same syringe was then filled with diluted nanomag-MIP tracer (7.5 mg Fe/mL), and the

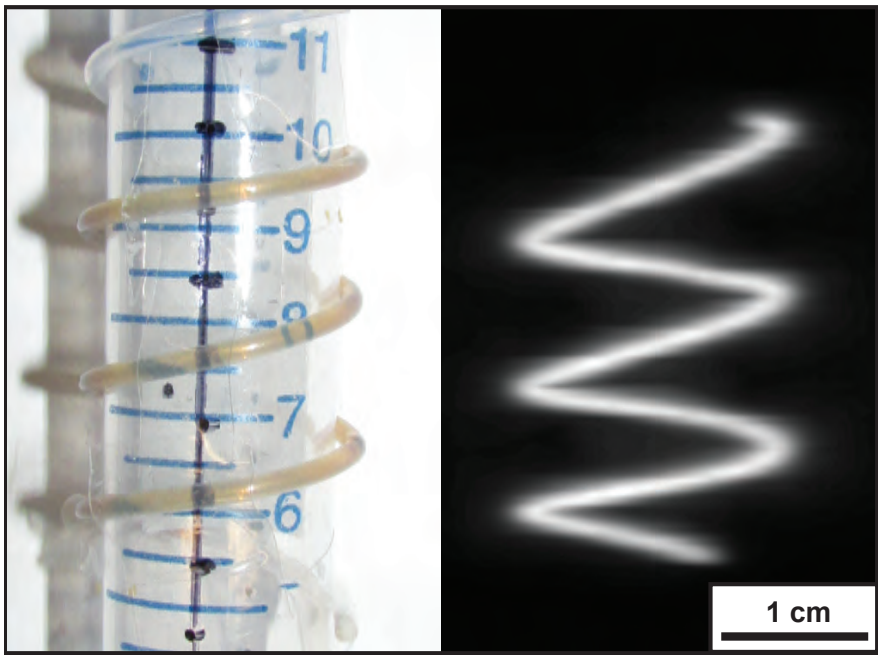

Figure 3.27: **Projection Reconstruction MPI of Spiral Phantom.** *Left*: Spiral phantom containing Lodespin SPIOs (0.344 mg Fe/mL). *Right*: 3D projection reconstruction image of the phantom acquired with the 6.3 T/m FFL MPI scanner. Imaging FOV: 50 mm × 50 mm × 40 mm, 35 projections, 15 seconds per projection.

solution was injected into the phantom. As you can see in Figure 3.29(a), this resulted in small air bubbles in the phantom. The phantom was coated with clear nail polish after tracer injection to prevent evaporation. The finalized phantom was mounted onto a 3D printed former and loaded into the high resolution FFL scanner. 35 projections of the phantom were taken, and projection reconstruction was performed on the reconstructed projections. Each projection was acquired in 20 seconds, and had a FOV of 50 mm × 50 mm. A cropped maximum intensity projection of the 3D MPI volume is shown in Figure 3.29(b). Note that all three air bubbles were faithfully captured in the MPI image.

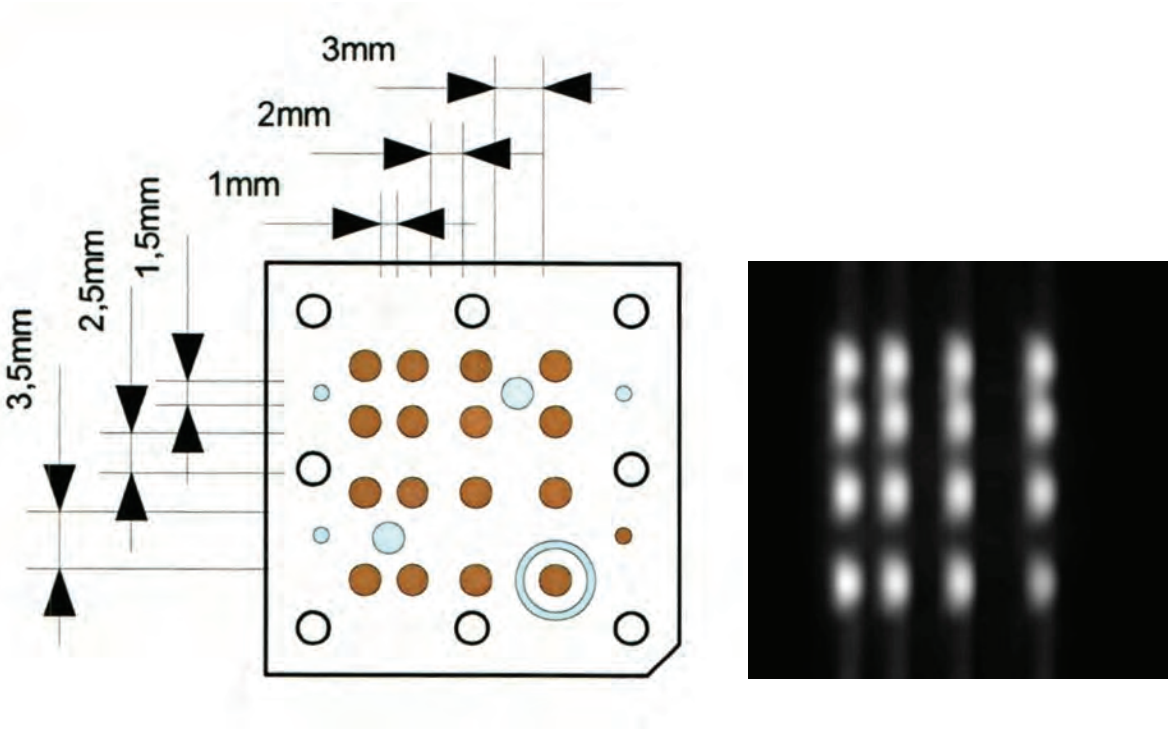

Figure 3.28: **Projection Reconstruction MPI of Resolution Phantom.** Illustration of resolution phantom (courtesy of Bruker) and corresponding maximum intensity projection of the 3D MPI image. Imaging FOV: 40 mm × 40 mm × 35 mm (cropped), 27 projections, 5 minutes total scan time.

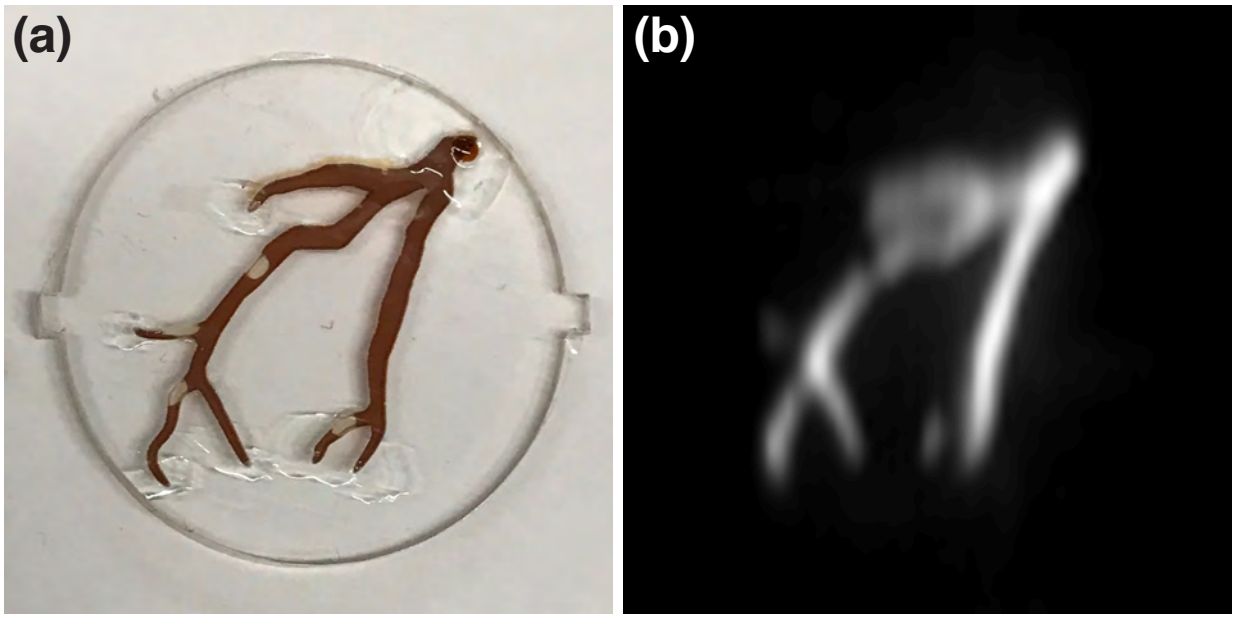

Figure 3.29: **Projection Reconstruction MPI of Coronary Phantom.** (a) Photo of coronary phantom containing nanomag-MIP (7.5 mg Fe/mL) and (b) corresponding maximum intensity projection of the 3D projection reconstruction image. Imaging FOV: 50 mm $\times$ 50 mm $\times$ 50 mm (cropped), 35 projections.

3.7 High Resolution Imaging Results: *in vivo*

3.7.1 Projection MPI Rat Head Angiography

To test the *in vivo* imaging capabilities of our imager, we injected a MPI-tailored long circulating SPIO tracer (LS-008, Lodespin Labs, Seattle, WA, USA) into the tail vein of a rat. A 3D printed animal bed was designed with a nose cone and a bite bar. The bite bar was necessary due to the vertical nature of the imaging bore. Once the animal was loaded into the animal bed, a thin flexible acrylic tube was taped to the bed to protect the animal during imaging. An anesthesia machine (VetEquip, Inc., Livermore, CA, USA) was used to mix 2.5-3.0% isoflurane into oxygen and supply the mixture at 1 L/min. The gas supply tubes were fixed to the top of the shield room with sufficient slack to minimize tube crimping during rotation and translation of the animal bed during imaging. In this study, the rat was injected at a dose of 20 mg Fe/kg, a dose that is high but still in the acceptable therapeutic range. Two projections were acquired, one coronal and one sagittal. The projection MPI result is shown in Figure 3.30. The superb contrast inherent to MPI and the improved resolution allowed for clear visualization and quantification of the anatomic vasculature and perfusion in the rat head.

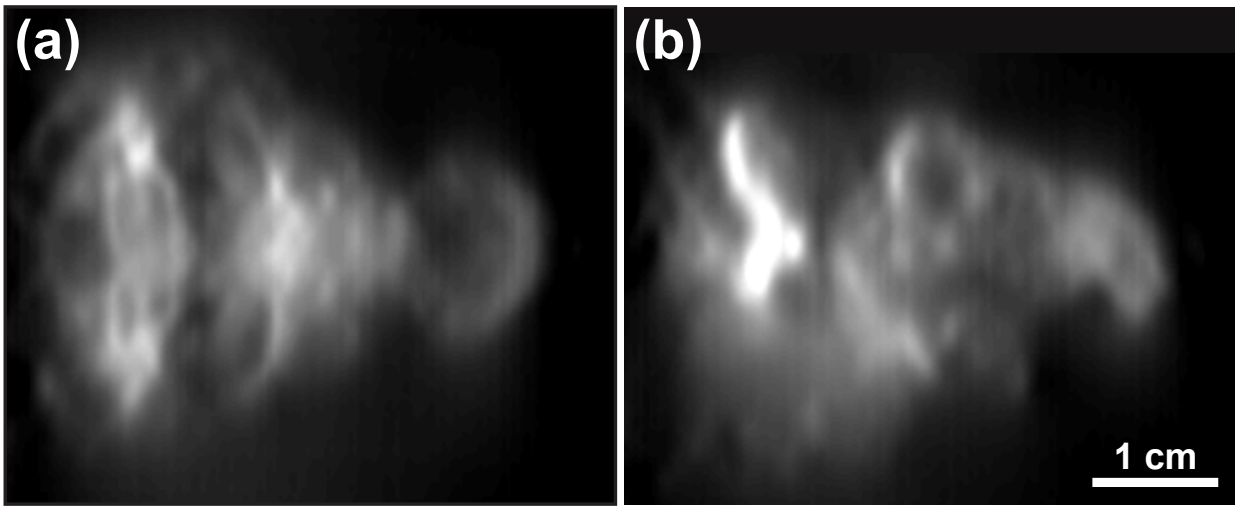

Figure 3.30: **Projection MPI Rat Head Angiography.** (a) Coronal and (b) Sagittal projection MPI image of a rat head with 20 mg Fe/kg long circulating LodeSpin SPIOs injected through tail vein. Imaging FOV: 50 mm × 50 mm (cropped); Scan time: 45 seconds.

3.7.2 Projection Reconstruction MPI Rat Head Angiography

To test the 3D *in vivo* imaging capabilities of our imager, we injected a MPI-tailored long circulating SPIO tracer (LS-008, Lodespin Labs, Seattle, WA, USA) into the tail vein of a rat, this time at a lower dose of 5 mg Fe/kg. The animal was loaded into the custom animal bed, and a small pneumatic pillow was placed on top of the animal's abdomen. A thin flexible acrylic tube was taped to the bed to protect the animal during imaging. The animal was scanned with respiratory gating to minimize motion artifacts. Thirty-five projections were acquired, and projection reconstruction was performed on the projection MPI images. Coronal and sagittal maximum intensity projections of the 3D MPI volume are shown in Figure 3.31. Notice the drastic improvement in resolution compared to the projection images shown in Figure 3.30. The SNR is slightly lower due to the lower injected dose, but the improved resolution allowed us to more clearly resolve the major vessels in the rat head. The blood perfusion throughout the rat head is still visualized.

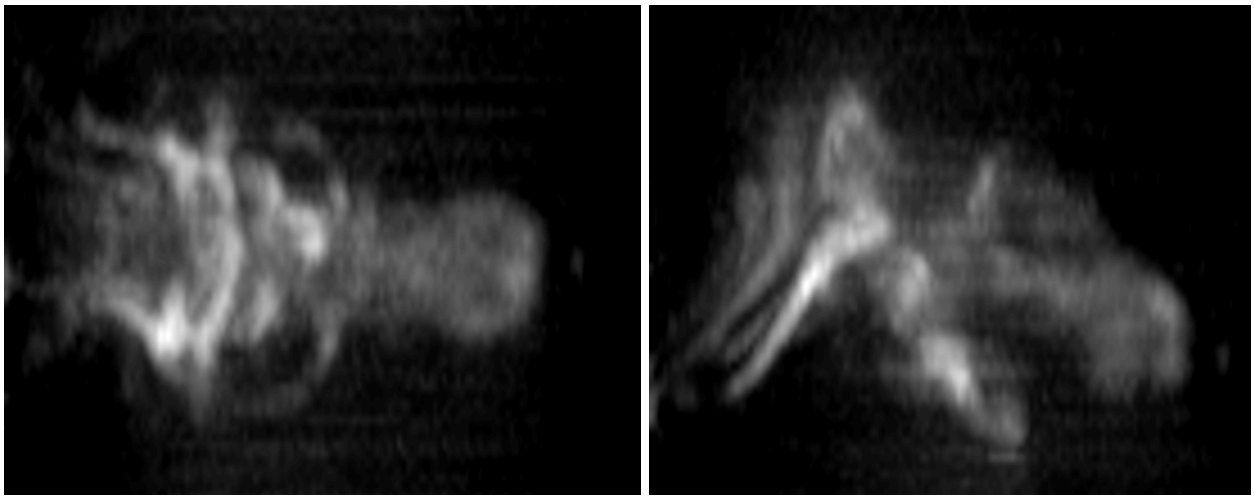

Figure 3.31: **Projection Reconstruction MPI Rat Head Angiography.** 3D projection reconstruction MPI of a rat head with 5 mg Fe/kg long circulating LodeSpin SPIOs injected through tail vein. Imaging FOV: 50 mm × 50 mm × 65 mm (cropped), 35 projections. (a) Coronal and (b) sagittal maximum intensity projections of the 3D volume.

3.8 Discussion & Conclusion

In this chapter, we have shown the design and construction of the world's highest resolution field-free line MPI scanner. This is the first MPI scanner to utilizes iron return electromagnets to shift and create the selection field. After numerous iterations in the design, we first built a $1/8^{th}$ size prototype to validate our simulations of the selection field.

We experimentally validated our design, and proceeded to designed and construct the full scale FFL MPI scanner. Software and hardware modifications were made to the existing system to enable high resolution imaging. We successfully conducted 2D projection and 3D projection reconstruction imaging *in vivo* with this scanner. The improved gradient over our previous FFL system (2.35 T/m) enabled a significant boost in imaging resolution. The improved resolution, coupled with the high speed capabilities due to the flexibility of the projection format are highly empowering. In fact, we leveraged these capabilities to conduct the proof-of-concept study for *in vivo* gastrointestinal bleed detection described in the next chapter.

The 6.3 T/m gradient reported in this work is power and cooling limited. Therefore, it is possible to increase the gradient and improve the resolution further. By obtaining access to a chilled water supply, the cooling efficiency can also be improved. It is important for the gradient along the FFL is remain low to prevent signal fading and loss of resolution. However, when using iron, the nonlinearity of the iron causes the field homogeneity to drift as a function of gradient strength. This is due to the fact that the relative magnetic permeability of the iron changes as a function of its magnetic saturation. Therefore, we have planned for shim magnets in our design to be added along the direction of the FFL to account for this drift. This shimming system can be passive, with pulse sequences designed using a priori models determined through simulation. It can also be active, with real-time measurement of the field at the poles used for feedback control of the current supplied to the shim coils. It is also possible to add high permeability material such as iron, steel, or mu-metal to the iron return as passive shims to reduce power consumption. Further characterization is required for fading and FFL shift nonlinearity under different gradient strength using different particles.

Since this system has a selection field created by an electromagnet, it is now also possible to explore variable gradient imaging. In some applications, it may be beneficial to trade off resolution for higher imaging speed. One can also envision an imaging session where a lower resolution scout scan is performed first to determine a FOV of interest for high resolution imaging. In addition, along with changes in the excitation field amplitude and frequency to improve resolution or for color MPI [10, 94, 95], where different tracers may be distinguished within the same image, variable gradient capabilities can also be explored for these purposes.

The current system has an anisotropic PSF. The resolution in the co-linear (z) direction is currently 2$\times$ worse than that of the transverse (x) direction. Dr. Kuan Lu from our lab has developed system theory and hardware to enable isotropic imaging [96]. There is an ongoing effort in the lab to design the multi-channel transmit and receive coil pairs for this scanner to enable high resolution isotropic imaging. With this hardware, we will also be able to perform equalization, a technique with which the long tails of our Lorentzian shaped PSF can be removed without noise penalty. The theory and algorithm for equalization were also developed by Dr. Kuan Lu [97, 98], and can be applied to images acquired using the FFL with the new transmit and receive hardware.

Our current system relies on mechanical translation of the imaged specimen in the z-direction in increments. This reduces the image acquisition speed considerably. We are

currently investigating techniques to increase the speed of the motor translation without introducing interference. Our design of the system also accounts for an additional pair of gradient and shift coils in the z-direction, orthogonal to the existing coils. These coils will serve to electronically shift the FFL in the z-direction. The addition of these coils will result in a significant speed-up, similar to the twenty-fold speed boost achieved in our previous low gradient system [6]. This coil pair will also further boost the selection field gradient. A few other strategies are currently being investigated to speed up image acquisition. Compressed sensing can be used to reduce the number of projections required for 3D projection reconstruction [99, 100]. In addition, a helical scanning trajectory similar to that used in CT [101] can be implemented as well.

3.9 Acknowledgement

The design and construction of the high resolution FFL MPI scanner was done in collaboration with Dr. Patrick W. Goodwill, Zhiwei Tay, Paul Keselman, Xinyi Y. Zhou, and Dr. Bo Zheng. This work was built off of the imaging theory for projection MPI and projection reconstruction MPI developed by Dr. Patrick W. Goodwill and Dr. Justin Konkle. MPI theory, reconstruction algorithms, and transmit and receive chain components were modified from the existing the system designed by Dr. Patrick W. Goodwill, Dr. Bo Zheng, Dr. Kuan Lu, and Dr. Justin Konkle. *In vivo* and phantom studies were done with the assistance of Dr. Prashant Chandrasekharan, Yueting Shi, and David Mai. MPI-tailored high resolution SPIO tracers were developed by University of Washington and Lodespin Labs, LLC: Dr. Amit P. Khandhar, Dr. R. Matthew Ferguson, Dr. Scott J. Kemp, and Prof. Kannan M. Krishnan.

Chapter 4

Projection Magnetic Particle Imaging for Quantitative Gastrointestinal Bleed Detection

4.1 Introduction

Gastrointestinal (GI) bleeding is a serious clinical problem and a common cause of hospitalization. Hospital admissions for GI bleeding in the United States and United Kingdom has been estimated at up to 150 patients per 100,000 population per year with a mortality rate of 5-10% [102]. GI bleeding is a diagnostic challenge both in its acute presentation, which requires the point of bleeding to be located quickly, and in its chronic presentation, which requires repeated examinations to determine its etiology [103]. Although methods for diagnosing the bleeding have drastically improved in the past 20 years, they are, unfortunately, not universally successful. In fact, as many as 8 - 12% of patients fail to have the precise origin and location of bleeding identified before an operation, despite exhaustive diagnostic evaluation. [104]. GI bleed can be a result of trauma, diverticular disease, inflammatory bowel disease, neoplasia, coagulopathy, arteriovenous malformations, and radiation induced proctitis/enteritis. Accurate and timely diagnosis is essential in order to reduce the morbidity and mortality, the length of hospitalization and the transfusion requirements.

Well established techniques for diagnosing GI bleeding include endoscopy, CT angiography, catheter angiography, and radionuclide scintigraphy [105]. In this work, we will focus on lower GI bleeding, which is defined as bleeding originating distal to the ligament of Treitz. Although colonoscopy has the highest efficacy in assessing major bleeding events in the lower GI tract [106], bowel preparation (which may cause a 3–4 hour delay [103]) is necessary for high diagnostic accuracy. In addition, colonoscopy is unable to examine most of the small bowel and introduces risks associated with sedation, perforation and increased bleeding [102]. CT angiography is commonly used, as it is widely available, does not require bowel preparation, and is minimally invasive. Catheter angiography is an invasive technique

that is used with the added advantage of therapeutic intervention capabilities at the time of diagnosis. However, both techniques require the rate of ongoing arterial bleeding to be at least 0.5 mL/min to reliably show extravasation of contrast into the bowel lumen [107]. The most sensitive imaging modality for GI bleeding is radionuclide imaging, with a bleed rate detection threshold of 0.1 mL/min [108]. Radionuclide scintigraphy for GI bleeding are either done with technetium-99m (^{99m}Tc) sulfur colloid or ^{99m}Tc-labeled red blood cells (RBC). ^{99m}Tc) sulfur colloid requires no preparation and can be directly injected into the patient. However, it has a short blood half-life (2–3 minutes), which means the patient must be actively bleeding during the few minutes the label is present the blood, and repeated scanning for intermittent bleeding is not possible without re-injection [104]. ^{99m}Tc-labeled RBC scan is the preferred scintigraphic technique for lower GI bleeding due to the long blood half-life: tracer can be detected on delayed images for up to 24 hours after injection [109]. An *in vitro* kit is typically used to label RBCs in a blood sample with ^{99m}Tc and re-introduced into the patient for imaging. *in vivo* methods that do not require blood to be extracted from the patient are also available, but the image quality is often reduced [110]. ^{99m}Tc-labeled RBC scans can detect active and intermittent bleeding with 80–98 % sensitivity [111]. Due to poor anatomic localization of the bleeding site, a positive ^{99m}Tc-labeled RBC scan result is typically followed up with angiography to accurately localize the bleed site prior to therapeutic intervention.

Magnetic Particle Imaging (MPI) [3, 4, 14, 54], is an emerging tracer imaging modality that directly measures the location and concentration of Superparamagnetic iron-oxide nanoparticles (SPIO) *in vivo*. A time-varying homogeneous excitation field is applied during signal generation, causing SPIOs to instantaneously flip, thereby inducing a signal in the receive coil. A field-free region (FFR) is created with a strong magnetic gradient to localize the signal– only the particles at the FFR are able to flip and generate signal. The FFR is then rastered through the FOV, and the signal detected is assigned to an image location corresponding to the instantaneous location of the FFP [36]. The field-free region can be a field-free point or a field-free line (FFL). To image a 3D field of view (FOV), an FFP is rastered in all 3 dimensions to create a 3D MPI volume, whereas an FFL can be rastered in 2 dimensions to create 2D projections of the 3D imaging FOV, increasing imaging speed [17]. 3D volumes can also be made with an FFL scanner by taking 2D projections at different angles and reconstructing with a filtered back projection algorithm [37], akin to computer tomography. A custom-built 6.3 T/m FFL MPI scanner [58] was used for this study. The dynamic *in vivo* projection imaging process is illustrated in Figure 4.1.

MPI is linearly quantitative, as shown in Figure 4.5. MPI is also highly sensitive, detecting nanograms of iron (200 labeled cells) per voxel [2, 24]. The current resolution with MPI-tailored SPIOs [13, 57] is approximately 1 mm, but may be improved to better than 300 μm resolution with optimized nanoparticles and pulse sequences [10]. Due to the low frequency magnetic fields used in MPI, there is zero signal depth attenuation, and there is zero signal from the tissue itself – only particle signal is visualized. When the SPIO tracer is used as a blood pool agent, tissue perfusion and tracer extravasation are clearly visualized. In addition to producing no ionizing radiation, iron-oxide tracers are also safe, some of which

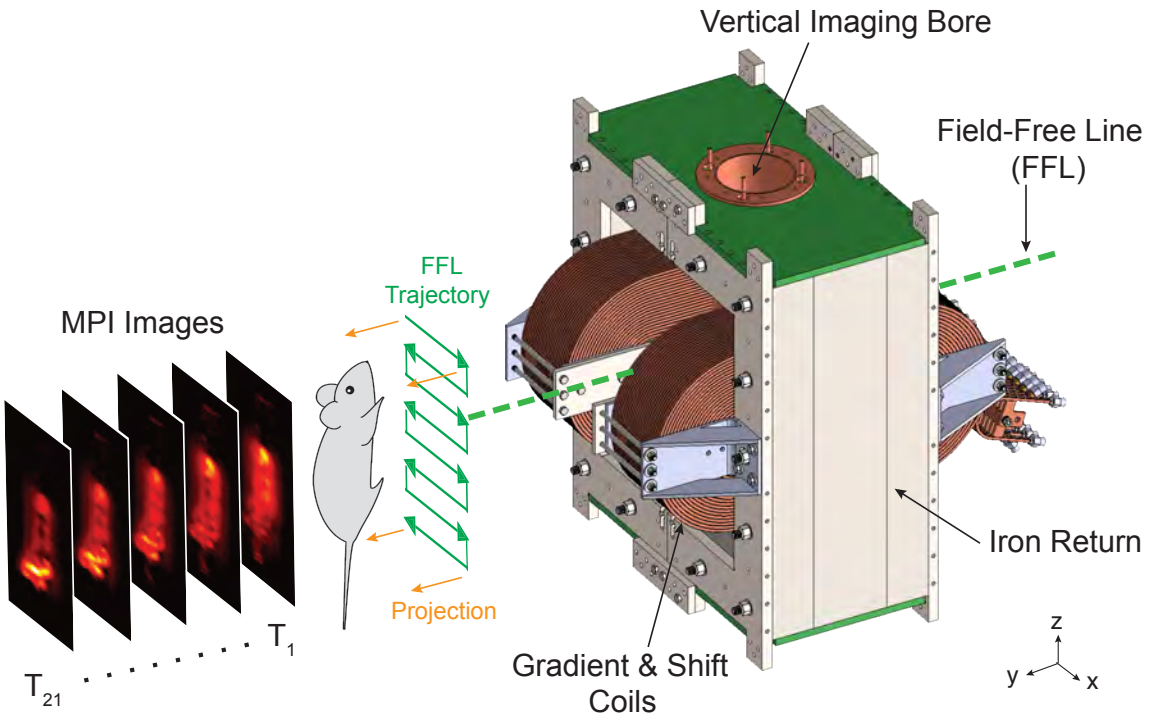

Figure 4.1: **Dynamic Projection Field-Free Line (FFL) MPI.** A custom-built vertical bore 6.3 T/m Field-Free Line (FFL) scanner is used for this study. The FFL is rastered across the imaging field of view, and 2D projection images are acquired over time.

are clinically approved as MRI contrast agents [39]. Hence, it is safe to repeat serial scans on an animal or human. At present, no human MPI scanner has been developed, but the commercial small animal MPI scanners are comparable in complexity to MRI scanners, so clinical translation should be feasible. The superb contrast, sensitivity, safety, and ability to image anywhere in the body gives MPI great promise for various blood pool imaging applications, including GI bleed detection.

In this study, we used the $Apc^{Min/+}$ mouse model as a disease model of GI bleeding. Apc^{Min} (Min, multiple intestinal neoplasia) is a point mutation in the murine homolog of the adenomatous polyposis coli (APC) gene [112]. This mutation is often found in patients of familial adenomatous polyposis (FAP), a hereditary form of colon cancer. Polyps spontaneously developed in the $Apc^{Min/+}$ mice with age, causing them to bleed and become anemic. To induce acute bleeding, heparin was administered through the tail vein at the beginning of the MPI study. Long circulating MPI-tailored SPIO tracer was then administered as a blood pool agent, and the animals were monitored with MPI over the course of 130 minutes.

For the very first time, we implemented a high spatial and temporal resolution dynamic

MPI projection scanning method to quantitatively detect GI bleeding *in vivo*. Due to the high contrast inherent to MPI, we captured clear images of the nanoparticle dynamics in the blood pool and extravasation into the gut lumen. The high contrast images also enabled quantitation of the blood flow rate into the gut.

4.2 Methods and Materials

4.2.1 Animal Procedures

All animal procedures were conducted according to the National Research Councils Guide for the Care and Use of Laboratory Animals and approved by the Animal Care and Use Committee at UC Berkeley. Male C57BL/6-Apc$^{Min/+}$ (8-week old) were obtained from Jackson Laboratories (Bar Harbor, ME). Male C57BL/6 mice (11-week old) were obtained from a UC Berkeley Office of Laboratory Animal Care approved vendor as wild-type control. All animals were monitored weekly for behavior, body weight and hematocrit level changes until they reached an age of 13-weeks. 10 μL of blood was drawn from the tail vein of each mouse, and the hematocrit level was measured with the AimStrip Hb Hemoglobin Test System obtained from Germaine Laboratories (San Antonio, TX). The experimental flowchart for this study is shown in Figure 4.2. The measured hematocrit levels of each group over time are shown in Figure 4.3.

4.2.2 MPI-tailored Superparamagnetic Iron-Oxide Nanoparticles (SPIOs)

MPI-tailored SPIO tracer (LS-017, LodeSpin Labs) was synthesized [14, 45, 113] to achieve optimal resolution and blood circulation half-life. The SPIOs were synthesized by thermolysis of iron III oleate in 1-octadecene, with subsequent oxidation (1 % oxygen in argon) to achieve desired magnetic behavior [62]. For biocompatibility and long circulation, poly(maleic anhydride alt-1-octadecene) (PMAO)-PEG(20k) coatings were created by attaching 20 kDa Methoxy-PEG-amine (JenKem USA) to PMAO (Sigma) (30-50 kDa) [45]. The SPIOs were then coated with the amphiphilic polymer coating and dispersed in PBS for characterization and animal studies.

Bright field TEM was performed at 200 keV to characterize nanoparticle morphology and size. Selected Area Electron Diffraction (SAED) was performed at 200 keV to characterize crystalline phase. Hydrodynamic size of the coated nanoparticles was measured in PBS using Dynamic Light Scattering (DLS, Malvern ZetaSizer Nano ZS). Magnetic properties were measured by Vibrating Sample Magnetometer (VSM, Lake Shore Cryoronics). Magnetic size was determined by fitting of M(H) data to a Langevin function (following Chantrell's method [63]).

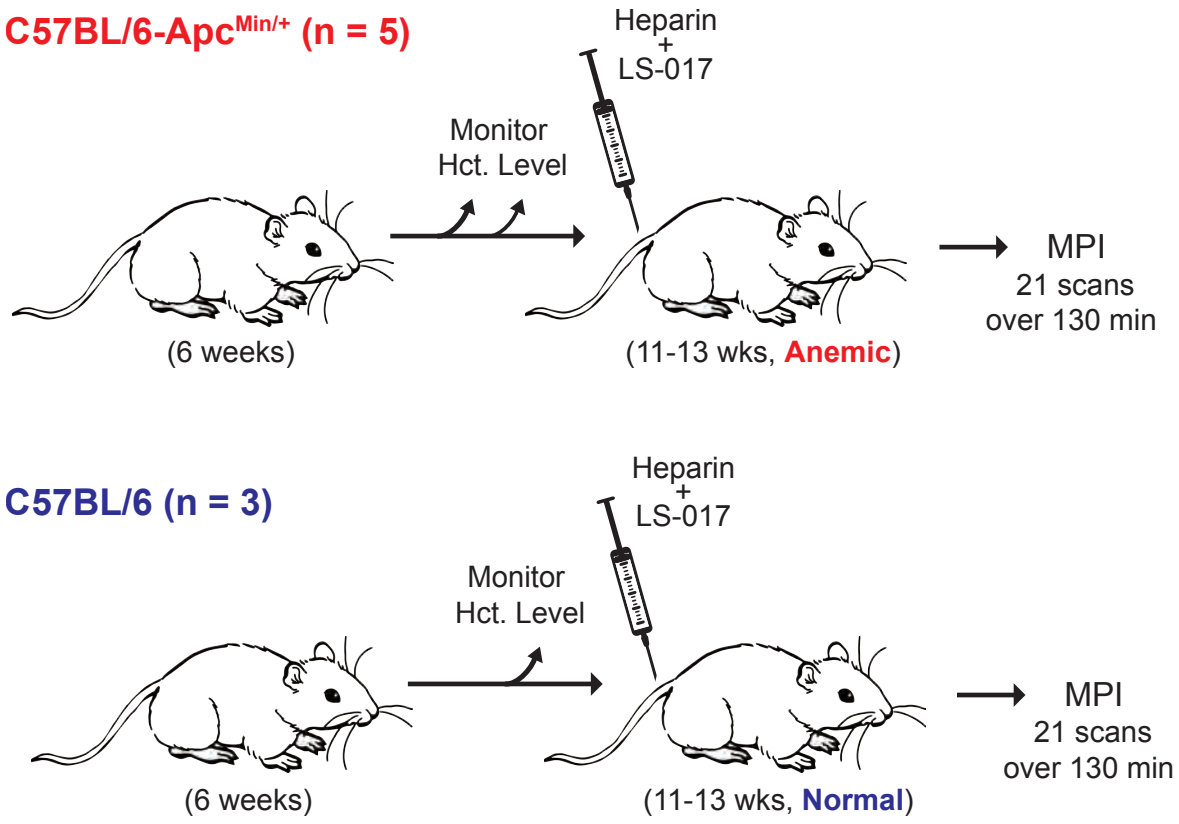

Figure 4.2: **Experimental Workflow.** C57BL/6-Apc$^{Min/+}$ mice (n = 5) and C57BL/6-WT mice (n = 3) were used for this study. Polyps spontaneously developed in the Apc$^{Min/+}$ mice with age, causing them to bleed and become anemic. The hematocrit levels were monitored weekly throughout the experiment. At age 11-13 weeks, Heparin and LS-017 were injected through the tail vein, and 21 projection MPI scans were perform over 130 minutes.

4.2.3 Dynamic *in vivo* Projection Magnetic Particle Imaging

A custom built vertical bore Field-Free Line (FFL) 6.3T/m/μ_0 magnetic particle imager was used for this study. The SPIOs are excited at a drive field frequency of 20.225 kHz and an excitation strength of 40 mTpp. The FFL is created and shifted by a pair of water-cooled gradient and shift coils with laminated iron returns. The FFL is created along the y-direction and electronically shifted in the x-direction as illustrated in Figure 4.1. To complete the imaging trajectory shown, the scanning bed is mechanically translated in the z-direction at 1 mm increments.

MPI-tailored long circulating SPIO tracer (5 mg Fe/kg) and heparin were administered

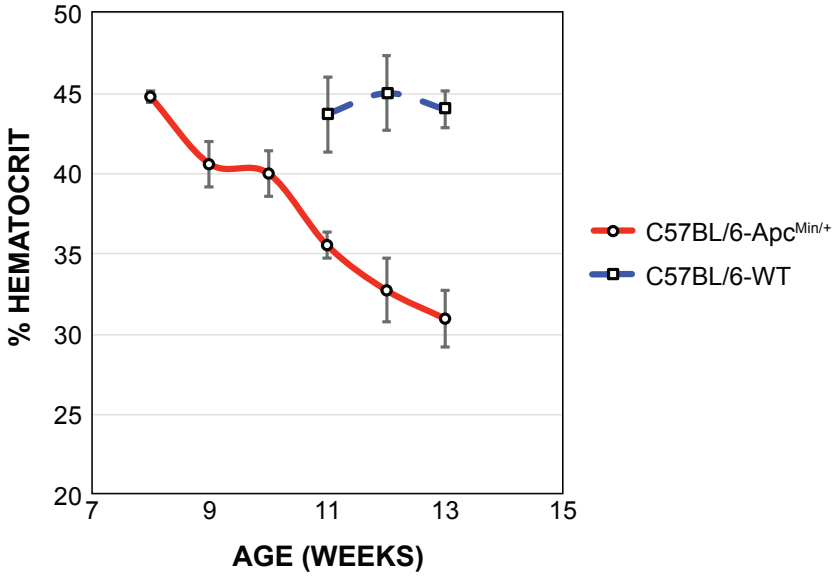

Figure 4.3: **Hematocrit Levels.** Hematrocrit levels in Apc$^{Min/+}$ and wild-type animal groups over time.

through the tail vein of each animal prior to imaging. 21 projection scans were acquired for each animal over the course of ∼130 minutes to capture in vivo tracer dynamics over time. All in vivo images were taken with respiratory gating, with a final field of view of 51.6 mm × 85.2 mm. All images were reconstructed using x-space MPI reconstruction algorithm. [4, 17]. Projection X-Ray images were acquired with a XPERT cabinet X-Ray system (KUB Technologies, Inc) following MPI study for anatomical reference.

4.2.4 Projection Magnetic Particle Imaging Linearity and Detection Limit

To show that our 2D projection imaging method is linearly quantitative, we prepared a phantom of 5 different tubes filled with 10 μL of LS-017 particle solution at various concentrations (0.0625, 0.25, 0.5, 1 and 2 mg/mL, each 10 μL) and imaged it at two different projection angles to create a line image in the 0-degree projection and a point image in the 90-degree projection. The signal was summed around the phantom for both projections for comparison. The system detection limit was also estimated from this study.

4.2.5 Image Processing and Data Analysis

MPI Image Analysis

After x-space reconstruction of the MPI images, the dynamic MPI time courses were collected for each animal. To better visualize the bleed into the gastrointestinal lumen, the image of the first time point is subtracted from the rest of the images in the time course to create difference maps. Since the GI bleed should manifest only as a positive accumulation of tracer over time, all negative changes in the difference maps were set to zero.

A conversion factor from MPI signal to iron (μg Fe) mass was calculated from the aforementioned phantom study. This conversion factor was applied to all MPI images and difference maps to create quantitative tracer distribution images for each animal. These images were overlaid with projection X-Ray images for anatomical reference.

Flow Quantitation through Compartment Fitting

The blood plasma Fe concentration C_p was determined by the MPI signal from the ventricle of the heart. Region of interest (ROI) around the heart was created from the MPI image of the first time point of each animal, and the same mask was applied across the rest of the images in the time course to determine amount of tracer in the heart over time. To determine the amount the amount of tracer extravasated into the gut lumen, a single ROI for each time series was created around the gut using all the difference images, ensuring that all the areas of bleed are captured over time. For the control mice with minimal to no tracer extravasation over time in the gut, the original MPI image was used to draw an ROI around the gut. This ROI mask was then applied across the all the difference images to determine the amount of tracer accumulated in the gut over time as a comparison. All image processing and analysis were performed using MATLAB (Mathworks, Natick, MA).

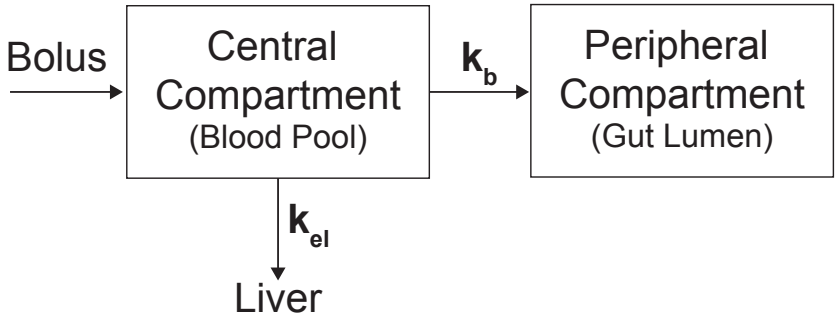

Figure 4.4: **Schematic of Two Compartment Model.** This model is used to quantify the rate of bleed into the gut.

Two methods were implemented to quantify the bleed rate in the gut lumen (a) a non-linear least square method involving compartmental fitting and (b) a modified Patlak plot based linear-least square graphical method assuming irreversible tracer extravasation in the gut lumen. A two compartment model was used for flow quantification of the gut bleed. The two compartments represent the central blood pool compartment and the peripheral gut lumen compartment. The tracer mass in the central blood pool compartment was calculated from the signal in the heart by assuming the heart volume to be 140 μL, and entire blood pool volume of each mouse V_0 to be 1.6 mL. In our model, the tracer exits the blood through two pathways: (1) Elimination due to nanoparticle filtration by the reticular-endothelial system (RES) and (2) Extravasation into the gut lumen due to gut bleed. The fitting was performed with two separate techniques, (1) nonlinear least squares (NLLS) iterative fitting, and (2) linear least squares (LLS) Patlak plot fitting. For the NLLS method, the following equations were used,

$$V = V_0 - k_b t \tag{4.1}$$

$$\frac{dy_1}{dt} = -k_{el} y_1 - \frac{k_b y_1}{V} \tag{4.2}$$

$$\frac{dy_2}{dt} = \frac{k_b y_1}{V} \tag{4.3}$$

where y_1 and y_2 represent the tracer mass in the blood pool and gut lumen compartments, respectively; k_{el} represents the tracer clearance rate to the RES in min^{-1}; and k_b represents the volume transfer constant or the bleed rate into the gut lumen in $\mu L/min$. V_0 is assumed to be 1.6 mL.

For the modified Patlak plot method, the following equation was used,

$$\frac{R(t)}{C_p(t)} = k_b \frac{\int_0^t C_p(\tau) d\tau}{C_p(t)} + constant \tag{4.4}$$

where C_p represents the tracer concentration in the blood pool, and R represents the tracer mass in the gut lumen. Linear least squares fitting was performed to find k_b in $\mu L/min$.

4.2.6 *Ex vivo* MPI and Histology

The animals were euthanized immediately after the dynamic MPI study, and the GI tracts were extracted and imaged with MPI to confirm tracer presence. ROI analysis was conducted on all ex vivo GI tract MPI images, and a linear fit was performed for the *in vivo* and *ex vivo* signal GI tract signal for animals.

After *ex vivo* MPI, the GI tracts were washed and subsequently fixed in neutral buffered formalin (NBF) and transfered to 70 % ethanol after 24 hours. For each animal, GI tracts were separated into 4 segments: stomach, small intestine, cecum, and large intestine. The

stomach and cecum were embedded into one paraffin block. Individual swiss rolls were created for the small and large intestines and both rolls were embedded together into one paraffin block. 5 micron sections were cut from each sample and Hematoxylin and eosin (H & E) staining was performed on all slices to identify the polyp distribution along the GI tracts. The slides were observed using an inverted bright field microscope (ZEISS AX10 Observer D1 with a ZEISS Axiocam ERc 5s).

4.3 Results

4.3.1 Projection Magnetic Particle Imaging Linearity and Detection Limit

A phantom containing SPIO tracer solutions of five different concentrations (0.0625–2 mg/mL, each 10 μL) was imaged with MPI at two different projection angles. As shown in Figure 4.5(a), the projection at 0-degrees resulted in a line image, while the projection at 90-degrees resulted in a point image. 2D Projection-MPI was linearly quantitative ($r^2 = 0.99$), and the detected signal summations were consistent across projection angles, as shown in Figure 4.5(b). A conservative estimate puts the sample with the lowest tracer concentration (0.0625 mg/mL) at 15× the detection limit of our system. The sample tubing had an inner diameter of 0.53 mm (less than our imaging resolution), and was 9.2 mm in length, covering roughly 11.5 imaging voxels. From this, the system detection limit was calculated to be 3 ng of Fe/voxel. However, in order for the bleed to be detectable, it needs to stand out from existing perfused tissue signal in the abdomen. The signal in the abdomen from the control mice compared to background had a signal to noise ratio (SNR) of 17.2. We therefore estimate a final SNR of 50 (3× tissue signal) for the bleed to be detectable. Based on the injected dose of 5 mg Fe/kg with 1.6 mL total blood volume, and assuming final SNR of 50, 2 μL of blood extravasating the gut lumen in one voxel is sufficient for our system to detect.

4.3.2 MPI-tailored Superparamagnetic Iron-Oxide Nanoparticles (SPIOs)

A bright field TEM image of uncoated iron oxide cores of LS-017 and (inset) Selected Area Diffraction pattern showing crystal morphology and characteristic spinel diffraction rings are shown in Figure 4.6(a). A histogram of the core size as measured from the bright field TEM images is shown in Figure 4.6(b). Hydrodynamic size of the particles was 89.3 nm with a PDI of 0.084. The magnetization curve was measured by VSM at room temperature, as shown in Figure 4.6(c). Magnetic size was fit to a Langevin function and determined to be 28.7 nm.

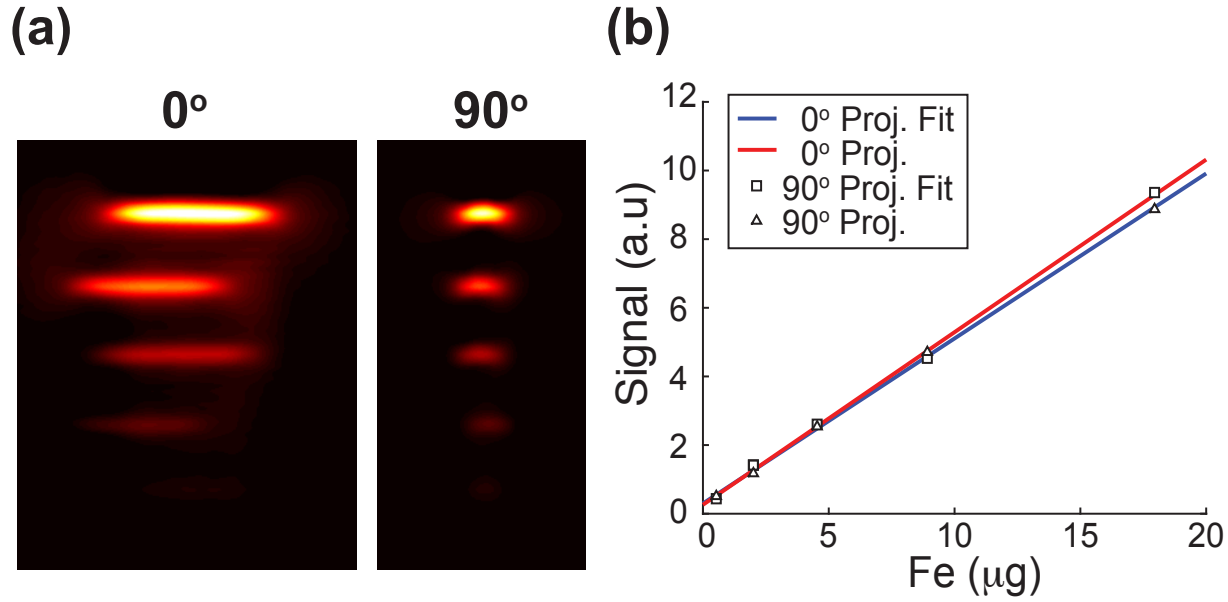

Figure 4.5: **Linearity of Projection FFL MPI.** Top: MPI images of a concentration line phantom (5 concentrations ranging from 0.0625 to 2 mg/mL, each 10 μL) at two different projection angles. Bottom: MPI is linearly quantitative ($r^2 = 0.99$), and the detected signal summation is consistent between projection angles (red, 90 degrees, blue, 0 degrees).

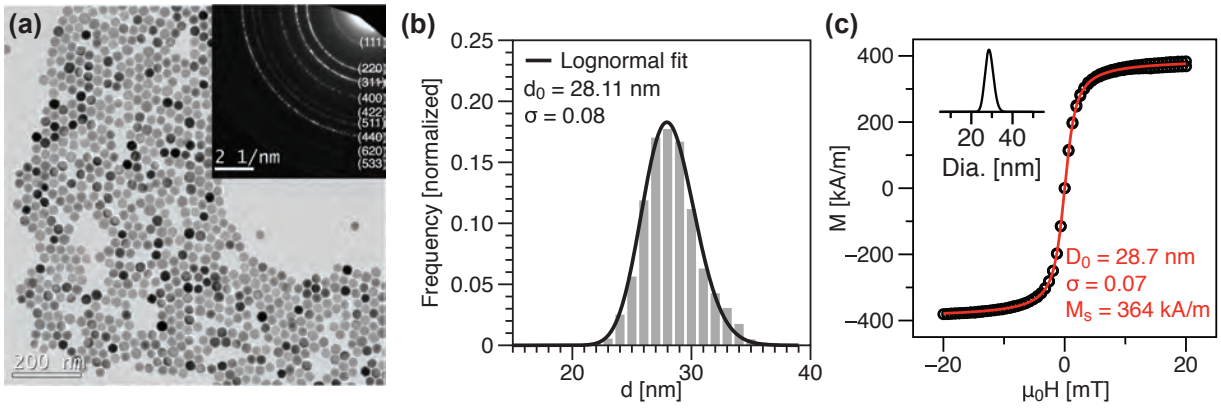

Figure 4.6: **LS-017 SPIO Characterization.** (a) Bright field TEM image of uncoated iron-oxide cores of LS-017 and (inset) Selected Area Diffraction pattern showing crystal morphology and characteristic spinel diffraction rings. (b) Histogram of particle core size from bright field TEM (mean = 28.11, $\sigma = 0.08$). (c) Magnetization curves measured by VSM at room temperature. Magnetic size was 28.7 nm ($\sigma = 0.07$).

4.3.3 Visualizing Gut bleed with Dynamic Projection MPI

Dynamic projection MPI studies were carried out when the hematocrit level of each Apc$^{Min/+}$ mouse became around 30–35% (aged 11–13 weeks), indicating blood loss. Age matched wile-type C57BL/6 mice with hematocrit of 45% were used as control. Long circulating SPIOs and heparin were injected through the tail vein as a bolus, and the dynamic projection MPI study was performed. Representative MPI images were overlaid with projection X-ray for anatomical reference, as shown in Figure 4.7. Whole body tracer dynamics was clearly captured over time. The long circulating SPIOs remained in the blood pool throughout the duration of the experiment, as observed by the strong signal from the heart in both Apc$^{Min/+}$ and control mice.

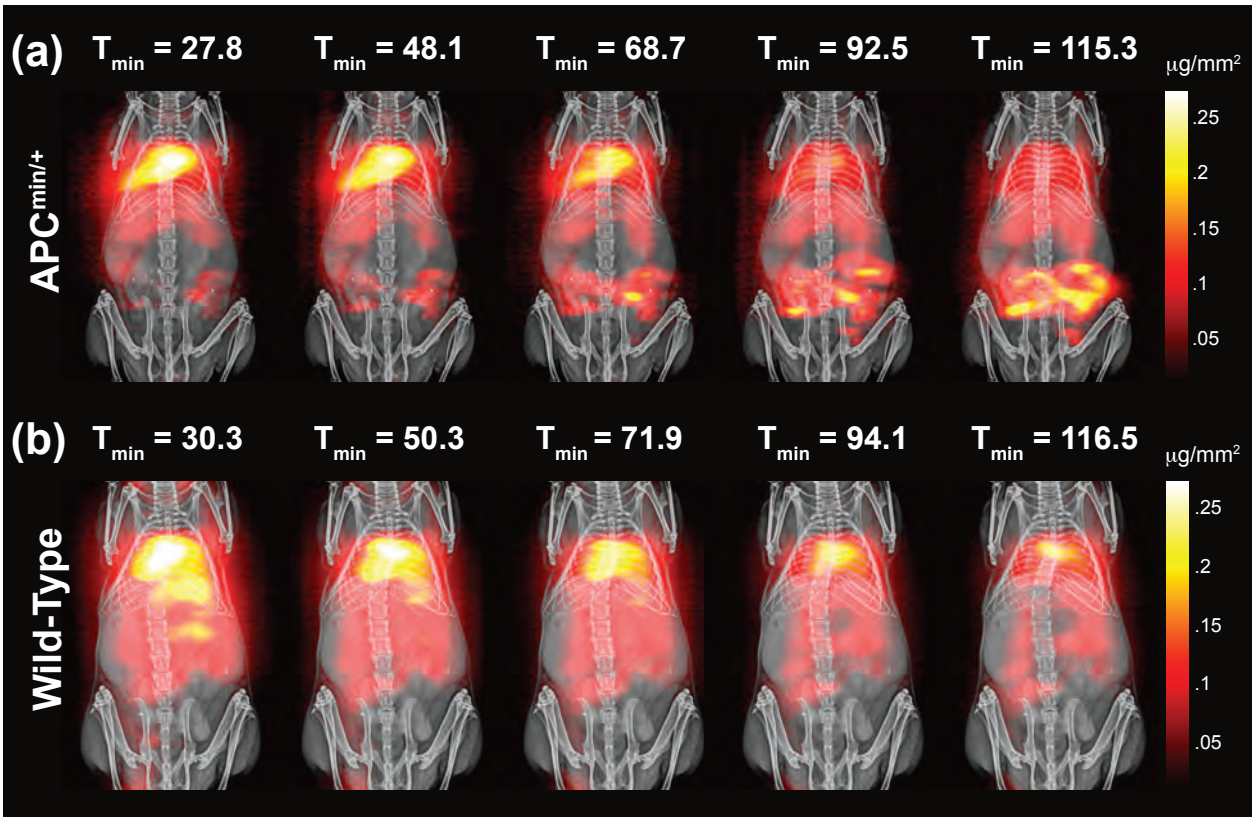

Figure 4.7: **Whole Body Dynamic Projection MPI of Apc$^{Min/+}$ and Wild-Type Mice.** MPI co-registered with projection X-ray for anatomical reference. (a) Representative images of an Apc$^{Min/+}$ mouse over time. MPI clearly captures dynamics of GI bleed over time. (b) Representative images of a Wild-Type mouse over time. No GI bleed is seen.

Tracer extravasation into the gut was clearly visible with time for the Apc$^{Min/+}$ mice, whereas no tracer accumulation was seen in the control mice. Further, the MPI images at the first time point were digitally subtracted from each image in the rest of the time course

for each animal, with negative changes set to zero. The resulting difference images, as shown in Figure 4.8, are quantitative maps of positive tracer accumulation. The gut bleed was visualized with extraordinary contrast in the $Apc^{Min/+}$ mice, whereas minimal changes were seen in the wild-type mice.

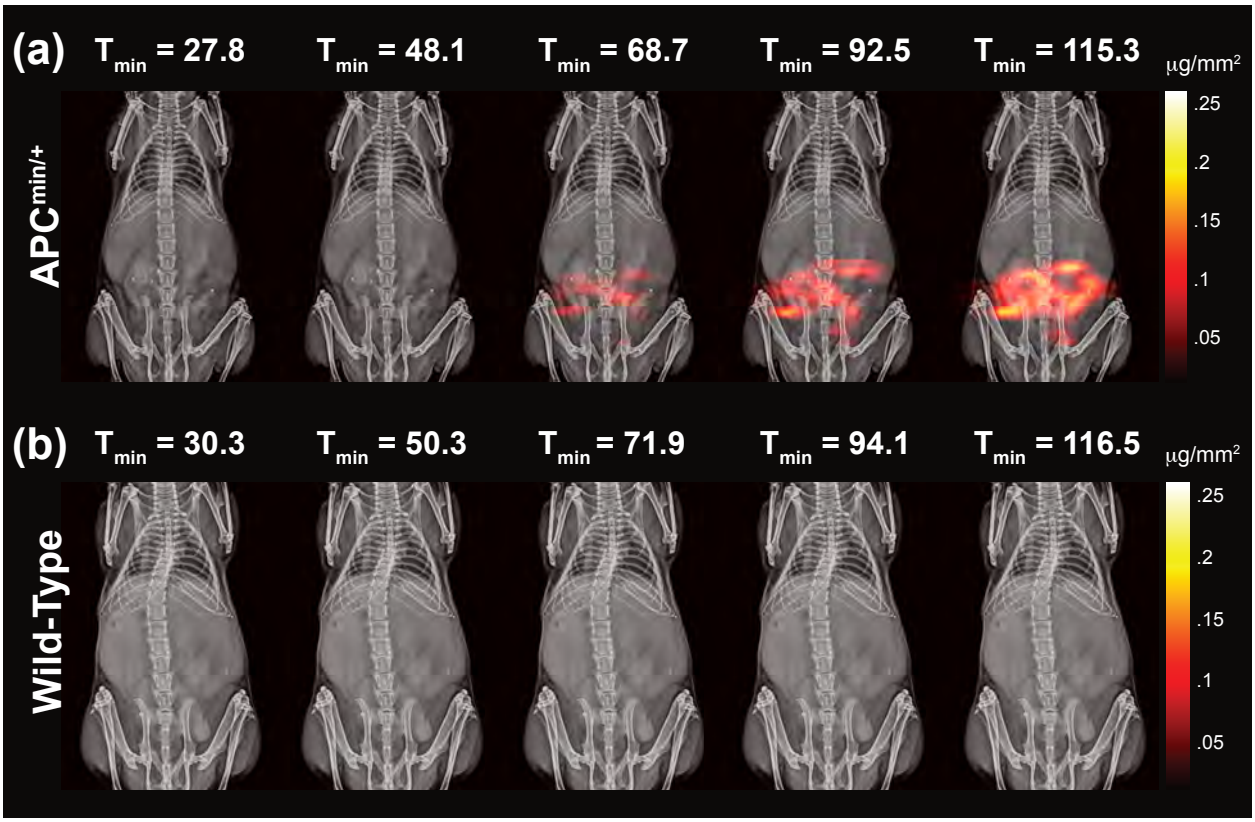

Figure 4.8: **MPI Difference Images of $Apc^{Min/+}$ and Wild-Type Mice.** Each MPI image in the time course was subtracted with that of the first time point to yield difference images. (a) Representative difference images of an $Apc^{Min/+}$ mouse over time. The GI bleed is visualized with extraordinary contrast. (b) Representative difference images of a wild-type mouse over time. No GI bleed is seen.

To confirm that the bleeding visualized in the 5 $Apc^{Min/+}$ mice is indeed the acute bleeding induced by heparin and not merely tracer accumulation in the polyps, we conducted the same dynamic MPI study with no heparin injection on 2 $Apc^{Min/+}$ mice. Representative data is shown in Figure 4.9. The images in the top row are original MPI images with CT overlay for anatomical reference. The images in the bottom row are subtracted MPI images with CT overlay, where the MPI image from the first time point is subtracted from all MPI images in the time course. All negative pixels in the subtracted images were set to zero to capture positive change in signal compared to the first time point. Similar to the healthy

control mice, the Apc$^{Min/+}$ mice with no heparin injection had no accumulation of tracer in the gut.

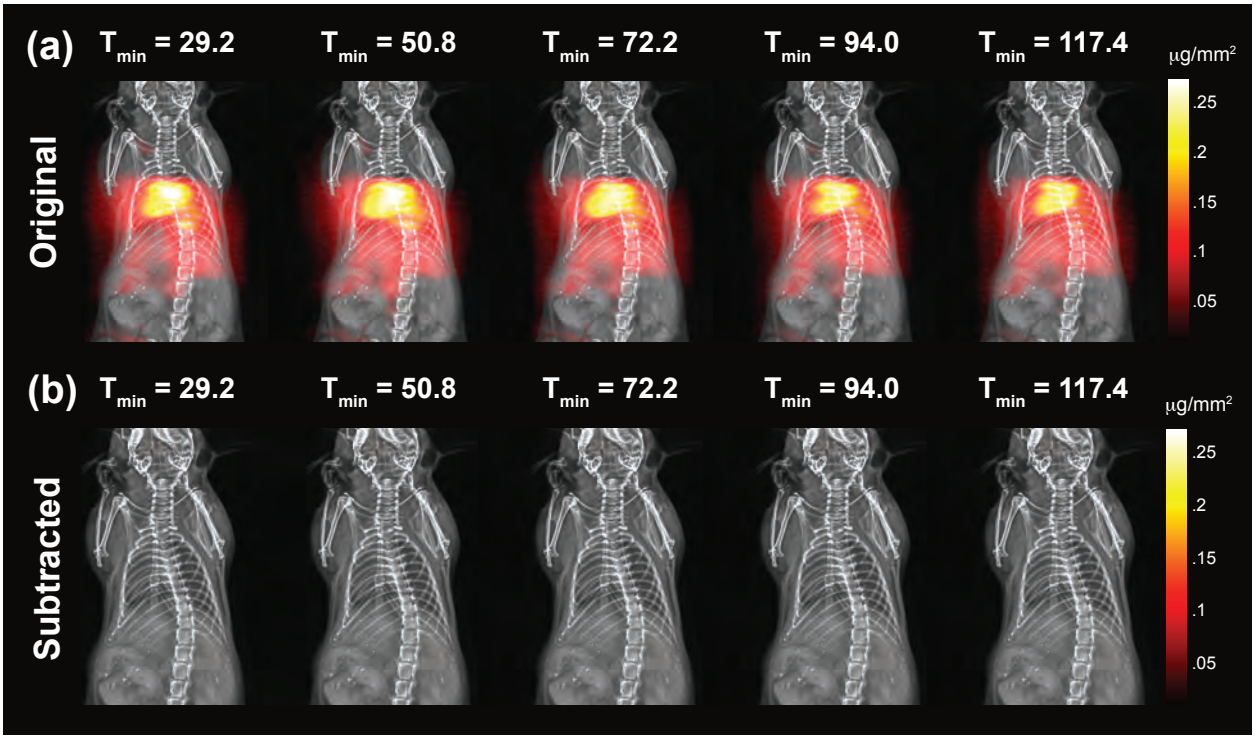

Figure 4.9: **MPI of Apc$^{Min/+}$ mice with no Heparin Injection.** (a) Representative images of an Apc$^{Min/+}$ mouse with no heparin injection over time. (b) Representative subtracted time course images of the same animal. No positive tracer accumulation is observed in the gut.

4.3.4 Gut Bleed Quantitation

The flow rate into the gut lumen was quantified with two methods: (1) Non-linear least squares iterative fitting, and (2) Linear least squares Patlak fitting. Both methods model the system as two compartments. Representative fit NLLS iterative fitting results are shown in Figure 4.10(a) and (b). Note that for both mice, the blood iron levels are similar what we expect based on tracer injection dose (roughly 130 μg Fe is injected in each mouse). This gives us confidence in the quantitative nature of MPI for SPIOs *in vivo*. The amount of tracer accumulated in the gut increases over time in the Apc$^{Min/+}$ mice, while staying close to zero in the wile-type mice throughout the study. Representative linear least squares Patlak fitting results are shown in Figure 4.10(c) and (d). The r^2 value of the LLS fit for the Apc$^{Min/+}$ mouse and wild-type mouse were 0.97 and 0.17, respectively. The low r^2 value

for the wile-type mouse is a result of the near zero accumulation of tracer in the gut lumen over time.

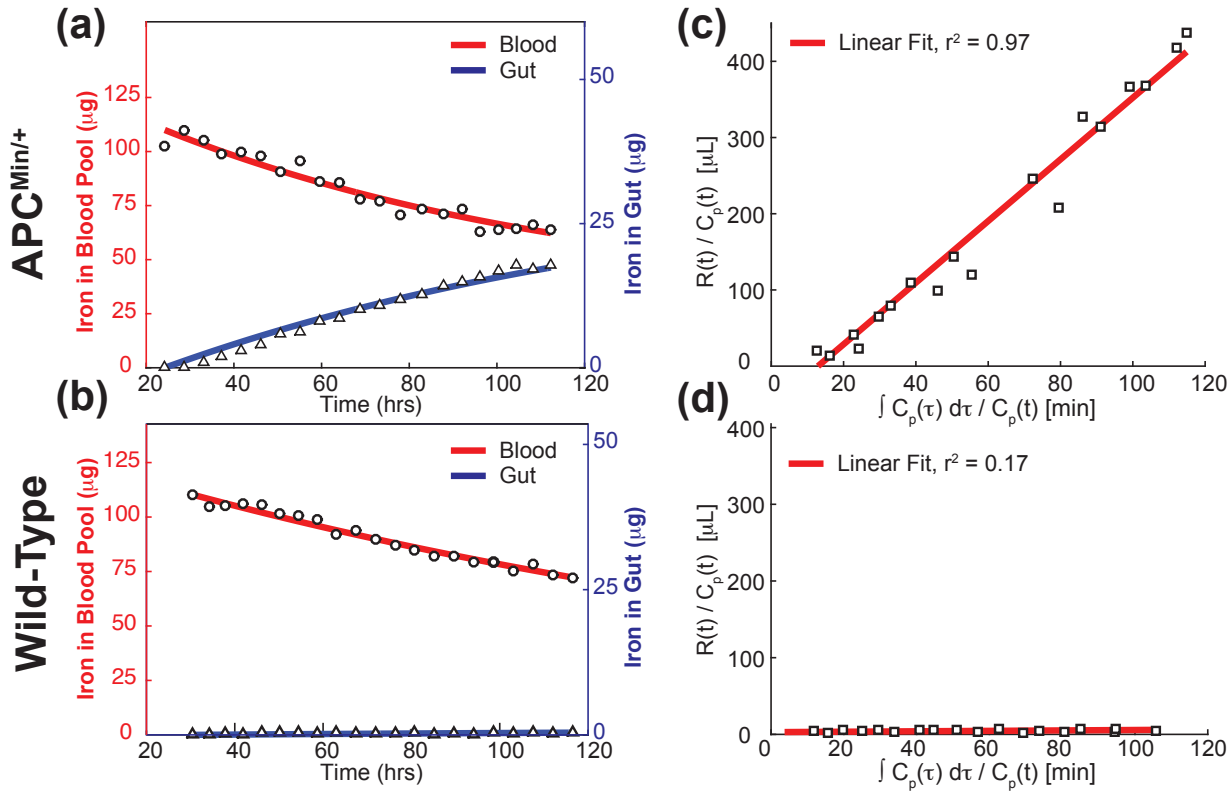

Figure 4.10: **Compartment Fitting Results.** Representative NLLS fit results for (a) Apc$^{Min/+}$ mice and (b) wild-type mice. Representative LLS Patlak fit results for (c) Apc$^{Min/+}$ mice and (d) wild-type mice.

The flow rates were significantly different between the Apc$^{Min/+}$ and control groups for both fitting methods: NLLS method ($p = 0.014$) and Patlak LLS method ($p = 0.007$), as shown in Figure 4.11. There was no significant difference between the flow rates across fitting methods. The flow rates for all animals, along with hematocrit levels when the study was conducted, are tabulated in Table 4.1. Both fitting methods yield similar bleed rates for each animal, with a maximum bleed rate of 4.25 μL/min. Notice that the animal with the largest bleed had the lowest measured hematrocrit level.

4.3.5 *Ex vivo* MPI and Histology

The GI tracts were excised from each mouse after the dynamic projection MPI study. The tracts were subsequently imaged with MPI to verify presence and location of accumulated tracer. Representative *ex vivo* MPI image and corresponding photograph are shown in

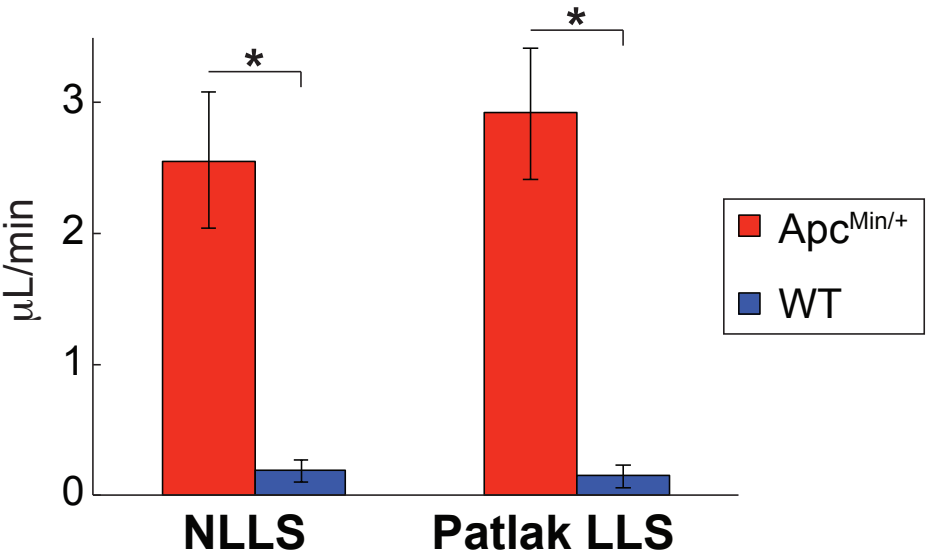

Figure 4.11: **Gut Bleed Flow Quantitation Comparison.** Bar graph of flow rate from both groups. The flow rates were significantly different between the $Apc^{Min/+}$ and wild-type groups for both fitting methods: NLLS method (p = 0.014) and Patlak LLS method (p = 0.007).

ID	Species	Hct (%)	NLLS Flow Rate (μL/min)	LLS Flow Rate (μL/min)
1	$Apc^{Min/+}$	30.18	2.01	2.39
2	$Apc^{Min/+}$	34.69	4.01	4.25
3	$Apc^{Min/+}$	34.57	1.55	1.97
4	$Apc^{Min/+}$	34.10	1.64	1.94
5	$Apc^{Min/+}$	N.A.	3.60	4.05
6	WT	42	0.34	0.32
7	WT	46	0.13	0.09
8	WT	44	0.07	0.03

Table 4.1: Gut bleed flow rate comparison.

Figure 4.12(a). Tracer accumulation was found to be intraluminal at parts of small intestine and large intestine. Quantitative comparisons were made between the *in vivo* and *ex vivo* MPI signal for all animals. Near unity slope of 0.98 was obtained for the linear fit (r^2 = 0.98). This demonstrates that MPI is reliable and gives consistent results *in vivo* and *ex vivo*.

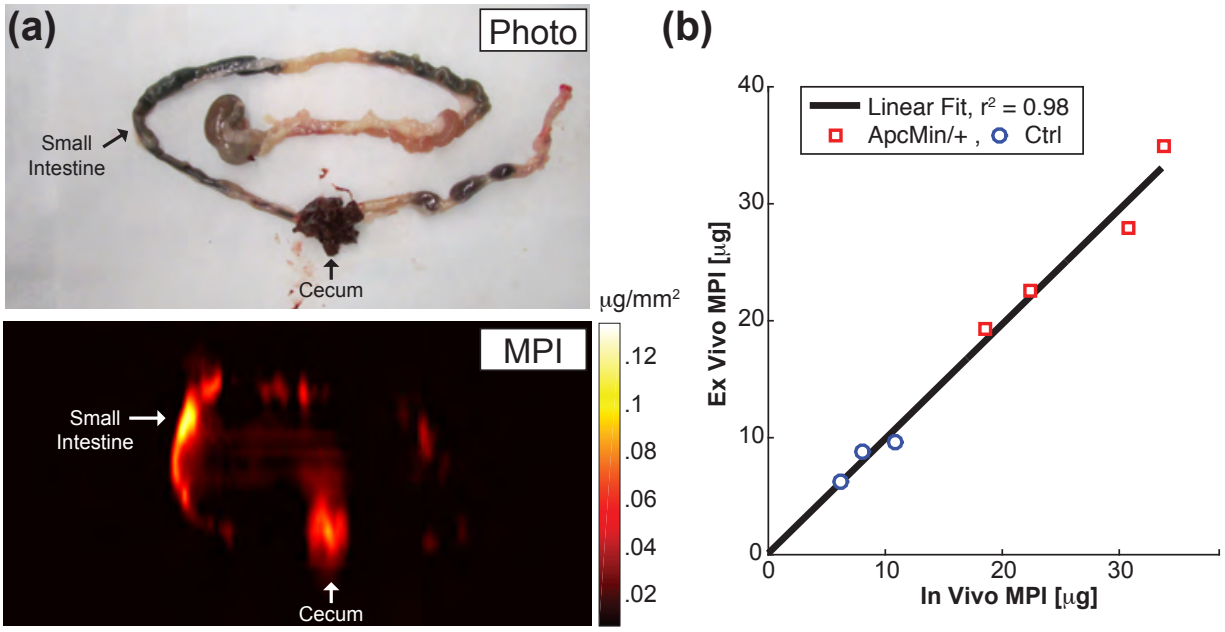

Figure 4.12: ***In vivo* and *ex vivo* MPI of GI Tract.** (a) Representative photo and corresponding MPI image of Apc$^{Min/+}$*mouse*GI tract after dynamic MPI study. Tracer accumulation is seen in the cecum and small intestine. (b) Ex vivo and in vivo MPI signal in the gut were compared for all mice. Near unity slope of 0.98 was obtained for the linearity fit ($r^2 = 0.98$).

Representative histological images of Apc$^{Min/+}$ and control mice are shown in Figure 4.12(c) and (d). The healthy control mice had well-ordered mucosal and serosal layers in their GI tracts, while the Apc$^{Min/+}$ mice had polyps along their intestinal lining. RBCs were observed within the gut lumen adjacent to a polyp, as seen in Figure 4.12(d). This confirms the GI bleeding that was observed in both *in vivo* and *ex vivo* MPI of Apc$^{Min/+}$ mice.

4.4 Discussion & Conclusion

We present the first *in vivo* report of dynamic 2D projection MPI for detection and quantitation of lower gastrointestinal gut bleed using a non-radioactive and long circulating PEGylated SPIO tracers. Unlike nuclear medicine techniques where tracer quantitation requires correction for tissue attenuation, tracer decay, and detector dead-time, MPI signal is linearly quantitative with SPIO concentration and is not affected by the tracer decay or tissue attenuation.

The quantitative nature of MPI enabled us to implement compartmental modeling to determine the bleed rate, assuming irreversible tracer extravasation into the gut lumen.

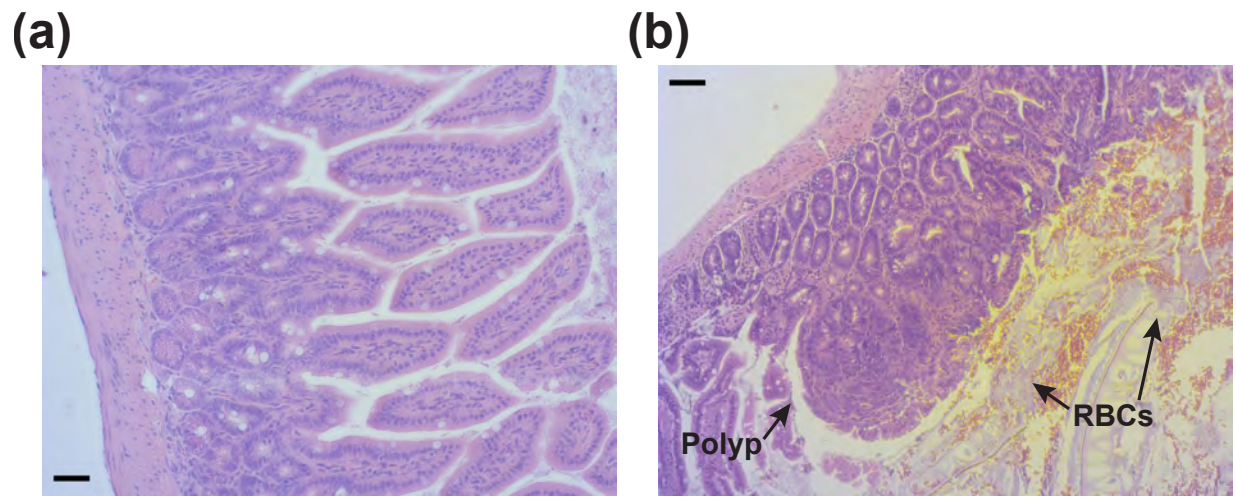

Figure 4.13: **Histology of GI Tract.** H&E stained histological section of the intestinal lumen: (c) Control mouse with well-ordered mucosal and serosal layers (20× magnification, scale bar 50 μm) and (d) Apc$^{Min/+}$ mouse with a polyp along the intestinal lining and RBCs in the lumen (10× magnification, scale bar 100 μm).

The non-linear compartment model fitting correlated well with the graphical linear least squares Patlak plot fitting result [114]. One can realize the immediate power of MPI for quantitative parametric tracer analysis. The bleed rate is of diagnostic value because it informs therapeutic intervention. We were able to detect bleed rate as slow as 1–5 μL/min. The iron content in the GI lumen measured by MPI was also consistent between *in vivo* and *ex vivo* images, demonstrating that MPI is a reliable quantitative imaging technique. MPI has a fundamental detection sensitivity in the μM range, which is less sensitive than nuclear medicine (nM–pM range) [1]. However, since SPIO tracer is safe, it has a much less stringent dose limitation compared to nuclear medicine. This is why MPI allows detection of 0.002 mL of blood, which is 10 times more sensitive than the 0.02 mL detection limit shown in a rat with planar scintigraphy using MPEG-PL-Tc-99m DTPA [115], both at clinically relevant doses. Moreover, these experiments were obtained on a custom-built, prototype MPI scanner, with engineered sensitivity far from the true physics limits. With optimized hardware and SPIOs, it is certain that MPI sensitivity could be dramatically improved.

Several SPIO tracers are FDA and EU approved for clinical use: for instance, ferumoxytol (Ferraheme) is commercially available for treating anemia and for use as an angiographic agent for MRI [116]. In addition, SPIO tracer is safe for use with patients diagnosed with chronic kidney disease (CKD), unlike iodine and gadolinium-based contrast agents used for CT and MRI [117]. By tailoring the core size and size distribution of the SPIOs, we can optimize their MPI performance [13]. Further, by modifying the surface chemistry of SPIOs, we can fine tune their pharmacokinetics and biodistribution properties *in vivo* [12, 14, 31]. In this study, we were able to achieve a prolonged circulation time (half-life of 140 minutes)

by polyethylene glycol (PEG) surface functionalization. This long-circulating nature of the tracer enabled dynamic imaging of the GI bleed over the course of 130 minutes. Unlike ^{99m}Tc-labeled RBC studies which require cumbersome *in vitro* labeling and hot chemistry[118], we were able to introduce our radiation-free SPIOs directly into the mice and image immediately. Since MPI uses zero ionizing radiation, and the SPIO tracer is safe even for use in CKD patients, one could also envision a tracer moiety that has an even more prolonged clearance half-life to enable continued patient monitoring. SPIOs can be encapsulated in PEGylated PRINT nanoparticles with circulation half-life of 19.5 hours [68] or in red blood cells with tracer life span in the mouse bloodstream prolonged to 12 days [69]. SPIO-labeled RBC MPI for detection of GI bleeding should allow imaging for as long as 12 days, instead of 24 hours as reported in $99mTc$-labeled RBC studies due to radioactive decay. With GI bleeding being intermittent by nature, repeated MPI scans could be performed to monitor the patient over longer periods of time with no tracer re-injection. This may significantly improve the accuracy of diagnosis, especially for cases of the occult and obscure GI bleeding which are currently highly challenging to diagnose and treat [109]. As we have demonstrated in this study, digital subtraction of baseline images from the rest of the images in the time course can dramatically improve image contrast. This improved image contrast will enable higher accuracy active bleed site localization, which may ultimately reduce cost and improve outcome.

The Apc$^{Min/+}$ mouse model was ideal for this study due to its clinically relevant genetic defect that causes spontaneous development of intestinal polyps. Our study warranted the need for heparin administration to induce the bleed in the mouse model, though such agents are typically contraindicated clinically for lower GI bleed diagnosis. However, we do note that clinical agents to reduce the gut peristalsis in ^{99m}Tc scans, like glucagon, can also increase cardiac contraction and vasodilation and encourage bleeding [119]. The 6.3 T/m gradient yielding 1 mm resolution projection images with our murine MPI imager are realizable at the human scale: for example, a commercially available clinical 3 T MRI scanner has a 7.2 T/m maximum spatial gradient just outside its bore [60, 120]. Further improvements to resolution below 300 μm are feasible through optimized nanoparticles and pulse sequences [10]. Higher sensitivity is also possible through tracer and hardware optimization. All these improvements should enable superior bleed site localization and improve clinical outcome. Overall, MPI is a clinically translatable imaging modality with superb contrast, sensitivity, linear quantitation and safety, lending it great promise as a diagnostic tool for GI bleed.

4.5 Acknowledgement

This work was done in collaboration with lab members Dr. Prashant Chandrasekharan, Ran Berzon, Zhi Wei Tay, Xinyi Y. Zhou, and Dr. Bo Zheng. Magnet design work was done in collaboration with Dr. Patrick W. Goodwill. Animal monitoring with MRI and compartment model fitting was done with the help and advice of Dr. Michael F. Wendland at the Berkeley Preclinical Imaging Center (BPIC). Histological sectioning and staining was

done by the UCSF Gladstone Institute Histology and Light Microscopy Core. MPI-tailored long circulating SPIOs work was done in collaboration with University of Washington and Lodespin Labs, LLC: Dr. Amit P. Khandhar, Dr. R. Matthew Ferguson, Dr. Scott J. Kemp, and Prof. Kannan M. Krishnan. This work also would not have been possible without the technical guidance from Dr. Spencer Behr and Dr. Jonathan Carter, Radiology and Gastrointestinal Surgery specialists from UCSF.

Chapter 5

Conclusion and Future Directions

Magnetic Particle Imaging is an emerging tracer imaging modality that quantitatively detects superparamagnetic iron oxide nanoparticles anywhere in the body. MPI has high image contrast, as it detects no signal from tissue, and the particle signal does not suffer from depth attenuation. MPI is highly sensitive, capable of detecting 5 nanograms of iron per voxel. MPI is also safe: the technique requires zero ionizing radiation and has clinically approved tracers available. With all these unique properties, MPI is poised to accelerate preclinical research in various areas, and can be readily translated into the clinic. These areas include cancer imaging, cell tracking, angiography, perfusion and blood pool imaging, and inflammation imaging.

One of the major challenges in MPI is spatial resolution, which is fundamentally governed by selection field gradient strength and nanoparticle properties. In this dissertation, I have designed and constructed a high gradient FFL scanner for improved spatial resolution. This is the first iron return MPI scanner, and the highest resolution FFL imager in the world. After numerous iterations in the design, we first built a $1/8^{th}$ size prototype to validate our simulations of the selection field. We experimentally validated our design, and proceeded to designed and construct the full scale FFL MPI scanner. Software and hardware modifications were made to the existing system to enable high resolution imaging. We successfully conducted 2D projection and 3D projection reconstruction imaging *in vivo* with this scanner. The improved gradient over our previous FFL system (2.35 T/m) enabled a significant boost in imaging resolution. Armed with MPI-tailored nanoparticles created by our collaborators at the University of Washington and Lodespin Labs, we were able to achieve 700 μm resolution *in vivo*. For this work, we plan to further improve the resolution by pulse sequence design and nanoparticle development, as well as additional power and coil cooling. Since the system has a selection field created by an electromagnet, it is now also possible to explore variable gradient imaging. We have planned for a pair of shim coils in our design to ensure that the FFL is homogeneous at different gradient strengths. There is also an ongoing effort in the lab to design a multi-channel transmit and receive system to achieve isotropic resolution and enable equalization to dehaze images with zero noise penalty. In addition, we have accounted for an extra pair of coils in the z-direction. These will further boost the gradient

and improve imaging speed by electronically shifting the FFL in the z-direction as opposed to mechanical translation of the sample in the current system. Compressed sensing can be used to reduce the number of angular projections required for projection reconstruction. In addition, a helical scanning trajectory similar to that used in CT can be implemented as well. In addition to hardware innovations, I have also demonstrated the use of MPI in two very important applications, namely cancer imaging and gastrointestinal (GI) bleed detection. All these efforts will enable improved resolution, image quality, and speed in the future.

In Chapter 2, I showed for the first time the use of MPI for *in vivo* cancer imaging with systemic tracer administration. Cancer remains one of the leading causes of death worldwide. Biomedical imaging plays a crucial role in all phases of cancer management. Physicians often need to choose the ideal diagnostic imaging modality for each clinical presentation based on complex trade-offs between spatial resolution, sensitivity, contrast, access, cost, and safety. The superb contrast, sensitivity, safety, and ability to image anywhere in the body lends MPI great promise for cancer imaging. In this study, long circulating MPI-tailored SPIOs were created and administered intravenously in tumor bearing rats. The tumor was highlighted with tumor-to-background ratio of up to 50. The nanoparticle dynamics in the tumor was also well appreciated, with initial wash-in on the tumor rim, peak uptake at 6 hours, and eventual clearance beyond 48 hours. Lastly, we demonstrated the quantitative nature of MPI through compartmental fitting *in vivo*. This study demonstrates passive targeting of nanopartilces to the tumor through long circulation and EPR effect. To supplement the work described in this thesis, there is an ongoing effort with our collaborators to bind MPI-tailored nanoparticles to various moieties that are thought to home to tumor biomarkers, including peptides, antibodies, and cells to achieve active targeting. In particular, we have looked at particles functionalized with RGD and Avastin, and studied the cellular uptake of particles as a function of surface charge of the particles. We plan to conduct the new active targeting studies in mice instead of rats, and use the new high resolution FFL for improved sensitivity instead of the FFP scanner. In this work, we used a xenograft tumor model in which the animal is immunocompromised. We are interested in using syngenic tumor models instead to study cancer MPI in the presence of a fully functioning immune system. Our lab is also in the early stages of demonstrating the potential for localized magnetic hyperthermia with simultaneous imaging using the existing selection field in MPI. MPI could be a powerful theranostic platform, where low frequency excitation is first used for image guidance, and high frequency excitation coupled with the FFR shifted to the tumor cite is subsequently used for magnetic hyperthermia.

In Chapter 4, I showed for the first time the use of MPI along with long-circulating, PEG-stabilized SPIOs for rapid *in vivo* detection and quantification of GI bleed. GI bleeding causes more than 300,000 hospitalizations per year in the United States. Imaging plays a crucial role in accurately locating the source of the bleed for timely intervention. In this study, a mouse model genetically predisposed to GI polyp development ($\text{Apc}^{Min/+}$) was used, and heparin was used as an anticoagulant to induce acute GI bleeding. We then injected MPI-tailored, long-circulating SPIOs through the tail vein, and tracked the tracer biodistribution over time using our custom-built high resolution FFL MPI scanner which was described

in Chapter 3. Dynamic MPI projection images captured tracer accumulation in the lower GI tract with excellent contrast. Quantitative analysis of the MPI images show that the mice experienced GI bleed rates between 1 and 5 μL/min. The robust contrast, sensitivity, safety, ability to image anywhere in the body, along with our MPI-tailored long-circulating SPIOs, demonstrate the outstanding promise of MPI as a clinical diagnostic tool for GI bleeding. To further supplement the work described in this thesis, we plan to label red blood cells (RBC) with SPIOs to increase circulation time. We are also interested in making a preclinical comparison of our technique with ^{99m}Tc labeled RBCs scintigraphy, which is the most sensitive technique currently used in the clinic to detect gastrointestinal bleeding. In addition, we are exploring methods to reliably detect slow and intermittent bleeding over long periods of time.

In conclusion, I have described in this dissertation both technical advances in MPI that enable high resolution projection and projection reconstruction imaging, as well as the first preclinical demonstrations of MPI for cancer imaging and GI bleed detection. The high resolution projection imaging capability of the new FFL imager is highly enabling for high speed dynamic projection imaging and more sensitive 3D imaging. MPI is an emerging technology in which many parameters remain to be optimized. These include slow shift and excitation pulse sequences, magnet architecture, nanoparticle size, geometry, and composition, as well as detector circuit topology, just to name a few. MPI is rapidly developing, and with its great patient safety and potentially high diagnostic quality due to high imaging contrast, it holds extraordinary promise for enabling more sensitive and earlier detection of diseases in the clinic.

Bibliography

[1] Michelle L James and Sanjiv S Gambhir. "A Molecular Imaging Primer: Modalities, Imaging Agents, and Applications". In: *Physiol. Rev.* 92.2 (Jan. 2012), pp. 897–965.

[2] Bo Zheng et al. "Quantitative Magnetic Particle Imaging Monitors the Transplantation, Biodistribution, and Clearance of Stem Cells In Vivo". In: *Theranostics* 6.3 (Jan. 2016), pp. 291–301.

[3] Bernhard Gleich and Jürgen Weizenecker. "Tomographic imaging using the nonlinear response of magnetic particles". In: *Nature* 435.7046 (30 06 2005), pp. 1214–1217.

[4] Patrick W Goodwill and Steven M Conolly. "The X-space formulation of the magnetic particle imaging process: 1-D signal, resolution, bandwidth, SNR, SAR, and magnetostimulation". In: *IEEE Trans. Med. Imag.* 29.11 (Nov. 2010), pp. 1851–1859.

[5] Kuan Lu et al. "Linearity and Shift-Invariance For Quantitative Magnetic Particle Imaging". In: *IEEE Trans. Med. Imag.* c (May 2013), pp. 1–11.

[6] Justin J Konkle et al. "Twenty-fold acceleration of 3D projection reconstruction MPI". In: *Biomed. Tech.* 58.6 (Dec. 2013), pp. 565–576.

[7] Justin J Konkle et al. "A Convex Formulation for Magnetic Particle Imaging X-Space Reconstruction". In: *PLoS One* 10.10 (23 10 2015), e0140137.

[8] J Rahmer et al. "First experimental evidence of the feasibility of multi-color magnetic particle imaging". In: *Phys. Med. Biol.* 60.5 (July 2015), pp. 1775–1791.

[9] Jürgen Rahmer et al. "Signal encoding in magnetic particle imaging: properties of the system function". In: *BMC Med. Imaging* 9 (Jan. 2009), p. 4.

[10] Zhi Wei Tay et al. "The relaxation wall: experimental limits to improving MPI spatial resolution by increasing nanoparticle core size". In: *Biomed. Phys. Eng. Express* 3.3 (27 04 2017), p. 035003.

[11] Rohan Dhavalikar et al. "Ferrohydrodynamic modeling of magnetic nanoparticle harmonic spectra for magnetic particle imaging". In: *J. Appl. Phys.* 118.17 (July 2015), p. 173906.

[12] Hamed Arami et al. "In vivo delivery, pharmacokinetics, biodistribution and toxicity of iron oxide nanoparticles". In: *Chem. Soc. Rev.* 44.23 (16 11 2015), pp. 8576–8607.

[13] R Matthew Ferguson et al. “Magnetic particle imaging with tailored iron oxide nanoparticle tracers”. In: *IEEE Trans. Med. Imag.* 34.5 (May 2015), pp. 1077–1084.

[14] A P Khandhar et al. “Evaluation of PEG-coated iron oxide nanoparticles as blood pool tracers for preclinical magnetic particle imaging”. In: *Nanoscale* 9 (3 2017), pp. 1299–1306.

[15] Lisa M Bauer et al. “Magnetic Particle Imaging Tracers: State-of-the-Art and Future Directions”. In: *J. Phys. Chem. Lett.* 6.13 (Feb. 2015), pp. 2509–2517.

[16] Patrick W Goodwill et al. “An x-space magnetic particle imaging scanner”. In: *Rev. Sci. Instrum.* 83.3 (Mar. 2012), p. 033708.

[17] Patrick W Goodwill et al. “Projection x-space magnetic particle imaging”. In: *IEEE Trans. Med. Imaging* 31.5 (May 2012), pp. 1076–1085.

[18] Kenya Murase et al. “Development of a system for magnetic particle imaging using neodymium magnets and gradiometer”. In: *Jpn. J. Appl. Phys.* 53.6 (19 05 2014), p. 067001.

[19] Klaas Bente et al. “Electronic field free line rotation and relaxation deconvolution in magnetic particle imaging”. In: *IEEE Trans. Med. Imaging* 34.2 (Feb. 2015), pp. 644–651.

[20] M Weber et al. “Scanner Construction for a Dynamic Field Free Line in Magnetic Particle Imaging”. In: *Biomed. Tech.* (July 2013).

[21] P Vogel1 et al. “First in vivo traveling wave magnetic particle imaging of a beating mouse heart”. In: *Phys. Med. Biol.* 61.18 (19 08 2016), p. 6620.

[22] X Lyu et al. “Design and Optimization for a Novel Field Free Line Generation Magnet for Human Target Clinical MPI #x2014;A Preliminary Study”. In: *IEEE Trans. Magn.* 50.11 (Nov. 2014), pp. 1–4.

[23] Emine Saritas et al. “Magnetostimulation Limits in Magnetic Particle Imaging”. In: *IEEE Trans. Med. Imaging* c (30 04 2013), pp. 1–11.

[24] Bo Zheng et al. “Magnetic Particle Imaging tracks the long-term fate of in vivo neural cell implants with high image contrast”. In: *Sci. Rep.* 5 (2015), p. 14055.

[25] J W M Bulte et al. “Quantitative “Hot Spot” Imaging of Transplanted Stem Cells using Superparamagnetic Tracers and Magnetic Particle Imaging (MPI)”. In: *Tomography* 1.2 (Dec. 2015), pp. 91–97.

[26] Elaine Y Yu et al. “Magnetic Particle Imaging: A Novel in vivo Imaging Platform for Cancer Detection”. In: *Nano Lett.* (16 02 2017).

[27] T Kuboyabu et al. “Quantitative Evaluation of Tumor Early Response to Magnetic Hyperthermia combined with Vascular Disrupting Therapy using Magnetic Particle Imaging”. In: *Int. J. Nanomed. Nanosurg.* 2.3 (2016).

[28] Xinyi Y Zhou et al. “First *in vivo* magnetic particle imaging of lung perfusion in rats”. In: *Phys. Med. Biol.* (20 02 2017).

[29] Kohei Nishimoto et al. “Application of Magnetic Particle Imaging to Pulmonary Imaging Using Nebulized Magnetic Nanoparticles”. In: *OJMI* 05.02 (2015), pp. 49–55.

[30] Sarah Vaalma et al. “Magnetic Particle Imaging (MPI): Experimental Quantification of Vascular Stenosis Using Stationary Stenosis Phantoms”. In: *PLoS One* 12.1 (May 2017), e0168902.

[31] Paul Keselman et al. “Tracking short-term biodistribution and long-term clearance of SPIO tracers in magnetic particle imaging”. In: *Phys. Med. Biol.* (Aug. 2017).

[32] Jan Sedlacik et al. “Magnetic Particle Imaging for High Temporal Resolution Assessment of Aneurysm Hemodynamics”. In: *PLoS One* 11.8 (May 2016), e0160097.

[33] Ryan Orendorff et al. “First in vivo traumatic brain injury imaging via magnetic particle imaging”. In: *Phys. Med. Biol.* 62.9 (May 2017), p. 3501.

[34] Lisa M Bauer et al. “High-performance iron oxide nanoparticles for magnetic particle imaging – guided hyperthermia (hMPI)”. In: *Nanoscale* 8.24 (16 06 2016), pp. 12162–12169.

[35] Daniel W Hensley et al. “Combining magnetic particle imaging and magnetic fluid hyperthermia in a theranostic platform”. In: *Phys. Med. Biol.* (29 12 2016).

[36] Patrick W Goodwill and Steven M Conolly. “Multidimensional x-space magnetic particle imaging”. In: *IEEE Trans. Med. Imag.* 30.9 (Sept. 2011), pp. 1581–1590.

[37] Justin J Konkle et al. “Projection reconstruction magnetic particle imaging”. In: *IEEE Trans. Med. Imaging* 32.2 (Feb. 2013), pp. 338–347.

[38] Mariusz Kowalczyk, Maciej Banach, and Jacek Rysz. “Ferumoxytol: a new era of iron deficiency anemia treatment for patients with chronic kidney disease”. In: *J. Nephrol.* 24.6 (Nov. 2011), pp. 717–722.

[39] Yi-Xiang J Wang. “Superparamagnetic iron oxide based MRI contrast agents: Current status of clinical application”. In: *Quant. Imaging Med. Surg.* 1.1 (Dec. 2011), pp. 35–40.

[40] Eric T Ahrens and Jeff W M Bulte. “Tracking immune cells in vivo using magnetic resonance imaging”. In: *Nat. Rev. Immunol.* 13.10 (Oct. 2013), pp. 755–763.

[41] Hisataka Kobayashi, Rira Watanabe, and Peter L Choyke. “Improving conventional enhanced permeability and retention (EPR) effects; what is the appropriate target?” In: *Theranostics* 4.1 (Jan. 2013), pp. 81–89.

[42] H Maeda. “The enhanced permeability and retention (EPR) effect in tumor vasculature: the key role of tumor-selective macromolecular drug targeting.” In: *Adv. Enzyme Regul.* 41 (2000), pp. 189–207.

[43] Hiroshi Maeda, Hideaki Nakamura, and Jun Fang. "The EPR effect for macromolecular drug delivery to solid tumors: Improvement of tumor uptake, lowering of systemic toxicity, and distinct tumor imaging in vivo". In: *Adv. Drug Delivery Rev.* 65.1 (Jan. 2013), pp. 71–79.

[44] K Lüdtke-Buzug et al. "Particle-Size Distribution of Dextran- and Carboxydextran-Coated Superparamagnetic Nanoparticles for Magnetic Particle Imaging". In: *World Congress on Medical Physics and Biomedical Engineering, September 7 - 12, 2009, Munich, Germany*. IFMBE Proceedings. Springer, Berlin, Heidelberg, 2009, pp. 226–229.

[45] Amit P Khandhar et al. "Tuning surface coatings of optimized magnetite nanoparticle tracers for in vivo Magnetic Particle Imaging". In: *IEEE Trans. Magn.* 51.2 (Feb. 2015).

[46] Richard Mathew Ferguson et al. "Tailoring the magnetic and pharmacokinetic properties of iron oxide magnetic particle imaging tracers". In: *Biomed. Tech.* 58.6 (Dec. 2013), pp. 493–507.

[47] Julian Haegele et al. "Magnetic particle imaging: kinetics of the intravascular signal in vivo". In: *Int. J. Nanomedicine* 9 (Mar. 2014), pp. 4203–4209.

[48] Tobias Knopp et al. "Prediction of the spatial resolution of magnetic particle imaging using the modulation transfer function of the imaging process". In: *IEEE Trans. Med. Imaging* 30.6 (June 2011), pp. 1284–1292.

[49] John Clarke and Alex I Braginski. *The SQUID Handbook: Fundamentals and Technology of SQUIDs and SQUID Systems*. 2004.

[50] Bruce J Hillman. "Introduction to the special issue on medical imaging in oncology". In: *J. Clin. Oncol.* 24.20 (Oct. 2006), pp. 3223–3224.

[51] John V Frangioni. "New technologies for human cancer imaging". In: *J. Clin. Oncol.* 26.24 (20 08 2008), pp. 4012–4021.

[52] Leonard Fass. "Imaging and cancer: a review". In: *Mol. Oncol.* 2.2 (Aug. 2008), pp. 115–152.

[53] P Caravan et al. "Gadolinium(III) Chelates as MRI Contrast Agents: Structure, Dynamics, and Applications". In: *Chem. Rev.* 99.9 (Aug. 1999), pp. 2293–2352.

[54] J Weizenecker et al. "Three-dimensional real-time in vivo magnetic particle imaging". In: *Phys. Med. Biol.* 54.5 (July 2009), pp. L1–L10.

[55] John F Schenck. "The role of magnetic susceptibility in magnetic resonance imaging: MRI magnetic compatibility of the first and second kinds". In: *Med. Phys.* 23.6 (June 1996), pp. 815–850.

[56] T Knopp et al. "Trajectory analysis for magnetic particle imaging". In: *Phys. Med. Biol.* 54.2 (19 12 2008), p. 385.

[57] Amit P Khandhar et al. “Monodisperse magnetite nanoparticle tracers for in vivo magnetic particle imaging”. In: *Biomaterials* 34.15 (May 2013), pp. 3837–3845.

[58] Elaine Yu et al. “In vivo Projection Imaging and 3D Computed Tomography Magnetic Particle Imaging with a High Resolution 6 T/m Field Free Line Electromagnet”. In: *World Molecular Imaging Congress*. World Molecular Imaging Society (WMIS). 2016.

[59] M Lu et al. “FDA report: Ferumoxytol for intravenous iron therapy in adult patients with CKD”. In: *Am. J. Hematol.* 85(5) (2010), pp. 315–319.

[60] Emine U Saritas et al. “Magnetic particle imaging (MPI) for NMR and MRI researchers”. In: *J. Magn. Reson.* 229 (Apr. 2013), pp. 116–126.

[61] P W Goodwill et al. “A 7 T/M 3D X-space MPI mouse and rat scanner”. In: *2013 International Workshop on Magnetic Particle Imaging (IWMPI)*. Mar. 2013, pp. 1–1.

[62] Scott J Kemp et al. “Monodisperse magnetite nanoparticles with nearly ideal saturation magnetization”. In: *RSC Adv.* 6.81 (2016), pp. 77452–77464.

[63] R Chantrell, J Popplewell, and S Charles. “Measurements of particle size distribution parameters in ferrofluids”. In: *IEEE Trans. Magn.* 14.5 (Sept. 1978), pp. 975–977.

[64] Shreyas S Vasanawala et al. “Safety and technique of ferumoxytol administration for MRI”. In: *Magn. Reson. Med.* 75.5 (May 2016), pp. 2107–2111.

[65] Michelle Longmire, Peter L Choyke, and Hisataka Kobayashi. “Clearance properties of nano-sized particles and molecules as imaging agents: considerations and caveats”. In: *Nanomedicine* 3.5 (Oct. 2008), pp. 703–717.

[66] M.M.J. Modo and J.W.M. Bulte. *Molecular and Cellular MR Imaging*. CRC Press, 2007. ISBN: 9781420004090. URL: https://books.google.com/books?id=0itc7OEoKBcC.

[67] Uma Prabhakar et al. “Challenges and key considerations of the enhanced permeability and retention effect for nanomedicine drug delivery in oncology”. In: *Cancer Res.* 73.8 (15 04 2013), pp. 2412–2417.

[68] Jillian L Perry et al. “PEGylated PRINT nanoparticles: the impact of PEG density on protein binding, macrophage association, biodistribution, and pharmacokinetics”. In: *Nano Lett.* 12.10 (Oct. 2012), pp. 5304–5310.

[69] Antonella Antonelli et al. “New Strategies to Prolong the In Vivo Life Span of Iron-Based Contrast Agents for MRI”. In: *PLoS One* 8.10 (25 10 2013), e78542.

[70] Stephanie D Steichen, Mary Caldorera-Moore, and Nicholas A Peppas. “A review of current nanoparticle and targeting moieties for the delivery of cancer therapeutics”. In: *Eur. J. Pharm. Sci.* 48.3 (14 02 2013), pp. 416–427.

[71] Rafal Swiercz et al. “Use of Fc-Engineered Antibodies as Clearing Agents to Increase Contrast During PET”. In: *J. Nucl. Med.* 55.7 (July 2014), pp. 1204–1207.

[72] Hao Hong et al. “Non-invasive cell tracking in cancer and cancer therapy”. In: *Curr. Top. Med. Chem.* 10.12 (2010), pp. 1237–1248.

[73] Jeff W M Bulte et al. “MPI Cell Tracking: What Can We Learn from MRI?” In: *Proc. SPIE Int. Soc. Opt. Eng.* 7965 (2011), 79650z.

[74] D Hensley et al. “Preliminary experimental X-space color MPI”. In: *2015 5th International Workshop on Magnetic Particle Imaging (IWMPI),* Mar. 2015, pp. 1–1.

[75] Vicky V Mody et al. “Magnetic nanoparticle drug delivery systems for targeting tumor”. In: *Appl. Nanosci.* 4.4 (Apr. 2013), pp. 385–392.

[76] Manuel Bañobre-López, Antonio Teijeiro, and Jose Rivas. “Magnetic nanoparticle-based hyperthermia for cancer treatment”. In: *Rep. Prac. Oncol. Radiother.* 18.6 (Jan. 2013), pp. 397–400.

[77] Adam J Cole, Victor C Yang, and Allan E David. “Cancer theranostics: The rise of targeted magnetic nanoparticles”. In: *Trends Biotechnol.* 29.7 (2011), pp. 323–332.

[78] Qiaoyun Shi et al. “Evaluation of the novel USPIO GEH121333 for MR imaging of cancer immune responses”. In: *Contrast Media Mol. Imaging* 8.3 (May 2013), pp. 281–288.

[79] Daniel Hensley et al. “A New Theranostics Platform: Magnetic Fluid Hyperthermia Localized with a Strong Gradient and Simultaneously Imaged with Magnetic Particle Imaging”. In: *World Molecular Imaging Congress*. World Molecular Imaging Society (WMIS). 2016.

[80] Jerry L Prince and Jonathan M Links. *Medical imaging signals and systems*. Pearson Prentice Hall Upper Saddle River, New Jersey, 2006.

[81] Juergen Weizenecker, Bernhard Gleich, and Joern Borgert. “Magnetic particle imaging using a field free line”. In: *J. Phys. D Appl. Phys.* 41.10 (Jan. 2008), p. 105009.

[82] Tobias Knopp et al. “Efficient generation of a magnetic field-free line”. In: *Med. Phys.* 37.7 (July 2010), pp. 3538–3540.

[83] Tobias Knopp et al. “Generation of a static magnetic field-free line using two Maxwell coil pairs”. In: *Appl. Phys. Lett.* 97.9 (30 08 2010), p. 092505.

[84] Marlitt Erbe et al. “Experimental generation of an arbitrarily rotated field-free line for the use in magnetic particle imaging”. In: *Med. Phys.* 38.9 (Sept. 2011), pp. 5200–5207.

[85] A Tonyushkin. “Single-Sided Field-Free Line Generator Magnet for Multi-Dimensional Magnetic Particle Imaging”. In: *IEEE Trans. Magn.* PP.99 (2017), pp. 1–1.

[86] Mat A Bernstein et al. “Concomitant gradient terms in phase contrast MR: Analysis and correction”. In: *Magn. Reson. Med.* 39.2 (Jan. 1998), pp. 300–308.

[87] Whittier R Myers, Michael Mössle, and John Clarke. “Correction of concomitant gradient artifacts in experimental microtesla MRI”. In: *J. Magn. Reson.* 177.2 (Dec. 2005), pp. 274–284.

[88] Edward P Furlani. *Permanent Magnet and Electromechanical Devices: Materials, Analysis, and Applications*. Academic Press, 2001.

[89] P Elleaume, O Chubar, and J Chavanne. "Computing 3D magnetic fields from insertion devices". In: *Proceedings of the 1997 Particle Accelerator Conference (Cat. No.97CH36167)*. Vol. 3. May 1997, 3509–3511 vol.3.

[90] I E Dayton, F C Shoemaker, and R F Mozley. "The Measurement of Two-Dimensional Fields. Part II: Study of a Quadrupole Magnet". In: *Rev. Sci. Instrum.* 25.5 (Jan. 1954), pp. 485–489.

[91] Jack T Tanabe. *Iron Dominated Electromagnets: Design, Fabrication, Assembly and Measurements*. World Scientific, 2005.

[92] David Weston. *Electromagnetic Compatibility: Principles and Applications, Second Edition, Revised and Expanded*. CRC Press, 30 01 2001.

[93] Y Chung and J Galayda. *Effect of eddy current in the laminations on the magnet field*. Tech. rep. Argonne National Laboratory, 1992.

[94] Laura R Croft, Patrick W Goodwill, and Steven M Conolly. "Relaxation in x-space magnetic particle imaging". In: *IEEE Trans. Med. Imaging* 31.12 (Dec. 2012), pp. 2335–2342.

[95] Zhi Wei Tay et al. "A High-Throughput, Arbitrary-Waveform, MPI Spectrometer and Relaxometer for Comprehensive Magnetic Particle Optimization and Characterization". In: *Sci. Rep.* 6 (30 09 2016), p. 34180.

[96] Kuan Lu et al. "Towards multidimensional x-space magnetic particle imaging for improved resolution". In: *2013 International Workshop on Magnetic Particle Imaging (IWMPI)*. Mar. 2013, pp. 1–1.

[97] K Lu et al. "Reshaping the 2D MPI PSF to be isotropic and sharp using vector acquisition and equalization". In: *2015 5th International Workshop on Magnetic Particle Imaging (IWMPI)*. Mar. 2015, pp. 1–1.

[98] Daniel A Price et al. "Improving conspicuity in MPI by equalization of the "broad tails" of the MPI point spread function". In: *Magnetic Particle Imaging (IWMPI), 2013 International Workshop on*. 2013, pp. 1–1.

[99] Michael Lustig, David Donoho, and John M Pauly. "Sparse MRI: The application of compressed sensing for rapid MR imaging". In: *Magn. Reson. Med.* 58.6 (Dec. 2007), pp. 1182–1195.

[100] Xueli Li and Shuqian Luo. "A compressed sensing-based iterative algorithm for CT reconstruction and its possible application to phase contrast imaging". In: *Biomed. Eng. Online* 10 (18 08 2011), p. 73.

[101] Anne Paterson, Donald P Frush, and Lane F Donnelly. "Helical CT of the Body". In: *American Journal of Roentgenology* 176.2 (Jan. 2001), pp. 297–301.

[102] Bong Sik Matthew Kim et al. "Diagnosis of gastrointestinal bleeding: A practical guide for clinicians". In: *World J. Gastrointest. Pathophysiol.* 5.4 (15 11 2014), pp. 467–478.

[103] S Quiroga Gómez et al. "Gastrointestinal bleeding: the role of radiology". In: *Radiologia* 53.5 (Sept. 2011), pp. 406–420.

[104] A. M. Vernava et al. "Lower gastrointestinal bleeding". In: *Dis. Colon Rectum* 40.7 (July 1997), pp. 846–858.

[105] R. S. Ramaswamy et al. "Role of interventional radiology in the management of acute gastrointestinal bleeding". In: *World J Radiol* 6.4 (Apr. 2014), pp. 82–92.

[106] B. C. Bounds and L. S. Friedman. "Lower gastrointestinal bleeding". In: *Gastroenterol. Clin. North Am.* 32.4 (Dec. 2003), pp. 1107–1125.

[107] William G Kuhle and Robert G Sheiman. "Detection of active colonic hemorrhage with use of helical CT: findings in a swine model". In: *Radiology* 228.3 (Sept. 2003), pp. 743–752.

[108] R Dusold et al. "The accuracy of technetium-99m-labeled red cell scintigraphy in localizing gastrointestinal bleeding". In: *Am. J. Gastroenterol.* 89.3 (Mar. 1994), pp. 345–348.

[109] K A McKusick et al. "99mTc red blood cells for detection of gastrointestinal bleeding: experience with 80 patients". In: *AJR Am. J. Roentgenol.* 137.6 (Dec. 1981), pp. 1113–1118.

[110] A H Maurer et al. "Effects of in vitro versus in vivo red cell labeling on image quality in gastrointestinal bleeding studies". In: *J. Nucl. Med. Technol.* 26.2 (June 1998), pp. 87–90.

[111] R R Kester, J P Welch, and J P Sziklas. "The 99mTc-labeled RBC scan. A diagnostic method for lower gastrointestinal bleeding". In: *Dis. Colon Rectum* 27.1 (Jan. 1984), pp. 47–52.

[112] A R Moser et al. "ApcMin, a mutation in the murine Apc gene, predisposes to mammary carcinomas and focal alveolar hyperplasias". In: *Proceedings of the National Academy of Sciences* 90.19 (Jan. 1993), pp. 8977–8981.

[113] Kannan M. Krishnan. *Fundamentals and Applications of Magnetic Materials*. 1st ed. Vol. 1. 1. 198 Madison Ave.,New York, NY 10016, USA: Oxford University Press, Oct. 2016. ISBN: 9780199570447.

[114] C S Patlak, R G Blasberg, and J D Fenstermacher. "Graphical evaluation of blood-to-brain transfer constants from multiple-time uptake data". In: *J. Cereb. Blood Flow Metab.* 3.1 (Mar. 1983), pp. 1–7.

[115] H Gupta et al. "Experimental gastrointestinal hemorrhage: detection with contrast-enhanced MR imaging and scintigraphy". In: *Radiology* 196.1 (Jan. 1995), pp. 239–244.

[116] "Molecular Imaging and Contrast Agent Database (MICAD) [Internet]". In: *National Center for Biotechnology Information (US), Bethesda (MD)* (2004-2013), Available from: https://www.ncbi.nlm.nih.gov/books/NBK5330/.

[117] S. S. Vasanawala et al. "Safety and technique of ferumoxytol administration for MRI". In: *Magn Reson Med* 75.5 (May 2016), pp. 2107–2111.

[118] S. C. Srivastava and L. R. Chervu. "Radionuclide-labeled red blood cells: current status and future prospects". In: *Semin Nucl Med* 14.2 (Apr. 1984), pp. 68–82.

[119] Farhood Saremi, Hossein Jadvar, and Michael E Siegel. "Pharmacologic Interventions in Nuclear Radiology: Indications, Imaging Protocols, and Clinical Results". In: *Radiographics* 22.3 (Jan. 2002), pp. 477–490.

[120] Frank G Shellock, Emanuel Kanal, and Tobias B Gilk. "Regarding the value reported for the term "spatial gradient magnetic field" and how this information is applied to labeling of medical implants and devices". In: *AJR Am. J. Roentgenol.* 196.1 (Jan. 2011), pp. 142–145.